UNIVERSITÀ DI PISA

Scuola di Dottorato in Ingegneria "Leonardo da Vinci"
Stefano Bennati (Direttore)

Programma di Dottorato in Automatica Robotica e Bioingegneria
Andrea Caiti (Presidente)

NOVEL BIO-AWARE TECHNOLOGIES AND ALGORITHMS FOR HANDS AND HAPTICS

Tesi di dottorato

Tutori:
Prof. Ing. Antonio BICCHI

Dott. Ing. Darwin CALDWELL

Dott. Ing. Nikos TSAGARAKIS

Dottorando:
Alessandro SERIO

Luglio 2013

Abstract

This thesis focuses on novel algorithms and interfaces, arising from inspection and comprehension of the human nature.

In the first part I deal with new mechanical designs and concepts for building and controlling robotic hands. In particular I show how the sensorimotor synergies of the human hand can be useful not only for controlling but also for building robotic hands, suggesting novel design paradigms.

Despite the synergy model is useful for designing and controlling robotic hands, it is incomplete to explain the hand behavior during grasp (both for humans and robots). To solve this problem, it is needed to consider compliant articulations introducing the "soft synergies" concept. Consequently, the compliance and the soft synergies lead to the concepts of muscle and mechanical impedance. Thus, in the second part of this thesis I present an observer for estimating the time varying mechanical impedance of a Variable Stiffness Actuator (VSA), i.e. a novel kind of actuator whose performances and capabilities are very close to the human muscles.

Another important feature, both for human and robotic hands, is the sense of touch. Indeed in the third and last part of this thesis, I deal with the haptics and haptic interfaces. I show two new haptic devices with their applications on humans. Moreover, I present a tactile sensing algorithm toolbox for computing the contact point of a robotic fingertip interacting with an object.

Acknowledgements

First and foremost I offer my sincerest gratitude to my supervisors, Antonio Bicchi, Darwin Caldwell and Nikos Tsagarakis. In particular I wish to thank professor Antonio Bicchi who has supported me throughout these last years with his patience and wide knowledge. I attribute the level of my PhD thesis to his encouragement, effort and precious suggestions.

I also would like to express my deep gratitude to my "lab friends": Matteo, Andrea, Andrea, Manuel, Giorgio, Fabio, Paolo, Manolo and all the guys of the lab.

A particular thank goes to my family, to my girlfriend and to my long time friends. I have really appreciated their support over these years.

Contents

Introduction

In this thesis I introduce novel technologies and algorithms employed in robotic hands and in haptics. All of these technologies and algorithms are derived from the study or inspection of the human behavior using biological inspiration as a starting point.

The first part of this thesis deals with hands and robotic hands: indeed, among the many aspects which characterize the human being, distinguishing it from other animated entities, the hand stands out. Its wonderful complication gives humans a wide spectrum of possibilities, which, very roughly, can be summarized in the 4 functional groups of sensation, holding, manipulation and communication. Over the centuries of human cultural and technological evolution the importance of the hand shape has played an important role, shaping the word around us in a reality made of handles, knobs, buttons and keyboards.

A hand designed with the only purpose of holding, for example, can still be fruitfully employed to perform a large number of everyday actions. In [19] two job activities are considered in detail as case-study (professional house-holding and machine operation). Highlithing that more than 50% of time the hand is used for grasping (63% for the house holder and 56% for the machinist).

Looking at how the brain copes with such complexity and redundancy, it is possible to argue on strategies that can be implemented in artificial systems, to enhance design simplicity, control and performance. This idea has been suggested by the dual concept of *hand postural synergies*; i.e. constraints due to peripheral and central contributions in the inter-digit movements and force exertion that actually reduces the dimensionality of the kinematic space of the human hand (or in other terms the number of hand Degrees of Freedom (DoFs) that can be independently controlled by the nervous system [20]).

A further enhancement of the synergies can be found in [21] where authors introduce concept of *soft synergies*. Indeed, the sole kinematic model with synergies of the hand fails to describe the actual grasp of an object. Therefore, contact forces must be brought into play if a realistic grasp analysis is in order. Taking a step further, and in view of dealing with the most general case of statically-indeterminate grasps, both contact and joint compliances have to be included in the analysis.

It is worth mentioning that this complaiant model, whereby motion is controlled by a reference position and modulation of joint stiffness, has apparent similarities with the equilibrium point hypothesis in the motor control literature [22].

The joint compliance introduces also the concept of variable impedance actuator (VIA) i.e. actuators capable of changing both shaft position and mechanical impedance. These actuators have a great importance in robotics because can be considered an approximation and an idealization of human muscles.

Thus, in the second part of this thesis I deal with the estimation of the mechanical impedance of VIA. In fact, it is well know that to fully characterize the motion of human limbs, not only knowledge of their position and velocity, but also of their physical behaviour in interaction with the environment, i.e. their mechanical impedance is needed [23–25]. Analogously, many modern robots are capable of changing their mechanical impedance to better perform a task and adapt to an environment. Variable impedance is obtained in these system by either intrinsic physical properties of the actuators (e.g. muscles in humans, or Variable Stiffness Actuators [26] in robots) or by low-level control (neural reflexes or impedance control).

Because of its ubiquitous importance, accurate measurements of the mechanical impedance of limbs are very important. Unfortunately, impedance is a rather elusive object to measure, as it is not, strictly speaking, a physical quantity per se (where by physical quantity it is meant “a property of a phenomenon, body, or substance, where the property has a magnitude that can be expressed as a number and a reference” [27]. Indeed, impedance is rather a differential operator relating the time course of physical quantities (forces and displacements). In full generality, therefore, the process of characterizing impedance of a system is more a problem of dynamical system identification than a direct measurement in a traditional sense.

Current protocols for identifying impedance in human motion typically measure the basic parameters of mass, damping, and stiffness, which concur in forming impedance, by experiments in which perturbations are purposefully injected in the system, and their effects are measured. These experiments are designed specifically so as to isolate the effects of different parameters of impedance, while at the same time minimizing perturbation of the task during which the measurement is needed [25]. In artificial robotic systems, impedance parameters are either calculated on the basis of a precise description of the model (wherever this is available), or obtained through accurate calibration procedures.

In both natural and artificial systems, it would be of great utility to have a method which could measure all impedance parameters in real time, without perturbing the normal execution of the task, and robust to inaccurate modeling and time-varying parameters which could alter calibration results.

Of particular interest in robotics would be the application of such methods to the class of Variable Impedance Actuators (VIA), which have been recently introduced to address the need for adaptability to the environment, energy conservation, and safety during physical interaction with humans. These have been implemented in a variety of ways, using different transduction technologies (electromechanical, pneumatic, hydraulic, but also piezoelectric, active polymeric, etc.) and arrangements. All designs share a fundamentally unavoidable nonlinear behavior.

Development of such novel actuators gives rise to interesting problems in term of control. A number of recent papers tackle the problem of controlling variable stiffness devices. Approaches ranging from simple PD control [28], to more sophisticate feedback linearization techniques [29] are adopted to control stiffness in VSAs. Nevertheless, most of these approaches suffer from the same flaw: the stiffness is not obtained trough direct measurements but it is inferred from the mathematical model of the device. This implies that all of the proposed control architectures are not closing the feedback loop on the value of stiffness, thus not directly controlling it.

Another important topics related to the hands and to their biological behavior are the haptic perception and the sense of touch which are tackled in the third and last part of this thesis.

Haptic perception allows to explore and recognize an object by conveying several physical information to mechano-receptors and thermo-receptors lying into our skin throughout the body. The term "haptic" is usually referred to eliciting both kinaesthetic and cutaneous channels ([30], [31]). In some cases kinaesthesia can play a more relevant role in discriminating physical or geometrical features rather than cutaneous information, while, in other cases, the role is symmetrically exchanged. For instance, while weight is dominated by kinaesthesia, thermal sensations are purely cutaneous.

However, both are necessary to have a fine and reliable perception of the reality, even if the cutaneous cues are generally predominant [32].

In addition to recent haptic displays ([33]), which focused on providing cutaneous cues, it is worthwhile mentioning other surrogating detailed contact shape information with information on the contact area on the fingertip and its changes with varying contact force (see e.g. [34], [35]). Although all these displays are capable of rendering a reliable softness sensation, there are still some technical limitations due to low resolution of stimuli.

Softness is the subjective measurement of the compliance of an object. This kind of information is very tactual–related [36] and hence its correct rendering is particularly challenging in haptics to guarantee a compelling perception. Regarding the two main modalities of haptic perception, kinaesthesia and tactile information, softness perception basically relies on both although cutaneous cues play a predominant role in most cases [37].

Different technological solutions have been adopted so far to build suitable devices [34, 35, 38] for softness rendering but the results, although reliable, are still unsatisfactory if compared to the human touch, and the low resolution of stimuli severely affects technical performance. Indeed, the mechanics of touch is very complex, consisting on a huge amount of redundant information processed via many receptors.

Considering cutaneous cues, a possible *reduction* of dynamic, force-varying tactile information operated by nervous system can be represented by the experimentally validated Contact Area Spread Rate (CASR) hypothesis [34]. It affirms that a considerable part of tactile ability in object softness discrimination is retained in the relationship between the contact area growth over the finger pad pressing the object and the indenting force itself. Inspired by this simple force-area relation, it was possible to develop simple and effective haptic interfaces such as the pneumatic CASR display [34]. However, although this device was proved to be able to convey a more compelling softness perception (if compared to a purely kinaesthetic one), its performance was limited by the lack of a real-time contact area measurement system, the edge effects due to its "discrete design" and the low resolution of the stimuli.

Thesis Structure This thesis is structured as follows (see also fig. 1 for a general overview):

1. Part I: Chapter 1 and 2 introduce two novel prototype of robotic

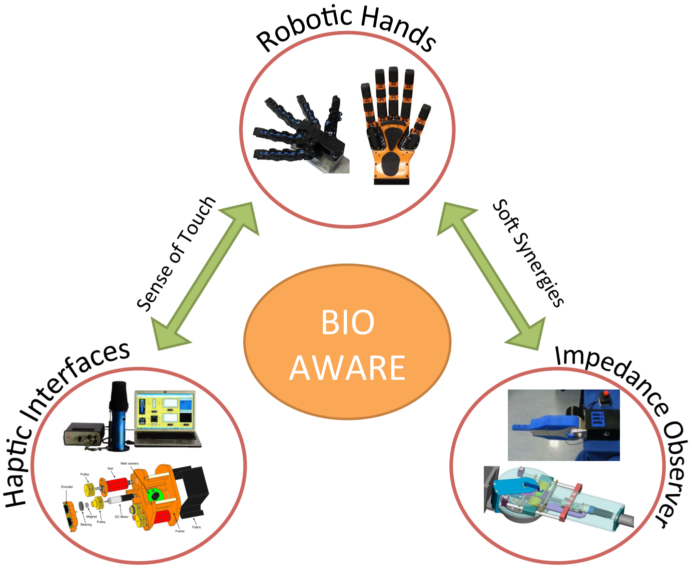

Figure 1: Thesis structure and its main part.

hand. The first presented, called *THE First Hand*, is a low cost with16 degree of freedoms (DoFs) robotic hand while the second one is an underactuated object adaptive hand, called *PISA–IIT SoftHand*, respectively.

2. Part II: Chapter 3 presents an algorithm for estimating variable mechanical impedance of variable stiffness actuators (VSAs).

3. Part III: Chapter 4 and 5 deal with novel haptic devices, the Fabric Yielding Display (FYD) and Fabric Yielding Display 2 (FYD–2) based on a bielastic fabric and capable to direct measure the contact area of a fingertip during the haptic exploration. Chapter 6 deals with the calibration an the contact point detection of 36 axis force/torque sensor (F/T) used for characterizing human grasp.

Thesis Motivation and Contributions The motivations behind the development of robotic hand is the will to comply with, and fruitfully integrate in the human environment, a world forged by humans for humans, where the importance of the hand shape dominates prominently. Nowadays robotics hand are complex mechanisms, many time fragile, expensive and not simple to use. In this thesis I introduce two novel robotic hands which can be considered a simplification, but with the same performances, of the classical robotic hands. Thus it is presented a novel, low cost, fully actuated robotic hand with 5 finger and with a kinematic very similar to an human hand, called *THE FIrst Hand*. Moreover, it is presented the first implementation of the PISA–IIT hand, a prototype which conciliates the idea of adaptive synergies for actuation with an high degree of integration, in a humanoid shape.

Then, in the second part of the thesis I tackle the problem of the variable mechanical impedance for VSA, i.e device that can be considered as robot muscles. All the VSAs suffers of the same flaw: the stiffness is not obtained trough direct measurements but it is inferred from the mathematical model of the device. In order to control the stiffness (or the in general the impedance), closing a real time loop, it is needed an algorithm to estimate the impedance. In this work I propose a technique for the combined estimation of the whole set of impedance parameters of a VSA powered system, which avoids interacting observation loops, thus preserving robustness of the estimation. The derived method can be applied to a class of variable stiffness devices.

Finally, the motivations behind the haptic devices can be found considering that in a good tactile perception, both kinaestetic and cutaneous cue are to be considered. Now, a great number of haptic interfaces rely only on the kinaesthetic rendering without consider any information on contact area and, more in general, on cutaneous cues. For the reasons above, in this work I present two novel prototype of haptic devices which are capable to directly measure the contact area of a fingertip during the haptic exploration. Moreover, with these devices it is possible to mimic different stiffness levels and force-area curves linked to the human touching.

In the last part of this thesis I deal with a sensorized object which will be employed in experiments of human grasping characterizations for measuring contact wrenches and points. This object can change its shape by applying different patches on its surface. The core of this object is 36 axis F/T sensor. Here, I present three calibration methods for the 36 axis F/T and, subsequently, I present a tactile toolbox for detecting the contact point which it is used on the sensorized object.

Part I

Robotic Hands Design and Control

This part presents two novel prototypes of robotic hands.

In chapter 1 a 5 finger robotic hand with 16 degree of freedoms (DoFs), called *THE First Hand* is introduced. To test the performances of this hand, some static and dynamic grasps with common objects are executed.

In chapter 2 I introduce an under–actuated robotic hand, called PISA–IIT hand. This hand is designed and builded exploiting the concept of synergies, both for the human and robotic point of view.

Also for this hand, some grasps of common object are performed to test its performances.

Chapter 1

THE First Hand

THIS CHAPTER introduces a novel robotic hand, called *THE First Hand*. This hand has 5 finger and, in total,16 degree of freedoms (DoFs). It can reproduce movements very similar to the human hand (see fig. 1.1 for more details). The hand is designed exploiting the paradigm "low cost but smart" and It is possible to consider *THE First Hand* as a feasibility study on cheap material and simple mechanisms for assembling robotic hands.

The performances of the hand are tested with grasp experiments on common object and then with a complex grasping task (for more details of this work see also [A1]).

1.1 An Overview on Robotic Hands

Man has always tried to replicate ability and movements of human hand in robot. But human hand can make really hard and specific movements. Furthermore the system that regulates the movement is complex, thus it is very difficult to replicate perfectly all human features in a robotic hand.

The problem is to build an artificial hand capable to make a wide range of movements easily, but with a simple design and employing

Figure 1.1: *THE first Hand* prototype: a 5 fingers, 16 DoFs robotic hand driven by tendons.

cheap materials. Studies and researches of this topic led to the construction of some robotic hands, with a wide use range for humanoid robots or prosthesis (as for example [39] or [40], but many others robotic hands can be found in literature).

Yet today it was not possible to build a perfect artificial hand, also the more complete hand shows several limits.

1.2 Mechanical Design

The robotic hand here presented, called *THE First Hand* is designed in order to reproduce the kinematic structure of a human hand with the same general dimensions. The hand has 5 fingers driven by tendons for a total of 16 DoFs.

All the proximal phalanges of *THE First Hand* have an independent DoF with an angular displacement of about 90°. For each finger, except the thumb, the upper phalanges (intermedial and distal) has one DoF with dependent movements. The thumb has only two phalanges, with independent movements. Each finger has independent abduction with an angular displacement of about 40°, except the medium which do not have abduction.

Finally, the palm has two independent DoFs with an angular displacement of about 30° and it is linked to the thumb and to the little in order to replicate the palm arch closure.

THE First Hand has been developed to study synergies from software point of view. Indeed, this robotic hand is intended as a study platform for mapping synergies and for studying robotic grasp. For these purposes, *THE First Hand* was build respecting a simple and low cost design paradigm in order to have a robust, quick and simple to use prototype.

Another design target was connected to the prototype size and movement capability. I chose to build a robotic hand very similar to a human hand as far as dimensions and movements are concerned, in a sort of bio-replication design paradigm.

1.2.1 Joint Design

Essentially, the hand is composed by two type of joint: rotational joint and the Cardan joint. Each rotational joint is composed by a shaft and a torsion spring (joint details are reported in fig. 1.2). This structure allows to use only one tendon to move the joint, indeed the tendon can move the link from its rest position to a desired one

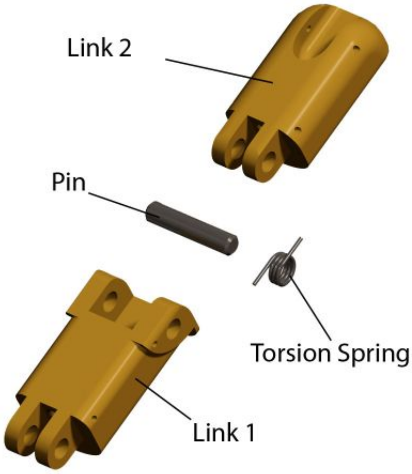

Figure 1.2: Rotational joint of the robotic hand with its main component.

compressing the spring, then, once the tendon is released, the spring is able to recoil the link in the starting position. The Cardan joints are composed by 2 rotational joints with normal axes and are employed. They are build for the abductions where 2 DoFs are needed.

1.2.2 Tendon Routing

To achieve a better tendon displacement a double layer tendon routing is implemented. The upper phalanges of the robotic hand are linked to the motor pulleys by tendons lying on a certain plane while the lower phalanges of the robotic hand are connected to the motors with tendons lying on a lower plane.

In the proximity of the motors tendons are redirected on the pulley plane (for details see fig. 1.3). In practice, this approach allows to simplify the tendon routing decoupling the movements of the upper phalanges of the robotic had from the movements of the lower phalanges.

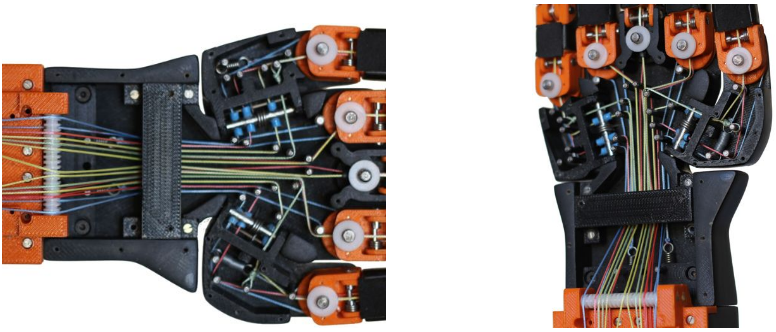

Figure 1.3: Double layer tendon routing of *THE First Hand*.

1.2.3 Zero Torque Pin

The solution of using only one tendon to actuate the DoF makes necessary the uses of zero torque joints. Zero torque pin are implemented drilling an hole perpendicular to the joint pin axis.

In this way, if a tendon must not produce a torque on a certain link, can pass through the pin hole.

In particular this pin are located in the abduction joints where the movement of the phalanges must be decoupled from the abduction movements.

1.2.4 Actuation

The actuation system is based on hobbistic servomotor servomotors (HITEC 645 Hg) which can achieve a 1 Nm of maximum torque with an angular displacement of 180°. Rotational velocity is $60°/s$.

Tendons are fixed on the pulleys blocked on the servomotor shaft thus, the only sensors of the robotic hand are the encoders in the servomotors. In this way it is possible to control *THE First Hand* with the direct and inverse kinematics (see section 1.3 and 1.4, respectively) without bearing down on the hand cost.

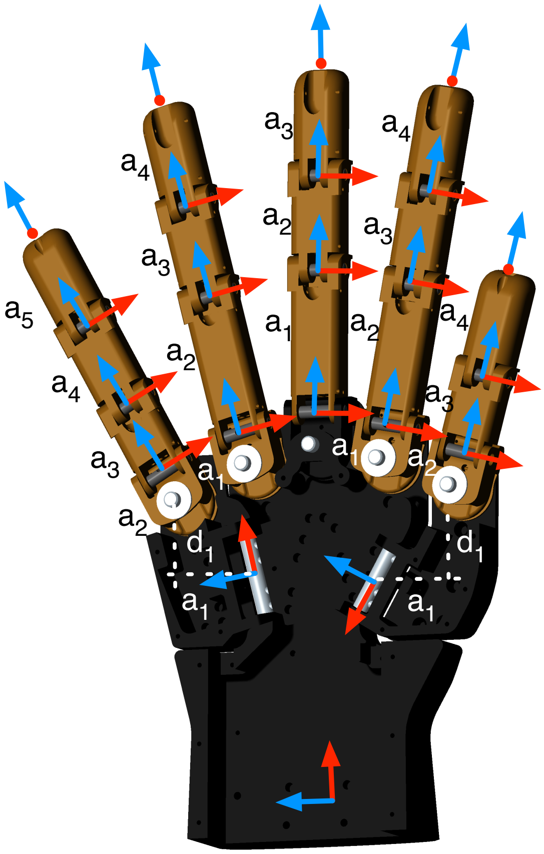

Figure 1.4: Reference system of the *THE First Hand* for the Denavit–Hartemberg tables. With red arrows I point out the z axis while with the blue arrows the x axis. Red point is the z axis out coming from the sketch plane. For sake of clarity, abduction frames are not reported but they are considered with z axis incoming in the sketch plane and x in the same verse of the phalanges frame.

1.3 Direct Kinematics

Through the direct kinematics I describe the relationship between the joint positions and the the position of fingertips.

Table 1.1: DH Table for the thumb

Link	a_i	α_i	d_i	θ_i
1	$-a_1$	$-\pi/2$	$-d_1$	θ_1
2	a_2	$-\pi/2$	0	$\pi/2 + \theta_2$
3	a_3	0	0	θ_3
4	a_4	0	0	θ_4

Table 1.2: DH table for the index

Link	a_i	α_i	d_i	θ_i
1	a_1	$-\pi/2$	0	θ_1
2	a_2	0	0	θ_2
3	a_3	0	0	θ_3
4	a_4	0	0	θ_4

Table 1.3: DH table for the medium

Link	a_i	α_i	d_i	θ_i
1	a_1	0	0	θ_1
2	a_2	0	0	θ_2
3	a_3	0	0	θ_3

Table 1.4: DH table for the ring

Link	a_i	α_i	d_i	θ_i
1	a_1	$\pi 2$	0	θ_1
2	a_2	0	0	θ_2
3	a_3	0	0	θ_3
4	a_4	0	0	θ_4

Table 1.5: DH table for the little

Link	a_i	α_i	d_i	θ_i
1	$-a_1$	$\pi/2$	d_1	$\pi + \theta_1$
2	a_2	$\pi/2$	0	$\pi/2 + \theta_2$
3	a_3	0	0	θ_3
4	a_4	0	0	θ_4
5	a_5	0	0	θ_5

In this case, each finger is considered separately as a serial kinematics chain. Then, each finger is linked to a reference frame fixed to the palm. Reference frame is the same for all the fingers.

Abduction joints are modeled with 2 orthogonal rotational joints with non zero distance between rotational axes (Cardan joint).

Direct Kinematics of the robotic hand is based on Denavit–Hartemberg (DH) convention. DH table for each finger are reported in tab. 1.1–1.5.

1.3.0.1 Fixed Frame Trasformation

From table 1.1–1.5 one can easily compute homogeneous transformation matrices for each finger separately.

Finally, to connect every finger to a fixed frame (for example, in the centre of the palm as in fig. 1.4), another homogeneous transformation has to be computed.

1.3.1 Tendons

Robotic hand joints are actuated by tendons and their wrapping on actuating motor pulleys has to be considered in direct kinematics.

Here I consider tendons as non elastic wires with one end fixed on the actuating motor pulley and the other fixed on a generic link.

First of all, for each joint, it is possible to define the *extension function* as $h_i : \mathbb{Q} \to \mathbb{R}$. The *extension function* describes the displacements of tendon ends w.r.t the joint variables. Generally, the *extension function* is non linear.

Therefore, starting from a geometric sketch of a tendon powered joint, as reported in fig. 1.5a, we can compute

$$\overline{AC} = \sqrt{a_1^2 + b_1^2} \qquad \overline{BC} = \sqrt{a_2^2 + b_2^2}$$

$$\beta_1 = \tan^{-1}\left(\frac{a_1}{b_1}\right) \qquad \beta_2 = \tan^{-1}\left(\frac{a_2}{b_2}\right) \tag{1.1}$$

$$\alpha = A\hat{C}B = \pi - \theta - \beta_1 - \beta_2.$$

Now, applying the Carnot Theorem to the triangle ACB, it is possible to write

$$\overline{AB} = \sqrt{a_1^2 + b_1^2 + a_2^2 + b_2^2 - 2\cos\alpha\sqrt{a_1^2 + b_1^2}\sqrt{a_2^2 + b_2^2}} \tag{1.2}$$

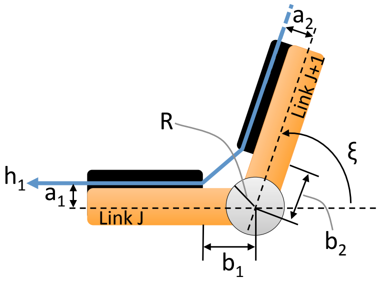

(a) Generic Joint

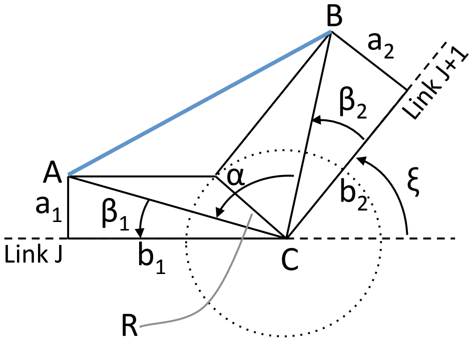

(b) Geometric Feature

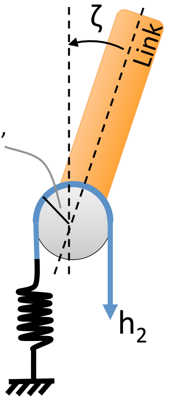

(c) Abduction Joint

Figure 1.5: Schematic of the joints type in *The First Hand*: generic joint 1.5a and its geometric feature 1.5b and abduction joint 1.5c.

Moreover, defining l_i as the nominal extension ($\theta = 0$), we can compute the *extension function* as

$$h_i(\theta) = l_i + AB - b_1 - b_2. \tag{1.3}$$

Now, it is possible to link the motor pulley wrapping W_m to the joint variable θ as

$$W_m = R_m \theta_m = l_i - h_i(\theta), \tag{1.4}$$

where R_m is the motor pulley radius, θ_m is the motor wrapping angle.

Hence, the relation between the joint angle and the motor angle is

$$\theta_m = \frac{l_1 - h_1(\theta)}{R_m} = f(a_1, b_1, a_2, b_2, \theta, R_m) \tag{1.5}$$

For abduction or arch palmar joint (see also fig. 6.11) the *extension function* is

$$h_e(\theta) = l_i \pm R'\theta' \tag{1.6}$$

where l_i is the nominal extension ($\theta' = 0$), R' is joint radius and θ' s the joint angle.

Now it is possible to link the abduction joint angle (θ') to the wrapping angle as

$$\theta_m = \pm \frac{R'\theta'}{R_m} \tag{1.7}$$

with positive sign if with positive angle the tendon gets shorter.

1.4 Inverse Kinematics

As discussed in section 1.3, I can consider the fingers as serial robots of 4 DoFs (thumb, little), 3 DoFs (index and ring) or 2 DoFs (medium).

If we want to determine the joint positions given only the position of the fingertips, i.e. the position of the end effectors, I have to take into account the position redundancy of the fingers.

This leads to implement an algorithmic method for solving inverse kinematics.

Briefly, I recall the general method to compute the inverse kinematics of a redundant serial robot. Starting from the position error defying as

$$e_p = p_d - p \tag{1.8}$$

where p_d and p represent the desired position and the current position of the *end-effector* respectively, it is possible to compute the derivative of the position error is

$$\dot{e}_p = \dot{p}_d - \dot{p}. \tag{1.9}$$

Moreover, remembering that

$$\dot{p} = J_p \dot{q}, \tag{1.10}$$

where J_p is the geometric Jacobian, equation 1.9 becomes

$$\dot{e}_p = \dot{p}_d - J_p \dot{q}. \tag{1.11}$$

Now, choosing a relation between the joint velocity $\dot{q}$ and the position error e_p which guarantees the convergence to zero of the position error, as

$$\dot{q} = J_p^{\dagger} \dot{p}_d - J_p^{\dagger} e_p, \tag{1.12}$$

it is possible to implement an iterative algorithm for the inverse kinematics as reported in the block diagram of fig. 1.6 .

Since one is interested to a motion point-to-point we can assume $\dot{p}_d = 0$.

Implementing inverse kinematics algorithm one has to take into account the coupling between the last two phalanges for index, medium, ring and little and the kinematic redundancy for the thumb and the little.

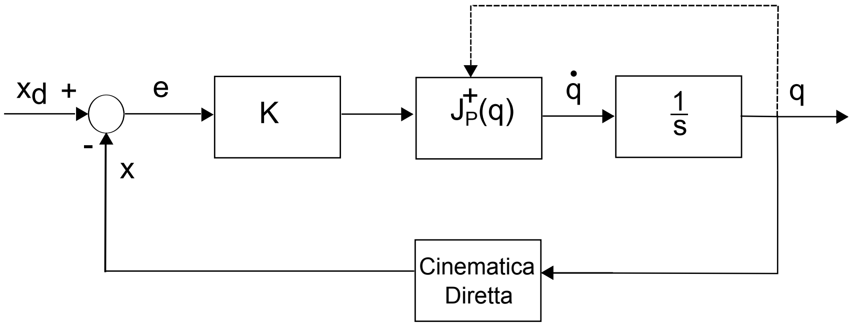

Figure 1.6: Block diagram of the inverse kinematic algorithm.

1.4.0.1 Inverse Kinematics with Fictitious Link

The coupling between phalanges can be represented as in figure 1.7.

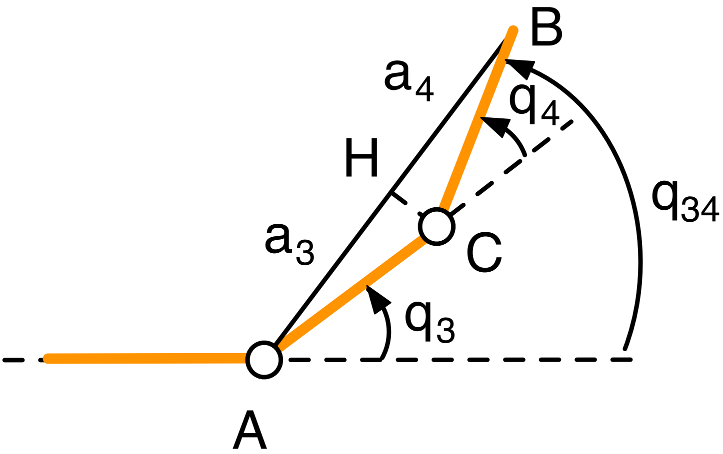

Figure 1.7: Model of a finger with fictitious link

To obtain a mathematical model it is possible to take into account the fictitious link $\overline{AB}$ and the fictitious angle q_{34}; it should be noted that the length of the link depends directly on the value of the joint angle. Assuming that $q_3 = kq_4$ and $a_3 = a_4$ it is possible to write

$$A\hat{C}B = \pi - q_4, \tag{1.13}$$

$$B\hat{A}C = \frac{\pi - A\hat{C}B}{2} = \frac{q_4}{2}, \tag{1.14}$$

$$\overline{AH} = \overline{AC}\cos(B\hat{A}C) = a_3 \cos(\frac{q_4}{2}), \tag{1.15}$$

$$\overline{AB} = a_{34} = 2a_3 \cos(\frac{q_4}{2}), \tag{1.16}$$

$$q_{34} = q_3 + \frac{q_4}{2} = q_3 + \frac{kq_3}{2} = q_3(1 + \frac{k}{2}), \tag{1.17}$$

and noting that

$$q_4 = \frac{q_3}{k} = \frac{q_{34}(1 + \frac{k}{2})^{-1}}{k} \tag{1.18}$$

finally one obtains

$$a_{34} = 2a_3 \cos\left(\frac{q_{34}(1 + \frac{k}{2})^{-1}}{2k}\right) \tag{1.19}$$

When the angle of fictitious joint q_{34} and its length a_{34} are found, it is possible to compute the Jacobian matrix relative to the system of fig 1.7. This Jacobian can be used in the inverse kinematic algorithm presented in the previous section.

1.4.0.2 Inverse Kinematics with Synergies

A different approach for considering the coupling between the last two phalanges of the fingers arises by the introduction of the synergy matrix (for more detail see [20]). In fact it is possible to write

$$q = S\sigma \tag{1.20}$$

where $S \in \mathbb{R}^{n_q \times n_s}$ is the synergy matrix and σ the value of the synergy actuation. To take into account the coupling between the last two phalanges it is possible to write

$$S_{index} = \begin{bmatrix} 1 & 0 & 0 \\ 0 & 1 & 0 \\ 0 & 0 & 1 \\ 0 & 0 & k \end{bmatrix}, \qquad S_{medium} = \begin{bmatrix} 1 & 0 \\ 0 & 1 \\ 0 & k \end{bmatrix}, \tag{1.21}$$

$$S_{ring} = \begin{bmatrix} 1 & 0 & 0 \\ 0 & 1 & 0 \\ 0 & 0 & 1 \\ 0 & 0 & k \end{bmatrix}, \qquad S_{little} = \begin{bmatrix} 1 & 0 & 0 & 0 \\ 0 & 1 & 0 & 0 \\ 0 & 0 & 1 & 0 \\ 0 & 0 & 0 & 1 \\ 0 & 0 & 0 & k \end{bmatrix}. \tag{1.22}$$

Remembering that

$$\dot{x} = Jq = JS\sigma \tag{1.23}$$

the matrix JS can be used inside the inverse kinematics algorithm instead of the Jacobian J. With this approach the convergence to an achievable configuration is garanteed.

1.4.1 Inverse Kinematics with Redundancy

The thumb and little of *THE First Hand* have 4 DoF. Imposing just a desired position for the end-effector, one can apply the inverse kinematics algorithm with redundancy. It is possible to approach the problem using the relation

$$\dot{q} = J^{\dagger} e_p + (I - J^{\dagger} J)\dot{q}_0 \tag{1.24}$$

where $(I - J^{\dagger} J)$ is a projector in $\ker(J)$ and the vector $\dot{q}_0$ is chosen as

$$\dot{q}_0 = k_0 \left(\frac{\partial w(q)}{\partial q} \right)^T, \qquad k_0 > 0 \tag{1.25}$$

with the *target function* $w(q) \in \mathbb{R}$ as

$$w(q) = -\frac{1}{2n} \sum_{i=1}^{n} \left(\frac{q_i - \bar{q}_i}{q_{iM} - q_{im}} \right)^2, \tag{1.26}$$

where q_{iM} and q_{im} are minimum and maximum value of the joint angle respectively, and $\bar{q}_i$is its medium point.

1.5 Grasp Trials

In this section we will show two set of experiments: in the first one we report snapshots of some grasp performed with the robotic hand. In the second set we perform an optimal control problem in grasping object.

1.5.1 Static Grasps

To test the effective performances of the robotic hand, trial grasps of several objects with different shapes were performed. Fig. 1.8 shows some of this grasps.

1.5.2 Dynamic Grasp

In the absence of applied external wrench on the object grasped, the grip conditions are described by equations

(a) Ball Grasp

(b) Pincer Grasp

(c) Stapler Grasp

(d) Scissor Grasp

(e) Syringe Grasp

Figure 1.8: Some experimental grasps performed with the proposed hand. Grasps are performed both on simple geometrical shapes (panels 1.8a) and on more complex shapes (panels 1.8b - 1.8e).

$$\begin{cases} Gf = 0 \\ \tau = J^T(q)f \end{cases} \tag{1.27}$$

where $G = \tilde{G}H^T$, $J = H\tilde{J}$ and H is the *selection matrix* dependent on the characteristics of the contacts. From (1.27) follows that $f \in \mathcal{N}(G)$ and $\tau \in \mathcal{R}(J^T)$. In a quasi-static formulation, introducing elasticity in contact points, the contact force variation δf and the torque variation $\delta\tau$ can be written as

$$\delta f = K_f J(q_t)\delta q = K_f J(q_t)(q - q_t) \tag{1.28}$$

$$\delta\tau = K_\tau(\delta q_r - \delta q) = K_\tau(q_r - q_t - q + q_t) = K_\tau(q_r - q) \tag{1.29}$$

where q_t, q_r, q are the initial configuration (tangent), the reference configuration and the real configuration respectively.

From these consideration follows that the system (1.27) can be written as

$$\begin{cases} GK_f J(q_t)(q - q_t) = 0 \\ K_\tau(q_r - q) = J^T(q_t)K_f J(q_t)(q - q_t). \end{cases} \tag{1.30}$$

Given the initial configuration, the value of the variables q_r and q minimizing a proper function has to be found.

This method is applied to *THE First Hand* studying the problem of a ball grasp just with the thumb and the little. Assuming contact point as *point-contact with friction*, the selection matrix results in

$$H_i = \begin{bmatrix} 1 & 0 & 0 & 0 & 0 & 0 \\ 0 & 1 & 0 & 0 & 0 & 0 \\ 0 & 0 & 1 & 0 & 0 & 0 \end{bmatrix}. \tag{1.31}$$

Admissible forces are those the remains inside the friction cone. It means that the following relations must hold

$$\begin{cases} \sqrt{f_{t1}^2 + f_{t2}^2} \leq \mu f_n \\ f_n \geq 0. \end{cases} \tag{1.32}$$

Starting from the knowledge of the contact point, using inverse kinematics we can obtain the value of q_t. Globally the problem is composed by:

- a cost function to minimize:

$$V = \parallel \tau \parallel_2 \tag{1.33}$$

- a linear equation set as $C_{eq}(x) = 0$:

$$\begin{cases} GK_f J(q_t)(q - q_t) = 0 \\ K_\tau(q_r - q) - J^T(q_t) K_f J(q_t)(q - q_t) = 0 \end{cases} \tag{1.34}$$

- a linear inequality set as $C_{ineq}(x) \leq 0$:

$$\begin{cases} \sqrt{f_{t1}^2 + f_{t2}^2} - \mu f_n \leq 0 \\ -f_n \leq 0 \end{cases} \tag{1.35}$$

The problem was implemented in $MATLAB$ by using the *fmincon* function.

Numerical results are obtained with a friction factor $\mu = 1.5$, a contact stiffness $K_f = 3$ N/m, a joint stiffness $K_\tau = 300$ Nm/rad. Below are the graphs with the evolution of position error during the execution of the algorithm of inverse kinematics with synergies. Similar results are obtained using the method of fictitious link.

$$q^t_{thumb} = \begin{bmatrix} 0.1164 \\ 1.0472 \\ 1.5708 \\ 1.2392 \end{bmatrix} \qquad q^t_{index} = \begin{bmatrix} 0 \\ 0 \\ 0.9599 \end{bmatrix} \tag{1.36}$$

Moreover, in fig. 1.9 and 1.10 the results for the inverse kinematic of the index and thumb are reported, respectively.

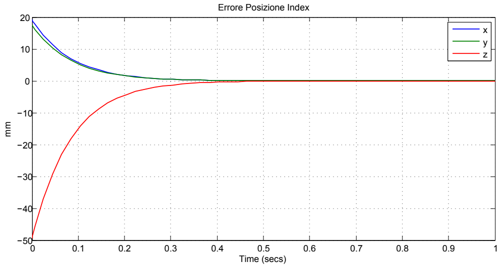

Figure 1.9: Position error during the execution of the inverse kinematics algorithm for the index.

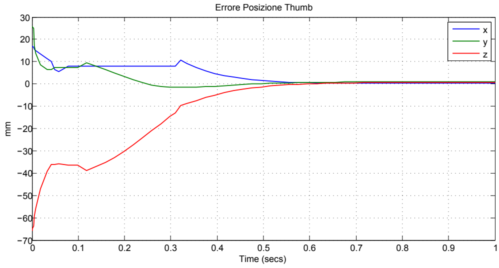

Figure 1.10: Position error during the execution of the inverse kinematics algorithm for the thumb.

Finally, in fig. 1.11 and 1.12 I report the algorithm results with simulations and experiments on *The First Hand*, respectively.

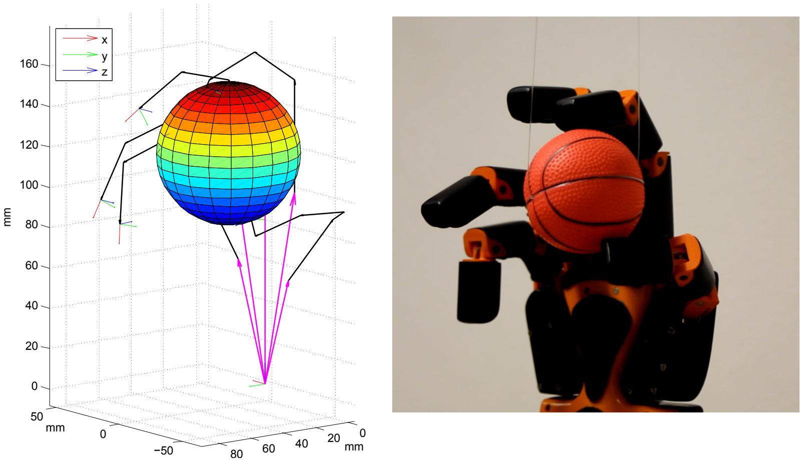

Figure 1.11: Starting configuration for the hand in simulation (on the left) and in experiment (on the right)

Figure 1.12: Starting configuration (on the left), final configuration (on the right)

Chapter 2

PISA–IIT SoftHand

In this chapter I retrace the evolution of adaptive synergies highlighting the differences with actuation approaches conceived for robot hands. Moreover, I presents the evolution of the design of hand prototypes implementing adaptive synergies, from the preliminary proof-of-concept of [41] to the integrated human-shaped PISA–IIT SoftHand, giving some details about the hand kinematics and mechanics. Finally, the grasping capabilities of the proposed hand are demonstrated by reporting some experimental results (for more details on this chapter see [A2] and [A3]).

2.1 Synergies for Robotic Hands

Focusing on grasping, [20] shows that most of the grasping hand movement can be explained, in terms of statistical variance, just by the first two or three principal components or *synergies*. A direct consequence of [20], was a new boost to the development of under-actuated and simplified hands, as that proposed in [42], which first exploited the idea of synergies in a mechanical way.

The synergy framework finds application in hand control, both for posture definition [43] and force/impedance management [44] and

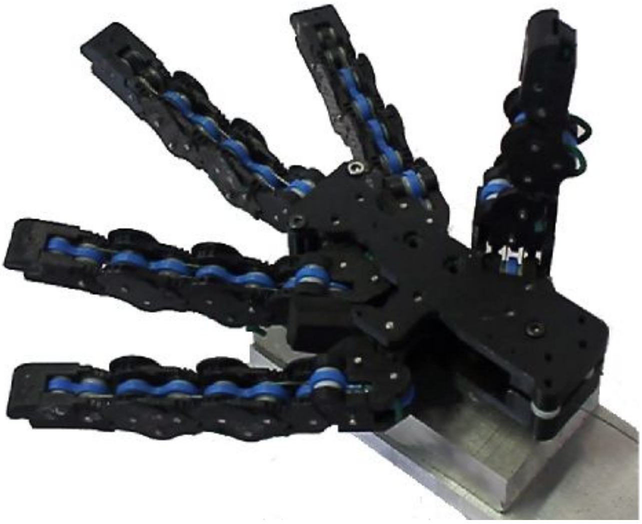

Figure 2.1: The PISA–IIT SoftHand, a self-contained humanoid robotic hand powered by adaptive synergies.

has, henceforth, developed theoretically with the introduction of *soft synergies* first, [21], and more recently, with *adaptive synergies* [41], where a preliminary mechanical implementation was proposed. Nevertheless, to easily comply and fruitfully integrate in a world developed after and around human hands, non-human shaped grippers, as that proposed in [41], still need to overcome possible geometric mismatches in order to achieve performance comparable to that of humanoid hands.

This work, retraces the concepts of soft and adaptive synergies within the rigorous twist notation framework, [45]. This allows to demonstrate their substantial equivalence, clearly stating the conditions in which a soft-synergy hand behaves like an adaptive-synergy one and vice-versa.

Later on, I present the first implementation of the PISA–IIT SoftHand, a prototype which conciliates the idea of adaptive synergies for actuation with an high degree of integration, thus yielding a human-shaped robotic hand with adaptive synergies, whose grasping performance are shown in some experiments.

2.1.1 Fully Actuated Hands

Before introducing under-actuation, I briefly present the equations describing a grasp made by a completely actuated robotic hand. This section shows how the movement of the whole system can be described knowing the joint displacement.

The notation adopted in this section is explained in Table 2.1. More details about the analytical description of the grasp can be found in [46].

Now, It is possible to consider the equilibrium equation for the grasped object. Let $w_e^o \in \mathbb{R}^6$ be the external wrench acting on the object and $f_h^o \in \mathbb{R}^c$ be the forces that the hand exerts on the object, where the dimension c depends on the number and type of contact points. Introducing the *grasp matrix* ${}^oG \in \mathbb{R}^{6\times c}$ referred to reference frame attached to the object, the equilibrium condition is verified when

$$w_e^o + {}^oG f_h^o = 0. \tag{2.1}$$

Since the grasp matrix is constant, by differentiation of (2.1) it follows that, for the first order variation of the equilibrium configuration, it holds

$$\delta w_e^o + {}^oG \delta f_h^o = 0. \tag{2.2}$$

Similarly, the equilibrium equation for the hand relates the contact forces with the joint torques ($\tau \in \mathbb{R}^{\sharp q}$) by the equation

$$\tau = {}^o\mathcal{J}^T f_h^o, \tag{2.3}$$

where ${}^o\mathcal{J}^T \in \mathbb{R}^{\sharp q\times c}$ is the transpose of the hand Jacobian matrix. It is worth observing that, since the contact forces are expressed in a frame attached to the object, the Jacobian matrix depends both on the hand configuration $q \in \mathbb{R}^{\sharp q}$ and the object configuration $u \in \mathbb{R}^6$. The general relationship describing a perturbation of the system can be found differentiating the equation (2.3), obtaining

$$\delta\tau = \bar{\Omega}\delta q + \bar{U}\delta u + \bar{J}^T \delta f_h^o, \tag{2.4}$$

where $\Omega = \frac{\partial {}^oJ^T f_h^o}{\partial q} \in \mathbb{R}^{\sharp q \times \sharp q}$ and $U = \frac{\partial {}^oJ^T f_h^o}{\partial u} \in \mathbb{R}^{\sharp q \times 6}$.
The hand/object interaction can be described introducing a virtual spring at the contact points. A force variation occurs in presence of a hand or object contact point displacements, that is

$$\delta f_h^o = K_c({}^o\bar{J}\delta q - {}^oG^T \delta u), \tag{2.5}$$

where $K_c \in \mathbb{R}^{c \times c}$ is the contact stiffness matrix.

Equations (2.2), (2.4) and (2.5) can be grouped the system

$$\begin{bmatrix} I_{\sharp w} & 0 & {}^oG & 0 & 0 \\ 0 & I_{\sharp\tau} & -{}^o\bar{J}^T & -\bar{\Omega} & -\bar{U} \\ 0 & 0 & I_{\sharp f} & -K_c{}^o\bar{J} & K_c{}^oG^T \end{bmatrix} \begin{bmatrix} \delta w_e^o \\ \delta\tau \\ \delta f_h^o \\ \delta q \\ \delta u \end{bmatrix} = 0, \tag{2.6}$$

that appears as a linear and homogeneous system of equations in the form $A\delta y{=}0$, where $A{\in}\mathbb{R}^{r_a \times c_a}$ and $\delta y \in \mathbb{R}^{c_a}$ is the vector containing all the system variables. It is easy to find that the nullspace basis of matrix A has a number of columns equal to $c_a - r_a {=} \sharp w - \sharp q$. Since that, I can describe the perturbed configuration of the system knowing the external wrench variation and the displacements of the joint configuration. A formal method to obtain these relationships consists in acting on the coefficient matrix by the elementary Gauss operation for a block partitioned matrix. The final result of the procedure is a set of equations of the type

Notation	Definition
δx	variation of variable x
$\bar{x}$	value of x in the reference configuration
$\sharp x$	dimension of vector x
c	number of contact constraints
$q \in \mathbb{R}^{\sharp q}$	joint configuration
$\tau \in \mathbb{R}^{\sharp q}$	joint torque
$f_h^o \in \mathbb{R}^c$	contact forces exerted by the hand on the object
$u \in \mathbb{R}^6$	pose of the object frame
$q_r \in \mathbb{R}^{\sharp q}$	reference joint configuration
$\sigma \in \mathbb{R}^{\sharp \sigma}$	soft synergy configuration
$\varepsilon \in \mathbb{R}^{\sharp \sigma}$	soft synergy forces
$z \in \mathbb{R}^{\sharp z}$	adaptive synergy displacements
$\eta \in \mathbb{R}^{\sharp z}$	adaptive synergy forces
${}^oG \in \mathbb{R}^{6 \times c}$	grasp matrix in object frame
${}^o\mathcal{J} \in \mathbb{R}^{c \times \sharp q}$	hand Jacobian matrix in object frame
$S \in \mathbb{R}^{\sharp q \times s}$	soft synergy matrix
$R \in \mathbb{R}^{\sharp z \times \sharp q}$	adaptive synergy matrix

Table 2.1: Notation for Grasp Analysis.

$$\delta y_i = W_i \, \delta w_e^o + Q_i \delta q, \tag{2.7}$$

where δy_i one of the variables in δy.A general algorithm to obtain the equations in (2.7) starting from (2.6), called GEROME-B, was presented in [46]. The matrices W_i and Q_i are functions of the elements of the matrix A, their explicit form is here omitted for brevity.

From (2.7) it trivially follows that, without an external wrench variation. The absence of the external wrench is not a general assumption. However its contribution is negligible in order to study the controllability of the system by the hand with or without underactuation. All the variables can be found as a function of the joint displacements as

$$\delta y_i = Q_i \delta q. \tag{2.8}$$

2.1.2 Simplicity in Control

As hinted by neuroscience works, as [20], the brain controls the human hand as a whole. Particular patterns of muscular activation give rise to organized movements, which form a base set resembling the concept of *basis* of a vector spac [47], that is a minimal number of linearly independent elements that, under specific operations, generate all members of the given set. Such basis is referred to as the space of postural synergies, or eigengrasp space [43, 48].

What brings out the bio-aware synergy space from other possible choices for the base to describe the hand configuration is the astounding result that most of the hand grasp posture, actually 80%, is statistically explained by the first two synergies alone (and 87% by the first three). Similar results can be found regarding grasping forces, as shown in [48]. This renders the synergy space a preferable base for *simplification*. There already exists some robotics application in robotics which take advantage of the idea of synergies. To simplify control, *software synergies* can be simulate on a fully actuated robotic hands (as that of Fig. 2.2a), as suggested by [43]. This can highly simplify the design phase of a grasp, by reducing the number of control variables.

The basic idea behind the use of synergies in robotics consists in specifying a suitable base for the joint space movements, called *synergy matrix*, $S \in \mathbb{R}^{\sharp q \times \sharp \sigma}$, where $\sharp \sigma$ is the number of synergies used.

In this scenario, a hand configuration can be described in the synergy space by the vector $\sigma \in \mathbb{R}^{\sharp \sigma}$, with $\sharp \sigma \leq \sharp q$, as

$$q = S\sigma. \tag{2.9}$$

The possible applications of the synergy concept are not limited to software. Simplified robotic hands can be built, which embed *hardware synergies* in their mechanics to reduce the number of motors used to achieve most grasping tasks. The hand design by Asada [42], adopts two interchangeable set of pulleys to move the hand along two synergies, as in the simplified scheme of Fig. 2.2d.

In reducing the number of control variables/motors, both approaches [43] and [42] need to confront with the gap between the number of hands DoFs (Degrees of Freedom) and the number of actuated synergies. Projecting a generic grasp configuration on the lower-dimensional sub-space spanned by S implies some error in achieving the desired pose. The software synergy approach of [43] faces this by stopping the motion of each finger when it comes in contact with the grasped object, while a complementary actuation system, realized with memory-shape alloys, is proposed in [49] by the same authors of [42] to compensate for lacking DoAs (Degrees of Actuation).

2.1.3 Soft Synergies

An alternative to the former solutions is proposed by the introduction of *soft synergies* in [21]. Here synergies define the reference configuration of the hand (called virtual hand), toward which the real hand is attracted by a stiffness model. To describe this situation, for each joint I introduce a *reference variable* $q_r \in \mathbb{R}^{\sharp q}$, such that its displacements is given by

$$\delta q_r = S\delta\sigma. \tag{2.10}$$

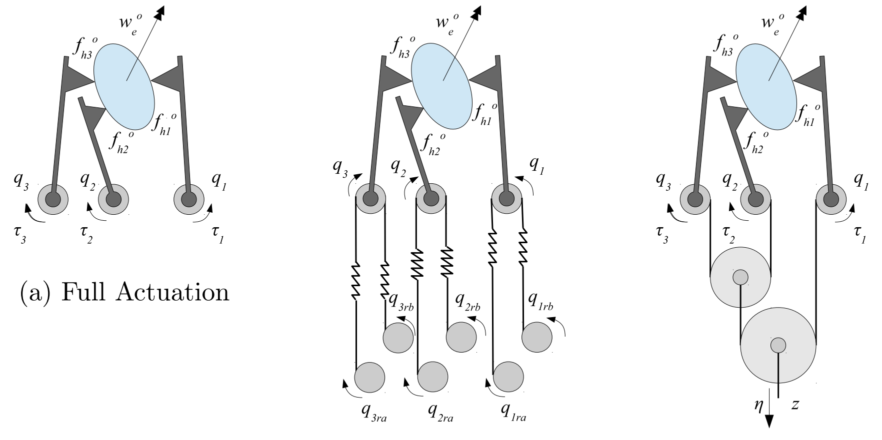

(a) Full Actuation

(b) Full VSA

(c) Adaptative UA

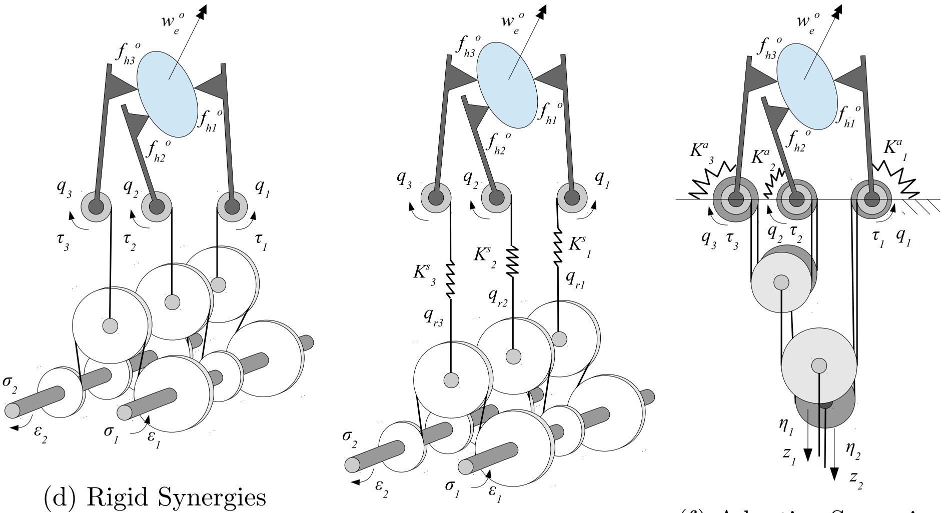

(d) Rigid Synergies

(f) Adaptive Synergies

(e) Soft Synergies

Figure 2.2: A simplified three-finger hand grasping an object, with concept implementation of different actuation paradigms.

The difference between the reference value and the real position of the hand generates the joint torque necessary to balance the repulsive forces given by contact with the grasped object. In other words, defining the matrix $K_q^s \in \mathbb{R}^{\sharp q \times \sharp q}$ as the joint stiffness matrix for the soft synergy case, for the joint torques $\tau \in \mathbb{R}^{\sharp q}$, I can write that

$$\delta\tau = K_q^s(\delta q_r - \delta q). \tag{2.11}$$

Furthermore, by kineto-static duality, letting the vector $\delta\varepsilon \in \mathbb{R}^{\sharp\sigma}$ be the force variation at the synergies, it is possible to prove that

$$\delta\varepsilon = S^T \delta\tau. \tag{2.12}$$

The differences between (2.9) and (2.10) highlight that a soft synergy hand retains all its kinematic DOFs, but is still able to simplify the grasp mechanics, leaving the burden of finely adjusting the $\sharp q - \sharp\sigma$ less important movements to the compliance model.

A concept scheme for the hardware implementation of this approach is shown in Fig. 2.2(e), where springs are used in series with a mechanism similar to that of Fig. 2.2(d). A software implementation of a similar approach is that implemented in [44] on the DLR HAND II, through the means of a suitable impedance controller. The soft synergy-like solution of [44] still requires full hand actuation and a sophisticate impedance controller on the hand. An hardware implementation could be realized on a hyper-realistic device, as that presented in [50], but such hardware, in principle similar to the scheme of Fig. 2.2(b), is actually twice as complex as that of a fully actuated hand.

Soft Synergy Hand Control

The effect of the synergistic under-actuation, described by (2.10), (2.11) and (2.12), can be taken into account in the equations (2.8). In particular for $i = 2$, thus for variable τ, I obtain simply that

$$\delta\tau = Q_\tau \delta q. \tag{2.13}$$

Substituting (2.13) in (2.11) and taking into account (2.10), it is easy to obtain

$$\delta q = (K_q^s + Q_\tau)^{-1} K_q^s S \delta\sigma. \tag{2.14}$$

Thus, from (2.8), it holds that

$$\delta y_i = Q_i (K_q^s + Q_\tau)^{-1} K_q^s S \delta\sigma. \tag{2.15}$$

The equation (2.14) and the system described by the (2.15) are able to give a complete description of the variation of the hand/object configuration given the position change at the synergy level.

To describe the situation where the soft synergies are controlled by forces, assessing (2.15) for the variable τ, placing it into (2.12), I can calculate the necessary force at the synergy level as

$$\delta\varepsilon = S^T Q_\tau (K_q^s + Q_\tau)^{-1} K_q^s S \delta\sigma. \tag{2.16}$$

Inverting the result I arrive to

$$\delta\sigma = (S^T Q_\tau (K_q^s + Q_\tau)^{-1} K_q^s S)^{-1} \delta\varepsilon. \tag{2.17}$$

Substituting (2.17) in (2.14), the hand joint displacement becomes

$$\delta q = (K_q^s + Q_\tau)^{-1} K_q^s S (S^T Q_\tau (K_q^s + Q_\tau)^{-1} K_q^s S)^{-1} \delta\varepsilon. \tag{2.18}$$

Therefore, substituting (2.18) in (2.8), the complete system variation depending on the soft synergy forces is also obtained.

2.1.4 Simplicity in Design

From early approaches, as [51], adaptive under-actuated hands evolved toward simplicity in design, such as those proposed in [52], [53] and [54]. To pursue this goal adaptive under-actuated hands make use of an approach based on differential transmissions, which distribute the displacements of a very small number of motors $z \in \mathbb{R}^{\sharp z}$, with $\sharp z \leq \sharp q$, to all the fingers actuating a linear combination of q, as in

$$R\delta q = \delta z. \tag{2.19}$$

as introduced in [41], $R \in \mathbb{R}^{\sharp z \times \sharp q}$ can be designed to be an *adaptive synergy matrix*, composed by the transmission ratios from the actuator to each joint. The scheme of Fig.2.2c shows a concept of this pattern of actuation. Adaptive synergies go a step past soft synergies by enabling a method to effectively exploit synergies for the design of under-actuated hands, compensating for the adoption of a reduced number of synergies with the possibility to adapt to the shape of the objects to be grasped. On the other hand, I go beyond traditional adaptive hands, by proposing a technique to combine multiple DOAs on the same under-actuated hand, in a way that each DOA globally actuates the whole hand and DOAs are hierarchically ordinated by a functional bio-inspired relationship.

Adaptive Synergy Hand Control

in order to find the hand/object displacements imposed by given adaptive synergies, I first look for the transmittable joint torques. Taking into account (2.19), from the kineto-static duality, R relates the force $\eta \in \mathbb{R}^{\sharp z}$ applied by the actuators to the torque τ on the joints by

$$\delta\tau = R^T \delta\eta. \tag{2.20}$$

The uniqueness of the free movement of the hand is assured by the introduction of elastic actions *in parallel* with the mechanical actuation system, as in Fig.2.2f. Thus, defining the joint stiffness matrix for the adaptive synergy case as $K_q^a \in \mathbb{R}^{\sharp q \times \sharp q}$, I can modify (2.20) in

$$\delta\tau = R^T \delta\eta - K_q^a \delta q. \tag{2.21}$$

Considering (2.21) and (2.13), it immediately follows that

$$\delta q = (K_q^a + Q_\tau)^{-1} R^T \delta\eta, \tag{2.22}$$

thus, substituting in (2.8), I can obtain the complete description of the hand/object displacements resulting from the application of forces at the synergy level.

To find a relationship describing the case of adaptive synergies controlled by the position, I start substituting the equation (2.19) in (2.22). Inversion allows to find that

$$\delta\eta = (R(K_q^a + Q_\tau)^{-1} R^T)^{-1} \delta z, \tag{2.23}$$

which is the expression of the synergy forces as a function of the synergy displacements. This result can be placed in (2.22) obtaining

$$\delta q = (K_q^a + Q_\tau)^{-1} R^T (R(K_q^a + Q_\tau)^{-1} R^T)^{-1} \delta z, \tag{2.24}$$

thus, substituting in (2.8), also the complete system description depending on the adaptive synergy displacements.

2.1.5 From Soft to Adaptive Synergies

I now look for a way to obtain an adaptive synergy matrix R and a joint stiffness matrix K_q^a able to imitate the effects of a given soft synergy under-actuation. In this sense, I suppose to know the joint stiffness matrix K_q^s and the soft synergy matrix S. Thus, from (2.14) and (2.18), I can suppose to know the term

$$\hat{S} = \begin{cases} (K_q^s + Q_\tau)^{-1} K_q^s S \\ (K_q^s + Q_\tau)^{-1} K_q^s S (S^T Q_\tau (K_q^s + Q_\tau)^{-1} K_q^s S)^{-1}, \end{cases} \tag{2.25}$$

where the first holds if the soft synergies are position controlled, the second otherwise. Since the matrix $\hat{S} \in \mathbb{R}^{\sharp q \times \sharp \sigma}$ is able to describe the joint displacements, and since from this depends all the hand/object motion, as by (2.8), I can say that to obtain the equivalent adaptive synergies means to obtain the same joint displacements. If I want to do that by a force controlled adaptive synergies I have to consider the equation (2.22), obtaining, under the hypothesis of $\sharp z = \sharp \sigma$, that

$$(K_q^a + Q_\tau)^{-1} R^T = \alpha \hat{S}, \tag{2.26}$$

where α is a non-null coefficient able to accord units of measurement. From (2.26) it immediately follows that

$$R^T = \alpha (K_q^a + Q_\tau) \hat{S}, \tag{2.27}$$

allowing to find suitable matrices R and K_q^a.

On the contrary, if I want to use a position controlled adaptive synergies, I have to consider (2.24), obtaining

$$(K_q^a + Q_\tau)^{-1} R^T (R (K_q^a + Q_\tau)^{-1} R^T)^{-1} = \alpha \hat{S}, \tag{2.28}$$

or equivalently

$$R^T = \alpha (K_q^a + Q_\tau) \hat{S} R (K_q^a + Q_\tau)^{-1} R^T. \tag{2.29}$$

It is easy to prove that (2.29) is satisfied only if

$$\hat{S} R = \frac{1}{\alpha} I, \tag{2.30}$$

where $I \in \mathbb{R}^{\sharp \sigma \times \sharp \sigma}$ is an identity matrix. Unfortunately, since in general $\hat{S}$ is a tall matrix and R is a fat matrix, the product $\hat{S} R$ can not be a full rank matrix, thus it is not possible to find a suitable position controlled adaptive synergy under-actuation able to imitate the effects of the given soft.

2.1.6 From Adaptive to Soft Synergies

Similarly to what seen before, I can search how to introduce a soft synergy actuation which imitates a given adaptive one, in terms of hand/object controllable displacements. Under this hypothesis, I can assume to know the adaptive synergy matrix R and the joint stiffness matrix K_q^a, that is the term

$$\hat{R}^T = \begin{cases} (K_q^a + Q_\tau)^{-1} R^T \\ (K_q^a + Q_\tau)^{-1} R^T (R Q_\tau (K_q^a + Q_\tau)^{-1} R^T)^{-1}, \end{cases} \tag{2.31}$$

where the first holds in the force control case, the second otherwise. In order to find an equivalent position controlled soft synergy, starting from (2.14), it is easy to obtain that

$$S = \beta (K_q^s)^{-1} (K_q^s + Q_\tau) \hat{R}^T, \tag{2.32}$$

where the coefficient β has the same function of α in (2.26).
It is worth observing that, considering (2.25) for the position controlled soft synergy case, and (2.31) for the force controlled adaptive synergy case, from (2.26) and (2.32), in the particular case of $K_q = K_q^s = K_q^a$, the map between the two under-actuation type is simply given by

$$R^T = \alpha K_q S, \tag{2.33}$$

in accordance with the results of [41].

Conversely, to find a suitable force controlled soft synergy, I have to consider the equation (2.18). Considerations similar to the previous allow to easily obtain the condition

$$\hat{R}^T S^T = \frac{1}{\beta} Q_\tau^{-1}. \tag{2.34}$$

Since the right hand term is a non-singular matrix, as for condition (2.30), it follows that even in this case it is not possible to solve the problem.

2.2 A Self-Contained Humanoid Hand

In the next section I show how adaptive synergies can be successfully implemented also in the design of a human-shaped hand. My purpose is to build a simple and robust human-shaped hand, which implements the concept of adaptive synergies, following the scheme of Fig. 2.2(f). The human hand has 19 DOFs, but its complexity can be approximated by a chain of 1 DOF joints (i.e. revolute joints), properly rotated to achieve flexion-extension, abduction-adduction and opposition movements. This simplified approach can be exploited to realize a hand out of only a few base modules.

The mechanical implementation of adaptive synergy dictates for the need to transfer simultaneously force and torque in a coordinated way for each DOF, implementing the transmission ratio R of (2.19).

A revised version of Hillberry's rolling joint [55] is, in the authors view, particularly suitable to realize this type of hand.

2.2.1 The Hillberry's Rolling Joint

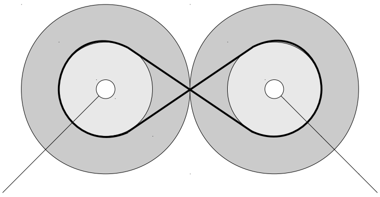

Figure 2.3: Schematics of Hillberry joint. It consists of two cylinders in rolling contact on each other. Hold together by a system of bands.

A Hillberry's joint consists of two pairs of cylinders in rolling contact on each other, as schematically shown in Fig. 2.3. Each of these two parts can be seen as a revolute joint. The two cylinders are held together through a system of bands, which can be rigid or elastic [55]. A Hillberry's joint exhibit many advantages:

1. The particular mechanical structure allows for easy modification of its characteristic diameters, thus changing the transmission ratio of the joint and therefore the transmitted force. Zero transmitted torque can be achieved by adequate tendon routing.
2. Joint friction is low, despite the lack of bearings.
3. The rotation range is about 180°, that covers the needed rotation range of about 90°.
4. It is easily scalable.
5. Absence of mechanical connection elements, like screws and bolts, is a major simplification.

Thanks to the presence of Hillberry's joint, an actuation system relying completely on tendons was achieved. The tendon carries the actuation and ensures also mechanical locking. The intrinsic elasticity of the joint, given by the elastic bands (in green in Fig. 2.4), allows to use an unidirectional actuation system. In particular, joint elasticity is determined by the bias of the elastic band from the (moving) contact point on the Hillberry's joint and can be, to some extent, adjusted by pretensioning the elastic band. The chosen implementation relies on a single cable acting on the whole hand and it gives adaptivity to the overall system, without the need for a differential gear mechanism (unlike the prototype presented [41]).

2.2.2 Robustness

In addition to the previously described features, another attribute of the joint is robustness. Indeed, in robots and humans, the hand is liable for crash, in particular during grasp and exploration movements. The designed joint is able to withstand severe disarticulations, as show in Fig. 2.5, exploiting the intrinsic system elasticity. The revisited Hillberry joint shows the following features:

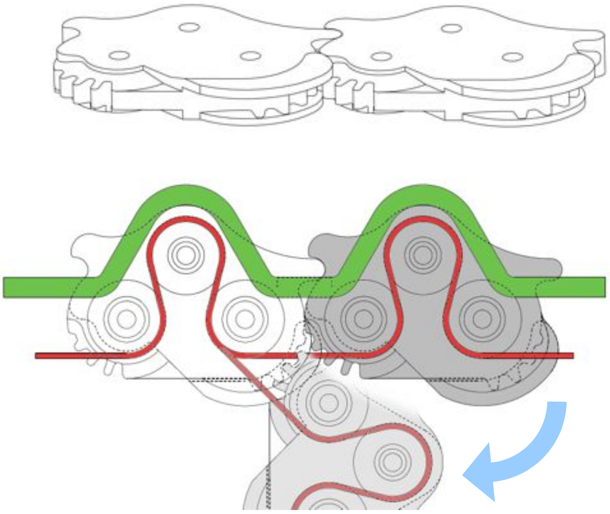

Figure 2.4: Revised version of Hillberry's joint (a) and profile view from the plane orthogonal to the rolling direction (b).

1. two cylindrical structures in rolling contact on each other,
2. lateral walls in each side of the joint, to ensure the following of the rolling profile, also in the case of transverse external forces. The walls present a slope of about 80°, as shown in Fig. 2.4 and Fig. 2.5. Each lateral wall is housed in a recess of the same dimension, properly designed in the other corresponding part of the joint.
3. An elastic tendon, locked at both ends with some pretensioning, which holds together the two parts of the joint and provides elasticity K^a.
4. A matching geared coupling integrated on rolling surface to constrain rolling contact. This profile is not that of a complete gear, but it's gradual (it can be seen in Fig. 2.4).
5. A small profile is included in the back of the joint, to ensure

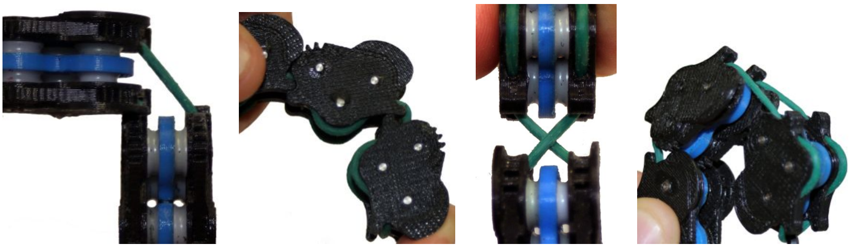

Figure 2.5: Example of disarticulations the designed joint is able to withstand.

correct return to the rest position in case of accidental over-opening of the joint.

6. Finally a series of ball bearings pulleys inside each joint, house the tendon actuation. The diameter of the pulleys range from 8 mm to 6 mm, with a wrapping radius of about 7 mm. A properly designed spacer, separates the pulley each from the other.

2.2.3 Hand Description

The whole hand is realized by the assembly of 20 modules, as showed in the exploded view of Fig. 2.6. In rest position, all the fingers are completely open and form an angle of about 30° one with respect the other. The thumb is rotated of 90° about its axis and is perpendicular to the palm, the full kinematics can be seen in Fig. 2.7.

Despite the integrated pulleys, friction ultimately limits, in practice, the number of joints that can be actuated by a single motor. This phenomenon is partly contained thanks to the tendon actuation which is realized pulling the tendon from both ends, allowing the implemented hand to perform satisfactorily. Further compensation for friction comes from proper choice of pulley radii, which is designed in order to let the real hand mimicry the first human hand synergy.

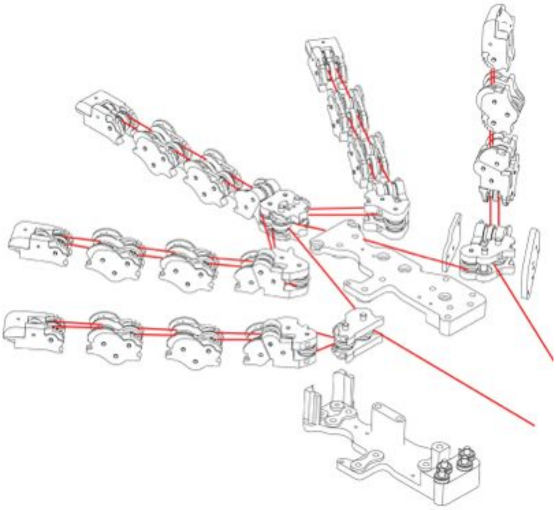

Figure 2.6: Exploded view of the modules of the whole hand.

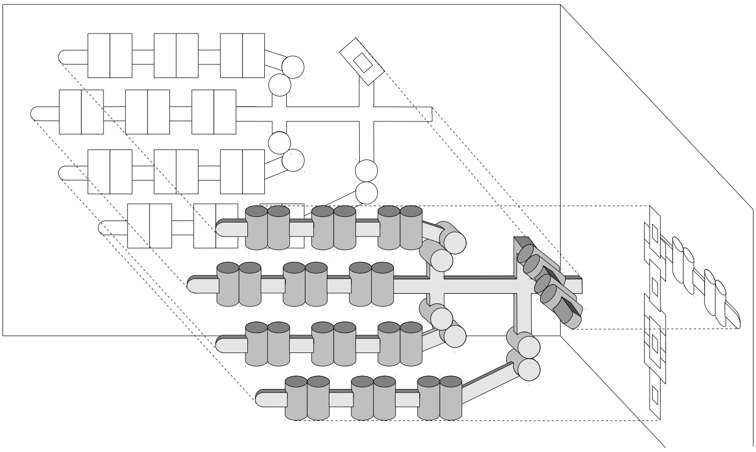

Figure 2.7: Schematics of the kinematics of the PISA–IIT SoftHand. As explained in the legend, rotation joints are represented by one light gray cylinder, while rolling joints are represented by a pair of dark gray cylinders.

2.3 Experiment

The proposed has been experimentally validated by measuring the maximum grasp force and holding torque and by grasping some common objects.

All the experiments and grasps of the following paragraphs rely on a PID control implemented on the motor position. The tendon was actuated by a $516 : 1$ $12\ V$ DC gear motor, equipped with a HEDS 5540 digital encoder (1024 counts per turn) and driven by Sabertooth Syren 10 driver. Encoder signals were acquired with a PhidgetsEncoder High Speed board while driver commands were sent trough a Phidget 4-Output board.

After calibration, the hand is controlled acting on the percentage of closure: from 0% (completely opened) to 100% (completely closed). In this manner it is possible to control the hand with a simple slider. For force and torque experiments I used an ATI nano 17 F/T sensor with UDP interface to measure holding force and torque of the robotic hand. The sensor was embedded in the two test objects of Fig. 2.8: a split cylinder (Fig. 2.8(a)) to measure the grasp force and a disk (Fig. 2.8(b)) to measure maximum holding torque.

Control and measurements were performed in MATLAB/ SIMULINK. During all the experiments the hand is equipped with an off-the-shelf rubber working glove to supply good contact friction. For grasp force experiments I used a cylinder of 120 mm height and diameter of 45 mm (see also Fig. 2.8(a)). For holding torque experiments I used a cylinder of 20 mm height and diameter of 95 mm (see also Fig. 2.8(b)). In Fig. 2.9a I report forces and torque acquisitions during sensorized object grasp.

2.3.1 Results

In Fig. 2.92.9b I report force acquisitions during sensorized object grasp. It is possible to notice how forces increased when fingers get in contact with the sensorized cylinder (step behavior of the red and

(a) Force Object

(b) Torque Object

Figure 2.8: Sensorized object for torque measurements (2.8b) and sensorized object for force measurements (2.8a).

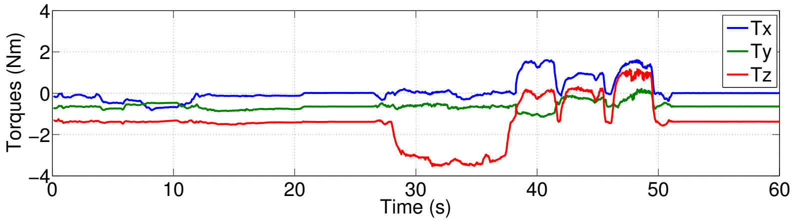

(a) Forces Measurements

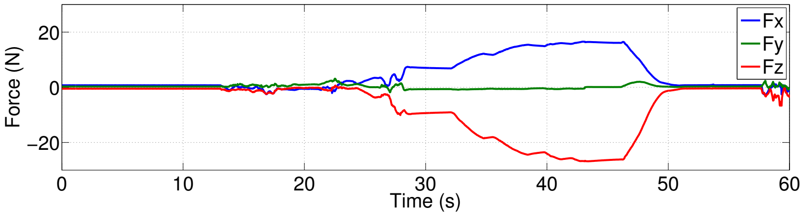

(b) Torque Measurements

Figure 2.9: Torques and forces of the robotic hand during grasp task.

blue line in Fig. 2.92.9b). I achieved a maximum holding torque of $3 \div 3.5$ Nm. I achieved a maximum holding force of about $25 \div 28$ N along z axis.

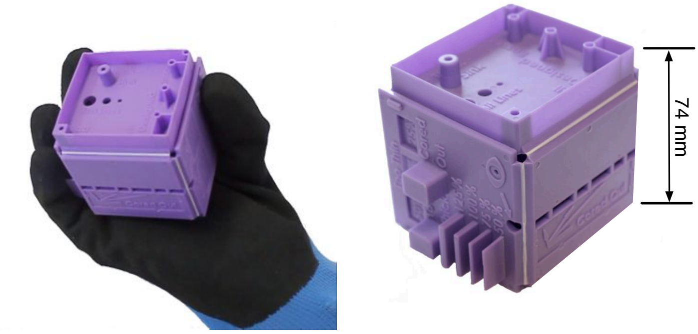

(a) Cube Grasp (b) Cube Dimensions

(c) Bottle Grasp (d) Bottle Dimensions

Figure 2.10: Some experimental grasps performed with the proposed hand on simple geometrical shapes.

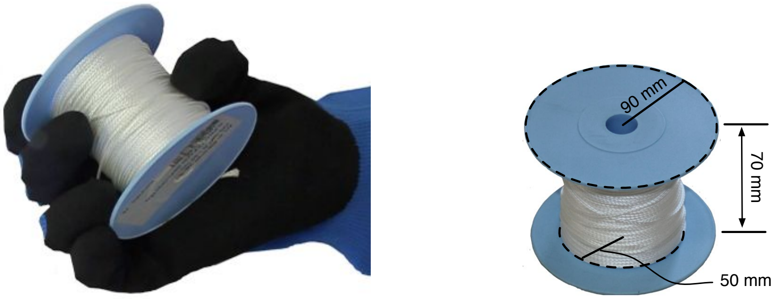

(a) Reel Grasp (b) Reel Dimensions

(c) Pincer Grasp (d) Pincer Dimensions

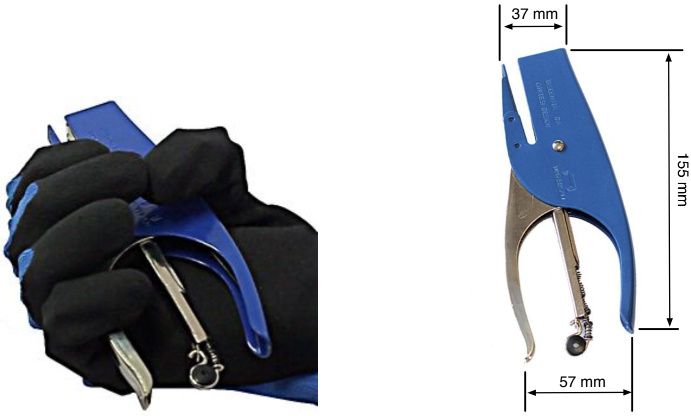

(e) Stapler Grasp (f) Stapler Dimensions

Figure 2.11: Some experimental grasps performed with the proposed hand on complex shapes.

Part II

Variable Impedance Observer

THIS PART presents a novel method to estimate variable impedance of Variable Stiffness Actuators (VSA).

In chapter 3, VSA devices with a generic classification are introduced. VSA devices are actuators capable to change both stiffness and link position using an elastic transmission mechanism of the motion between rotors and shaft. Their structure and mechanical implementation are very closed to human muscles.

After, the mechanical impedance estimation problem is tackled illustrating the theory and the structural properties of the methodology.

Performances of the method proposed are shown trough simulations on common models of VSAs and experiments on a real prototype.

Chapter 3

Variable Impedance Observer

This chapter introduce a method to estimate the mechanical impedance of Variable Stiffness.

Nowadays, VSA devices represents a wide research field of growing importance and interest both for research perspectives and for industrial applications. In fact, this new technology allows to completely change the way of thinking and building robots, and will replace the actual actuation system in robotics, allowing safety, saving energy, and preserving mechanisms.

Despite many solutions have been developed as prototypes, in VSA devices it is not possible to measure the time varying stiffness hindering the possibility of directly control the stiffness itself (further details can be found also in [A4] and [A5]).

3.1 Variable Impedance Actuator

While most of today's robots are built with rigid links and joints, recent robotic research shifted toward a new paradigm of intrinsically compliant robots. The first solutions of this kind introduced simple linear springs between the actuators and the links of a robot [56]. This approach was improved by realizing actuators with integrated adjustable stiffness, where springs, which could be tuned to the particular task in early prototypes [57], and could be adjusted in real-time on more recent devices ([58], [59] and [60]). Recently, devices which can also regulate damping or inertia have been proposed [61], thus generalizing Variable Stiffness Actuators (VSA) in Variable Impedance Actuators (VIA)

The overall trend aims toward the development of VIA [W12] that can adapt to the particular tasks and even during the task itself, changing the shape of their output dynamic characteristic, possibly with more than one degree of freedom.

Development of such novel actuators gives rise to interesting problems in term of control. A number of recent papers tackle the problem of controlling variable stiffness devices. Approaches, ranging from simple PD control [28] to more sophisticate feedback linearization techniques [29], are adopted to control stiffness in VIAs. Nevertheless, most of these approaches suffer from the same flaw: the impedance is not obtained trough direct measurements but it is inferred from the mathematical model of the device. Even if modeling an actuator in order to derive its stiffness seems like an easy and feasible approach, three main obstacles render it problematic.

First of all, the derivation of a model requires knowledge of the non-linear elastic mechanism of the actuator, and while this is possible today on prototypical devices, could not be facilitated or even hindered in tomorrow's commercial devices.

Second, derivation of impedance from a model requires fine calibration of the model parameters, in fact, due to intrinsic non-linearities of most VIAs, small errors in the model can badly propagate and produce large errors in the reconstruction of impedance.

Third, a model approach does not easily account for parameter variation due to wear, change in external condition (e.g. temperature) and unmodeled dynamics.

In a recent work [57], a stiffness observer was proposed as an alternative approach to face this problem. Without relying on a detailed model of the actuator, but rather using measurements of forces, posi-

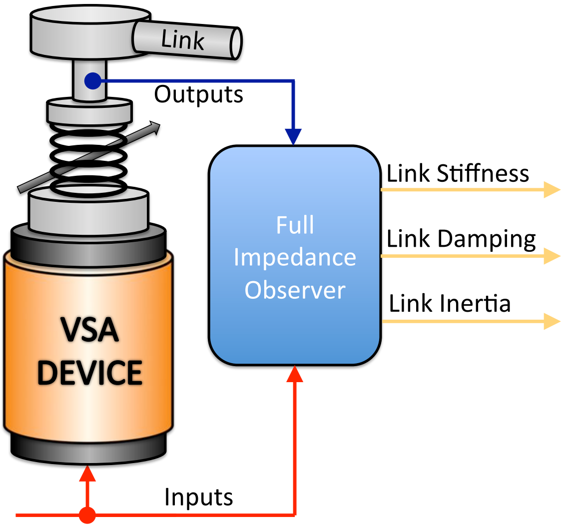

Figure 3.1: Concept of impedance observer for a variable stiffness robot: inertia, damping and stiffness on the link side are estimated from measures of inputs (motors currents) and outputs (angles and torques) of VSA device.

tions and their derivatives, the method is able to reconstruct the time-varying value of stiffness. Its application to the case of VSA-powered robots is partially restricted by the necessity of knowing estimates of damping and impedance of the link, although the algorithm shows some robustness to small errors on this information.

When linear impedance parameters are sufficient to model a system, standard estimation techniques exist to solve this problem, such as the Extended Kalman Filtering (EKF). Given proper calibration, their performance is satisfactory. A combined estimation approach is proposed to jointly observe non-linear stiffness and linear damping and inertia parameters. However, the first proposed implementation is not always practical: due to the fact that a loop between the two observers arises, robustness of the observation stability is severely un-

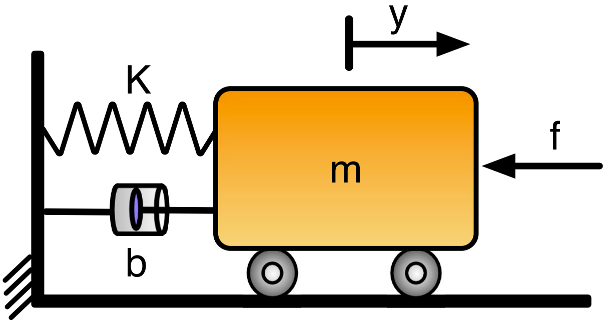

Figure 3.2: Classical spring, mass, damper dynamical system.

dermined.

Therefore I propose a technique for the combined estimation of the whole set of impedance parameters of a VIA powered system (as in Fig. 3.1), which avoids interacting observation loops, thus preserving robustness of the estimation. The derived method can be applied to a class of variable stiffness devices. Its practical feasibility is demonstrated by applying it to the estimation of the impedance parameters of the AwAS variable stiffness actuator, in simulations first and experimentally as a final verification.

3.2 Mechanical Impedance

To introduce impedance, consider first the paradigmatic example of a mass-spring-damper system (see fig. 3.2), described as a relation between the applied force $f(t)$ and position $y(t)$ through

$$f = m\ddot{y} + b\dot{y} + ky \tag{3.1}$$

the three parameters m, b, k are constant, the O.D.E. (3.1) is linear and time-invariant. Introducing the Laplace transforms $F(s), Y(s)$ of force and position, one has immediately

$$F(s) = (ms^2 + bs + k)Y(s). \tag{3.2}$$

The operator $Z(s) := (ms^2 + bs + k)$ is called the mechanical *impedance* of the spring-damper-mass system It should be noted that in the literature, the term *impedance* is sometimes used to denote the relationship between velocity and force. The reciprocal operator of impedance, called *admittance* $A(s)$, generalizes compliance as it maps forces in displacements: $Y(s) = A(s)F(s)$. The admittance operator is causal (while impedance is not).

The above approach can be generalized to a nonlinear dynamic setting by considering the relation between forces, displacements, first and second derivatives of displacements, and internal states u, and its graph $G \subset F \times Y \times DY \times D^2Y \times U$, comprised of 5-tuples $d(t) := (f(t), y(t), \dot{y}(t), \ddot{y}(t), u)$ corresponding to an idealized, infinite set of experiments. If $G(f, y, \dot{y}, \ddot{y}, u) = 0$ is an analytical description of the graph, and d_0 is a regular point, then a *force function* $f(y, \dot{y}, \ddot{y}, u)$ is defined in a neighborhood of d_0.

Defining *generalized stiffness* as

$$k(d) = -\left(\frac{\partial G(d)}{\partial f}\right)^{-1} \frac{\partial G(d)}{\partial y}, \tag{3.3}$$

generalized damping as

$$b(d) = -\left(\frac{\partial G(d)}{\partial f}\right)^{-1} \frac{\partial G(d)}{\partial \dot{y}}, \tag{3.4}$$

and *generalized mass* as

$$m(d) = -\left(\frac{\partial G(d)}{\partial f}\right)^{-1} \frac{\partial G(d)}{\partial \ddot{y}}, \tag{3.5}$$

one can compute the Frèchet differential of the force function as

$$\delta f = m(d)\,\delta\ddot{y} + b(d)\,\delta\dot{y} + k(d)\,\delta y + \nu(d)\,\delta u \tag{3.6}$$

From consideration of the positive definiteness of the kinetic energy, Rayleigh dissipation function, and elastic energy associated with the generalized inertia, damping and stiffness, it follows that m, b, and k are always greater than zero.

3.2.1 Observability for Linear Impedance

Consider an extended state vector $z = \begin{bmatrix} y & \dot{y} & -\frac{k}{m} & -\frac{b}{m} & \frac{1}{m} \end{bmatrix}$, and rewrite the dynamics of (3.1) as

$$\begin{aligned} \dot{z} &= \begin{bmatrix} z_2 \\ z_1 z_3 + z_2 z_4 \\ 0 \\ 0 \\ 0 \end{bmatrix} + \begin{bmatrix} 0 \\ z_5 \\ 0 \\ 0 \\ 0 \end{bmatrix} f \qquad (3.7) \\ y &= h(z) = z_1. \end{aligned}$$

The identification of the impedance parameters can thus be cast as a nonlinear state estimation problem, i.e., from the measurement of the external force f and position y, estimate the initial state $z(0)$, and in particular its three last components which completely determine the linear impedance.

I preliminarily establish that the problem is well posed. Indeed, considering the observability codistribution for this system,

$$\Omega(z) = \begin{bmatrix} 1 & 0 & 0 & 0 & 0 \\ 0 & 1 & 0 & 0 & 0 \\ z_3 & z_4 & z_1 & z_2 & 0 \\ 0 & 0 & 0 & 0 & 1 \\ z_3 z_4 & z_3 + z_4^2 & z_2 + z_1 z_4 & z_1 z_3 + 2 z_2 z_4 & 0 \\ 0 & 0 & 0 & z_5 & z_4 \end{bmatrix} \tag{3.8}$$

it turns out that for $m, b, k > 0$, $\mathrm{d}im\Omega(z)^{\perp} = 0$, $\forall z$ except $z_1 = z_2 = 0$. Hence, if the system moves from the equilibrium, the three linear impedance parameters can be reconstructed from position and force measurements.

To actually estimate the impedance in this case, different methods can be adopted. These include standard off-line identification techniques (which exploit the linear nature of the regressor for the unknown parameters), such as e.g. in [62], or on-line nonlinear state observers (e.g. Extended Kalman Filters) applied to system (3.7).

Unfortunately, generalization of the above straightforward approach to the case when impedance is nonlinear and/or time varying is not trivial. To convince oneself, it is sufficient to consider the case of an unknown force function $s(y, u(t))$ replacing the linear spring term in (3.1), i.e.

$$f = m\ddot{y} + b\dot{y} + s(y, u), \tag{3.9}$$

when no information on the structure of f or on the variable $u(t)$ is available.

In the case a parametric description of the force function is available, e.g. in terms of a finite polynomial expansion $f(y, u) = k_0(u) + k_1(u)y + k_2(u)y^2 + \ldots$, and u is constant, an observable finite dimensional nonlinear system can be built.

However, the possibility to achieve good performance of the corresponding observer is dubious.

3.3 Variable Impedance Actuator

Most of the VIA mechanisms are characterized by 3 degrees of freedom (DOFs) and, therefore, can be described by a similar common structure. I will assume here that a VSA can be modeled with one motor (indirectly) actuating the link movement and another motor actuating the impedance variation, as in Fig. 3.1, or:

$$\begin{cases} I\ddot{q} + N\dot{q} + \Sigma(\theta_2, \cdots) = \tau_{ext} \\ B_1\ddot{\theta}_1 + D_1\dot{\theta}_1 - \Sigma(\theta_2, \cdots) = \tau_1 \\ B_2\ddot{\theta}_2 + D_2\dot{\theta}_2 + \Gamma(\theta_2, \cdots) = \tau_2. \end{cases} \tag{3.10}$$

The first equation of (3.10) represents the dynamics of the link: I, N and $\Sigma(\theta_2, \cdots)$ are inertia, damping and the non-linear variable impedance of the link, respectively, τ_{ext} is the external torque on the link, q is the link angle. The second equation of (3.10) represents the dynamics of the position actuating motor: B_1 and D_1 are inertia and damping of the link motor, respectively, τ_1 is the motor torque and θ_1 is the motor angle. The third equation represents the dynamics of the impedance actuating motor: B_2 and D_2 are inertia and damping of the stiffness motor, respectively $\Gamma(\theta_2, \cdots)$ is the torque needed for the motors to change impedance and τ_2 and θ_2 are the motor torque and angle, respectively.

The functions

$$\Sigma(\theta_2, \cdots) = \Sigma(\theta_2, q - \theta_1, \dot{q} - \dot{\theta}_1, \cdots) \tag{3.11}$$

$$\Gamma(\theta_2, \cdots) = \Gamma(\theta_2, q - \theta_1, \dot{q} - \dot{\theta}_1, \cdots), \tag{3.12}$$

represent the *variable impedance* part of the system. Their effective structure and the set of their arguments itself depend on the particular

VIA system considered, but it can usually be restricted to the values of θ_2 , $q - \theta_1$ and their derivatives. In the case of a VSA, i.e. a VIA where damping and inertia are constant, the arguments of $\Sigma()$ and $\Gamma()$ usually reduce to just θ_2 , $q - \theta_1$, respectively.

3.3.1 VIA Classification

VIA systems can be classified into two categories:

- Constant compliance devices
- Variable compliance devices

A constant compliance device has a fixed stiffness in the elastic transmission between rotor and shaft. The system can adapt to the situations only changing the elastic element and has only one motor. Instead, in the second case, compliance can be changed adapting to the situation, as moving a heavy load or move a glass of liquid. There is the necessity of an extra motor to change compliance resulting in an increased complexity of the system. Compliance is altered by varying stiffness of the elastic element, hence it is commonly referred to as Variable Stiffness Actuators (VSA). In particular, in a quick variable compliance system, compliance can be changed with time constants comparable to motion.

At present, the variable stiffness devices (VSA) can fall into two categories:

- Explicit Stiffness Variators (ESV)
- Agonist-Antagonist (A.A.)

The ESV devices consist of two motors, one dedicated for the link movement, which transfers power (torque and velocity) to the joint, and the other dedicated to explicitly change the link stiffness. The A.A. devices have also two motors, but unlike the ESV, the two motors change both the link position and stiffness, affecting each other.

Therefore, their behavior is said agonist-antagonist, as the operation's principle of the biological muscles. In fact, if I consider to only change the link stiffness, keeping the link position fixed, this can be obtained by commanding the two motors to move in opposite directions.

From a more general point of view, it has to be pointed out that stiffness is one of the parameter that characterize the concept of mechanical impedance with mass and damping. Devices that can also regulate damping and inertia are called Variable Impedance Actuators (VIA).

3.4 Impedance Observer

It is possible to consider that the mechanical impedance of a VSA is composed by two part. First is the stiffness (time varying) and second is the mass and damping (time invariant).

In this section I explain the algorithm for estimating the mechanical impedance of a VSA dividing the estimation task in stiffness estimation and in mass and damping estimation.

3.4.1 Variable Stiffness Observer

For simplicity's sake, I assume that accurate measures of the applied force $f(t)$ and of the position $y(t)$ are available, and that numerical derivatives of these signals can be done. I assume also that both the mass and damping coefficients, m and b, are known (these strong assumptions will be discussed later on). No assumptions are made on the function $s(y, u)$ except that it is smooth in both arguments, with bounded derivatives of all orders.

I assume that the stiffness-regulating input $u(t)$ is bounded with its first derivative $\dot{u}(t)$. It should be noticed that, in building an observer that relies only on measurements of the position $y(t)$ corresponding to the external load $f(t)$, it is physically impossible to observe a stiffness which is changing in time ($\dot{u}(t) \neq 0$) while the system is at equilibrium

($\dot{y}(t) = 0$). More precisely then, I will make the assumption that the ratio between the stiffness regulation rate of change and the velocity of the measured trajectory is bounded, namely that, for all times t during the application of the observer, it holds

$$\frac{|\dot{u}(t)|}{|\dot{y}(t)|} < v \in \mathbb{R}, \quad \forall t. \tag{3.13}$$

Let $\frac{\partial f}{\partial y} = \frac{\partial s(y,u)}{\partial y} := \sigma(y, u(t))$ denote the stiffness to be measured. Also let $\hat{\sigma}(t)$ denote its estimate at time t, and $\tilde{\sigma}(t) = \sigma(y, u(t)) - \hat{\sigma}(t)$ be the estimation error.

Differentiate (3.9) once with respect to time to get

$$\dot{f} = m\dddot{y} + b\ddot{y} + \sigma\dot{y} + s_u\dot{u}, \tag{3.14}$$

where $s_u := \frac{\partial s(y,u)}{\partial u}$. Using the current estimate of stiffness and the assumptions stated above, a best-effort prediction for $\dot{f}$ can be written (in the absence of information on $s(y,u)$ and on $u(t)$) as

$$\dot{\hat{f}} = m\dddot{y} + b\ddot{y} + \hat{\sigma}\dot{y} \tag{3.15}$$

I will show that the update law

$$\dot{\hat{\sigma}} = \alpha\dot{\tilde{f}} sgn(y), \tag{3.16}$$

with $\alpha > 0$ and

$$sgn(x) := \begin{cases} \frac{x}{\|x\|} & \text{if } \|x\| \neq 0 \\ \\ 0 & \text{if } \|x\| = 0 \end{cases}, \tag{3.17}$$

is such that $\hat{\sigma}(t)$ can be made to converge to the true stiffness value $\sigma(t)$ within an uniformly ultimately bounded error.

Indeed, consider the positive definite error function

$$V_\sigma := \frac{1}{2}\tilde{\sigma}^2 \tag{3.18}$$

and its derivative along the trajectory defined in (3.16), i.e.

$$\dot{V}_\sigma = \tilde{\sigma}\dot{\tilde{\sigma}} = \tilde{\sigma}\dot{\sigma} - \tilde{\sigma}\dot{\hat{\sigma}} = \tilde{\sigma}\dot{\sigma} - \alpha\tilde{\sigma}s_u\,\dot{u}\,sgn(\dot{y}) - \alpha\tilde{\sigma}^2|\dot{y}|\ . \tag{3.19}$$

While the first two terms in the rightmost sum in (3.19) are indefinite in sign, the third term is negative definite. Therefore, wherever the inequality holds

$$|\tilde{\sigma}| > |s_u|\frac{|\dot{u}|}{|\dot{y}|} + \frac{1}{\alpha}\frac{|\dot{\sigma}|}{|\dot{y}|} \tag{3.20}$$

the derivative of the error function $\dot{V}_\sigma$ is negative, hence the estimation error decreases. By writing $\dot{\sigma} = \sigma_y\dot{y}+\sigma_u\dot{u}$, and using the upper bound above assumed on the rate of stiffness change, I have that stiffness estimates converge to the true value within an ultimately uniformly bounded error given by

$$|\tilde{\sigma}| > \frac{|\sigma_y|}{\alpha} + \left(|s_u| + \frac{|\sigma_u|}{\alpha}\right)v \tag{3.21}$$

Remark 3.1 *The assumption that the mass and damping are exactly known is not realistic. However, it is easy to verify that the analysis above carries over exactly even with no knowledge of m and b, provided that a force sensor directly placed on the elastic element provides a measure of the force $s(x,u)$. In case this is not available, then errors on the m and b parameters have the effect of making the ultimate error larger (this efect can be countered by increasing the observer gain α).*

3.4.2 Combined EKF-Stiffness Observer

Assuming that a measurement of the torque τ_{ext} is known, a possible approach to the combined estimation problem relies on the juxtaposition of a stiffness observer and an EKF. Rewriting (3.14) as

$$\dot{\tau}_{ext} - K(\dot{q} - \dot{\theta}_1) - \Sigma_u \dot{\theta}_2 = \dot{\tau}_* = I\dddot{q} + N\ddot{q} \ , \qquad (3.22)$$

an EKF can be easily built in to estimate the impedance parameters of the rightmost side given a measurement of $\dot{\tau}_*$. Given the estimates $\hat{I}$ and $\hat{N}$ derived from the EKF, the estimation of stiffness can be obtained by using the best-effort prediction for the $\dot{\tau}_{ext}$ defined now as

$$\dot{\hat{\tau}}_{ext} = \hat{I}\dddot{q} + \hat{N}\ddot{q} + \hat{K}(\dot{q} - \dot{\theta}_1) \ , \qquad (3.23)$$

where $\hat{\tau}_{ext}$, $\hat{I}$, $\hat{N}$ and $\hat{K}$ are the estimations of external torque, inertia, damping and stiffness, respectively.

By virtue of the robustness of the stiffness observer algorithm claimed in [57], the error on the knowledge of I and N should introduce only an error on the estimate K.

The knowledge of $\dot{\tau}_*$ is, unfortunately, unavailable but, possesing possessing an estimate of the stiffness K, can be approximate as

$$\dot{\hat{\tau}}_* = \dot{\tau}_{ext} - \hat{K}(\dot{q} - \dot{\theta}_1). \qquad (3.24)$$

This approach has the advantage of estimating the whole set of parameters using only torque and position measurement (and their derivatives) without needing any other assumption. It works under the hypothesis that the initial error on the estimates of I and N and the influence of the term Σ_u are small enough. Nevertheless, as it is highlighted from the block-diagram of Fig. 3.3, the problem of an interaction loop between the two observers arises. This has a negative effect on the stability of the algorithm, and can make convergence depend strongly on initial guesses. A solution to this problem is presented in the next section (3.4.3).

3.4.3 Decoupled Impedance observer

Assume that the torque sensor necessary for the stiffness estimation is assembled between the actuator unit and the link so as to measure

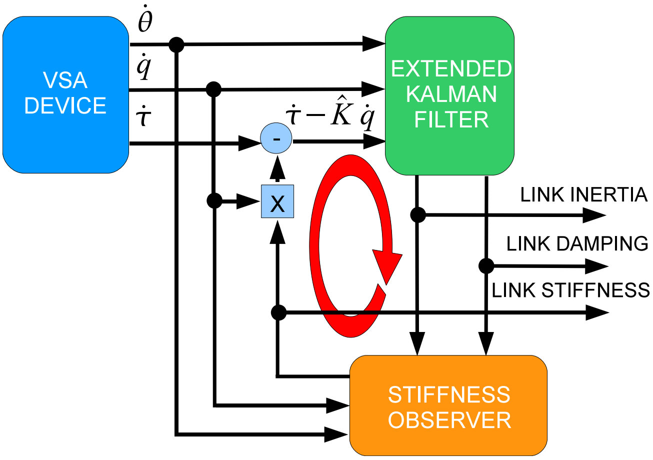

Figure 3.3: Schematics of the full observer as proposed in section 3.4.2. The interaction loop between the two observers is highlighted.

Σ. It is possible to notice, that the variable impedance term Σ, giving rise to the stiffness K, appears in both the first and second equations of (3.10). If I consider, in particular, the second equation of (3.10), its general form is identical to that needed by the stiffness observer. While accomplishing the stiffness estimation task on the first equation of (3.10) requires the knowledge of I and N, performing the estimate on the second of (3.10) demands just the knowledge of the motor parameters B_1 and D_1. Those values can be usually deduced by the motor data-sheets, or otherwise measured with standard off-line calibration techniques . Moreover, small errors in the knowledge of these two parameters are robustly tolerated, as shown in [57]. The rest of the problem, i.e. the estimation of the inertia I and the damping N, can be realized with a standard EKF on the system

$$I\ddot{q} + N\dot{q} = \hat{u}. \tag{3.25}$$

Defining the extended state vector

$$\begin{bmatrix} q \\ \dot{q} \\ 1/I \\ N/I \end{bmatrix} = \begin{bmatrix} x_1 \\ x_2 \\ x_3 \\ x_4 \end{bmatrix}, \tag{3.26}$$

allows to write the non linear discrete state representation of (3.25) as

$$\begin{cases} x_1^{(k+1)} = x_2^{(k)} T_c + x_1^{(k)} \\ x_2^{(k+1)} = (-x_3^{(k)} x_2^{(k)} - x_4^{(k)} \hat{u}^{(k)}) T_c + x_2^{(k)} \\ x_3^{(k+1)} = x_3^{(k)} \\ x_4^{(k+1)} = x_4^{(k)} \end{cases}, \tag{3.27}$$

where T_c is the sampling time. From (3.27), a suitable EKF can be designed which is effectively decoupled from the stiffness observer (for some details see the [63]). The stiffness observer, built in as explained in section 3.3, is discretized such as

$$\hat{K}^{(k+1)} = [\alpha \dot{\hat{\Sigma}} sgn(q^D - \theta_1^D)] T_c + \hat{K}^{(k)}, \tag{3.28}$$

with $\dot{\hat{\Sigma}}$ defined as

$$\dot{\hat{\Sigma}} \triangleq \Sigma^D - \hat{K}^D (q^D - \theta_1^D) - B_1 q^{DD} - D_1 q^{DDD}, \tag{3.29}$$

with x^D calculated, for a generic quantity x, as

$$[x^D]^{(k)} = \frac{x^{(k)} - x^{(k-1)}}{T_c}. \tag{3.30}$$

3.5 Simulations and Experiment

In order to test effective performances of the algorithm presented, simulations both ESV model an AwAS model are performed.

Moreover, I test the observer also on a real prototype of VSA.

In next sections the result of the simulations and experiment are reported.

3.5.1 Simulation with ESV Model

The impedance observer was tested through simulations on a ESV model, the Actuator with Adjustable Stiffness (AwAS), developed by the Italian Institute of Technology [64] (see Fig. 3.4). The dynamics of the AwAS actuator, neglecting the gravity, can be described by the following equations:

$$\begin{cases} I\ddot{q} + N\dot{q} + \tau_E = \tau_{ext} \\ B_1\ddot{\theta}_1 + D_1\dot{\theta}_1 - \tau_E = \tau_1 \\ B_2\ddot{\theta}_2 + D_2\dot{\theta}_2 + \tau_r = \tau_2 \end{cases} \tag{3.31}$$

where I, N and M are the inertia, damping and mass of the link with generalized coordinate q; B_i, D_i and τ_i with $i \in [1,2]$ are the inertia damping and command torque of the motors M_1 and M_2, respectively, with generalized coordinate θ_i. The external torque applied at the joint is represented with τ_{ext} and the elastic torque τ_E is formulated such as

$$\tau_E = k_s r^2 \sin(2\theta_s) \tag{3.32}$$

where k_s is the spring rate and $\theta_s = q - \theta_1$ is the spring deflection; the rotational stiffness $K = \frac{\partial \tau_E}{\partial \theta_s}$ is therefore obtained such as

$$K = 2k_s r^2 cos(2\theta_s). \tag{3.33}$$

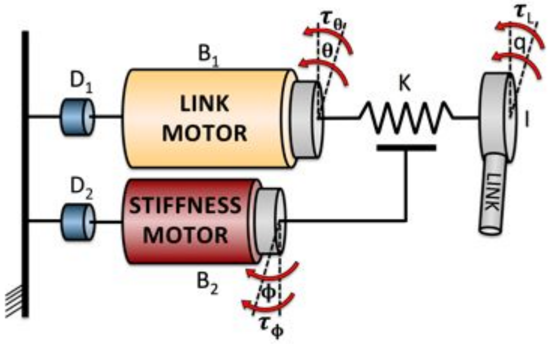

(a) AwAS Model

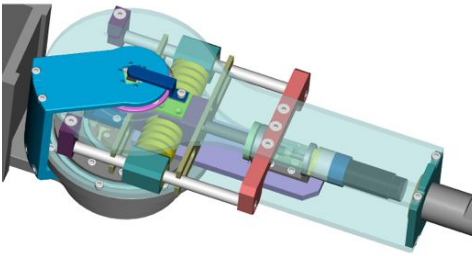

(b) AwAS Mechanical Implementation

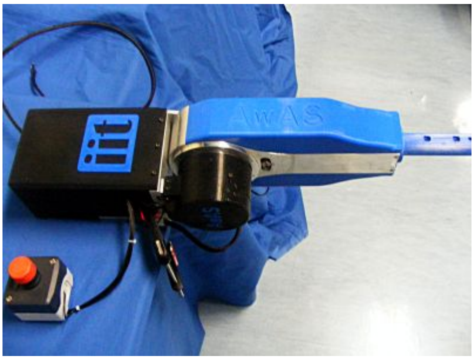

(c) AwAS Real Protoype

Figure 3.4: The Actuator with Adjustable Stiffness (AwAS) used as a testbed for the proposed impedance observer. Schematic 3.4a, CAD image 3.4b and prototype 3.4c.

The joint stiffness K depends on the lever arm r, which is the effective distance between the center of rotation of the joint and the springs, and, in minor contribution, from the deflection of the springs. The lever arm is adjusted through a ball screw mechanism through the actuator M_2 such as

$$r = r_0 - n\theta_2 \tag{3.34}$$

where n is the transmission ratio between the motor and the ballscrew and r_0 is the initial length. Finally, the torque τ_r which applies at the motor M_2 is given by

$$\tau_r = -2k_s nrsin(\theta_s)^2. \tag{3.35}$$

Note that, to simplify the notation the motors inertia and damping factors are already scaled by the transmission ratios.

Results of simulations are shown in Fig. 3.5. The simulated experiment consisted in feeding the two motors of the AwAS actuator with two sinusoidal torque signals. Parameters of the two observers are tuned as follows: the EKF matrices are

$$Q = 0.001 \times I_{4\times4}$$
$$R = 0.001 \times I_{2\times2},$$

with initial guesses

$$\begin{aligned} x_{0|0} &= \begin{bmatrix} 0 & 0 & 0 & 0 \end{bmatrix}^T \\ P_{0|0} &= 10000 \times I_{4\times4}. \end{aligned}$$

The stiffness observer gain (3.16) is set to $\alpha = 2000$.

3.5.2 Simulation with AA Model

In this section, I consider the AA VSA model which can be sketched up as in fig. 3.6 and can be described by the following set of equations

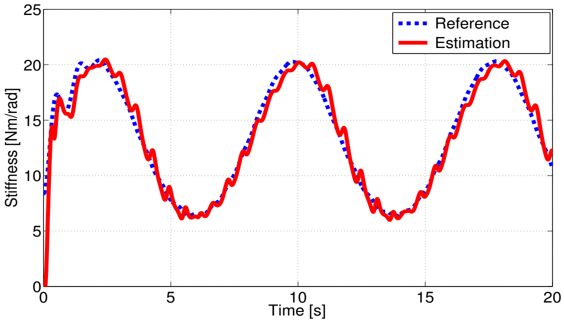

(a) Stiffness Estimation

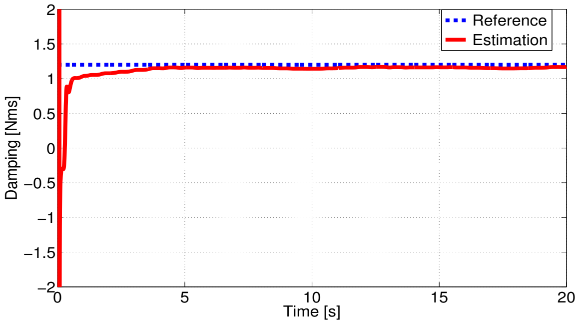

(b) Damping Estimation

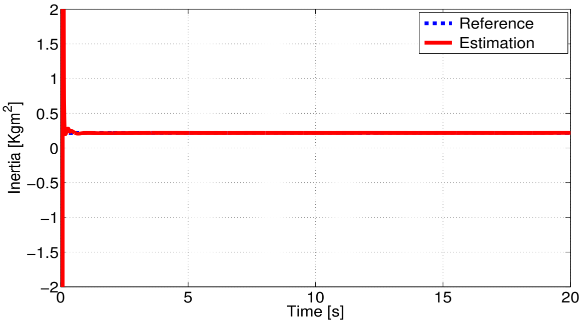

(c) Inertia Estimation

Figure 3.5: Simulation result. Mean values of relative errors: 5.1% for the link stiffness, 6.7% for link damping and 9.8% for link inertia.

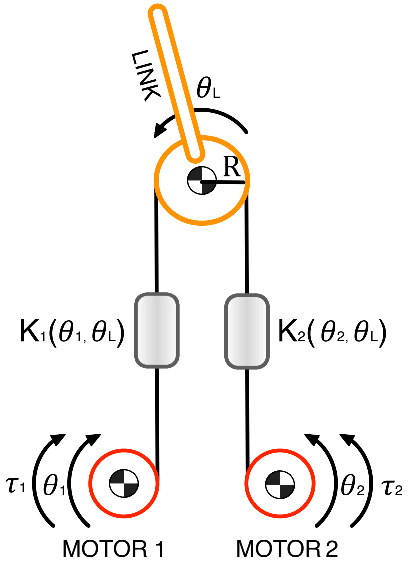

Figure 3.6: Schematic of agonist antagonist (AA) model.

$$\begin{cases} J_L\ddot{\theta}_L + S_L\dot{\theta}_L + K_1(\theta_L, \theta_1) + K_2(\theta_L, \theta_2) = \tau_{ext} \\ J_1\ddot{\theta}_1 + S_1\dot{\theta}_1 - K_1(\theta_L, \theta_1) = \tau_1 \\ J_2\ddot{\theta}_1 + S_2\dot{\theta}_2 - K_2(\theta_L, \theta_2) = \tau_2 \end{cases}, \tag{3.36}$$

where in the first equation J_L is the link inertia, S_L is the link damping, θ_L, $\dot{\theta}_L$ and $\ddot{\theta}_L$ is the link angular displacement, angular velocity and angular acceleration, respectively.

In the second equation J_1 is the inertia of the Motor 1, S_1 is the damping of the Motor 1, θ_1, $\dot{\theta}_1$ and $\ddot{\theta}_1$ is the Motor 1 angular displacement, angular velocity and angular acceleration, respectively.

Finally, in the third equation J_2 is the inertia of the Motor 2, S_2 is the damping of the Motor 2, θ_2, $\dot{\theta}_2$ and $\ddot{\theta}_2$ is the Motor 2 angular displacement, angular velocity and angular acceleration, respectively.

$K_1(\cdot)$ and $K_2(\cdot)$ are the elastic torques produced by two non linear cubical spring and described by the following equations

$$\begin{aligned} K_1 &= K(\theta_L - \theta_1)^3 \\ K_2 &= K(\theta_L - \theta_2)^3, \end{aligned} \tag{3.37}$$

where K is the elastic constant of the cubical springs.

For this set of simulation I considered Motor 1 and Motor 2 (see also fig. 3.6) with the same physical parameters, hence with $J_1 = J_2$ and $S_1 = S_2$.

Results of simulations are shown in Fig. 3.7. The simulated experiment consisted in feeding the two motors of the Agonist–Antagonist actuator with two sinusoidal torque signals added with a saw tooth torques. Parameters of the two observers are tuned as follows:

$$\begin{aligned} Q &= I_{4\times4} \\ R &= 10^4 \times I_{2\times2} \end{aligned} \tag{3.38}$$

with initial guesses

$$x_{0|0} = \begin{bmatrix} 0 & 0 & 0 & 0 \end{bmatrix}^T \tag{3.39}$$

$$P_{0|0} = 1000 \times I_{4\times4}, \tag{3.40}$$

while the stiffness observer gain (3.16) is set to

$$\alpha = 1000. \tag{3.41}$$

Agonist–Antagonist model parameters are reported in table 3.1.

Remark 3.2 *J_L and S_L are purely used as reference in order to compare the results obtained with the full impedance observer.*

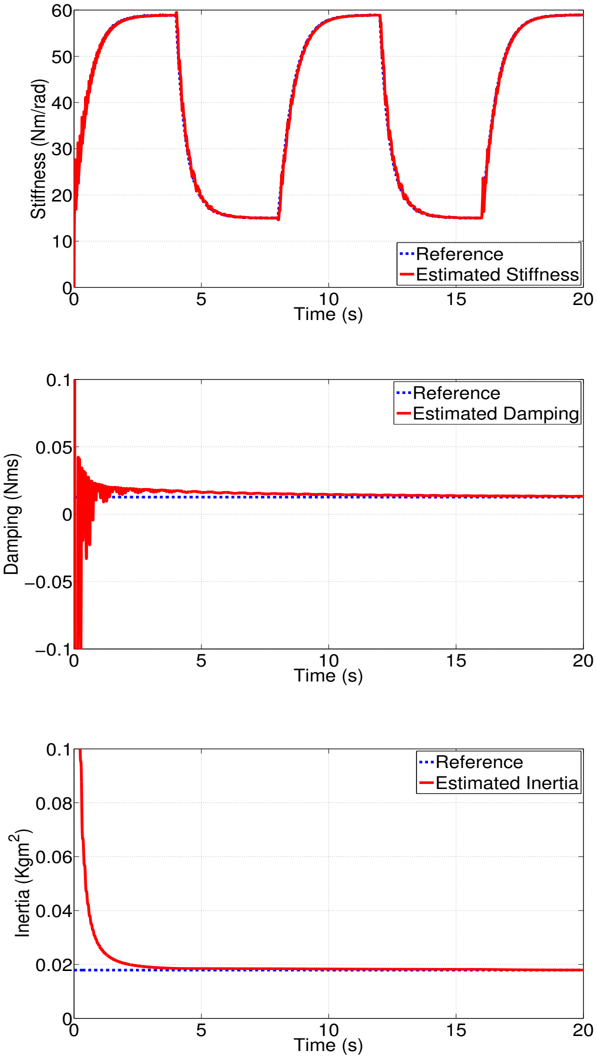

Figure 3.7: Simulation result. Mean values of relative errors: 3.2% for the link stiffness, 4.7% for link damping and 8.8% for link inertia.

Table 3.1: Agonist–Antagonist model parameters

Parameter	Value	Dimension
J_L	0.0179	Kgm^2
$J_1 = J_2$	10^{-4}	Kgm^2
S_L	0.0127	Nms
$S_1 = S_2$	0.0127	Nms
K	10	F/m^3

3.5.3 Experiment with ESV Prototype

The setup of the AwAS system, employed for the execution of the experimental trials, is shown in Fig. 3.4. The AwAS unit consists of two actuators. The main joint actuator (Link Motor) is based on a combination of an Emoteq HT-2300 frameless brushless motor (capable of a peak torque of 2.3 Nm) and a harmonic reduction drive CSD 20 (reduction ratio of $N = 50$ and peak rated torque of 80Nm). The stiffness adjusting actuator (Stiffness Motor) is realized by a DC motor from Faulhaber (peak torque of 0.8 Nm) combined with a ball screw reduction drive which converts the rotary motion of this motor into a linear displacement, allowing to change the effective lever arm and efficiently tune the joint stiffness. More details on the mechanical implementation of the AwAS unit can be found in [64]. The sensing system of AwAS includes four position sensors and one torque sensor; one optical encoder measures the position of the link motor, two absolute magnetic encoders measure position of the joint before (at the harmonic drive output) and after the compliance module (link position) while an incremental encoder monitors the position of stiffness motor and subsequently the displacement of the linear drive. A torque sensor is located between the harmonic drive and the intermediate link and senses the torque applied by the link motor. The general specifications of AwAS are presented in Table 3.2. The unit controller and power driver used to control the AwAS unit are custom control boards based on the Motorola DSP 56F8000 chip with CAN communication interface.

Table 3.2: General specification of AwAS

Range of Motion(deg)	-120÷120
Range of Stiffness (N m/rad)	30÷130
Peak Output Torque (N)	80
Length (m)	0.27
Width (m)	0.13
Total Weight (Kg)	1.8

The experiment consisted in feeding the two motors of the AwAS actuator with two sinusoidal torque signals. Parameters of the two observers are tuned as follows:

$$Q = 0.00001 \times I_{4\times4}$$
$$R = 0.000001 \times I_{2\times2},$$

with initial guesses

$$\begin{aligned} x_{0|0} &= \begin{bmatrix} 0 & 0 & 0 & 0 \end{bmatrix}^T \\ P_{0|0} &= 100 \times I_{4\times4}, \end{aligned}$$

while the stiffness observer gain (3.16) is set to $\alpha = 8$.

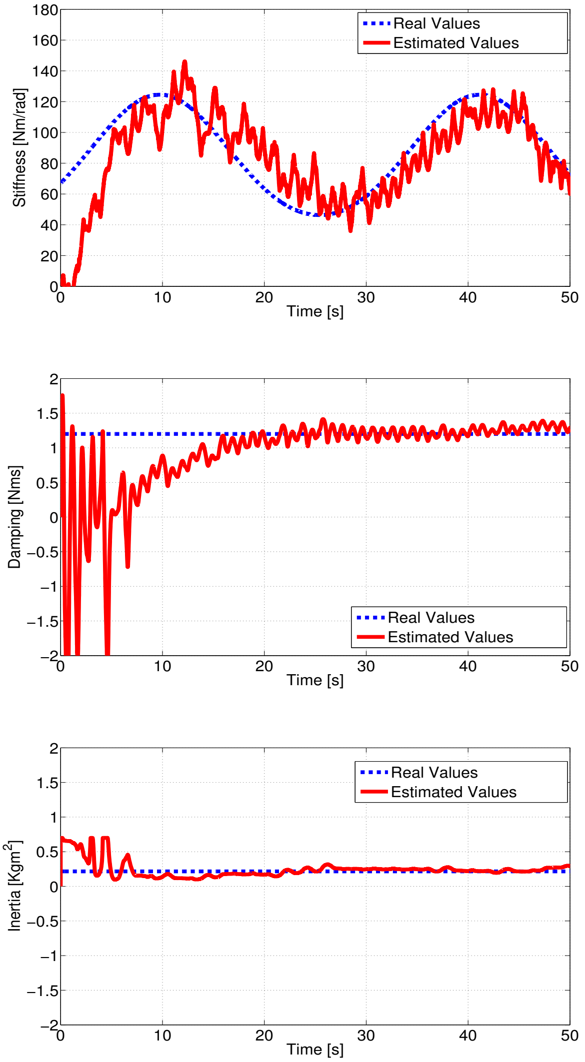

Figure 3.8: Experiment result. Mean values of relative errors: 38.2% for the link stiffness, 9.4% for link damping and 12.2% for link inertia.

3.5.4 Tuning

The observer was calibrated by trial and error as following.

1. Extended Kalman Filter: starting from Q, R e $P_{0|0}$ matrices equal to the identity, diagonal elements related to badly converging variables are tuned. In particular, elements of Q are related to oscillation of the variables, elements of R to the convergence speed. $P_{0|0}$, influences the update speed on the initial moments in which EKF starts.
2. Stiffness observer: the only parameter to calibrate is the observer gain α, it is obtained by optimizing the trade-off between the effects of the measurement noise on one side, and speed of convergence of the estimate on the other.

Part III

Haptic and Haptic Devices

This part presents two haptic devices, the Fabric Yielding Display (FYD) and the Fabric Yielding Display–2 (FYD–2) (introduced in chapter 4 and 5, respectively). This devices are based on a bi-elastic fabric and allow to mimic different stiffness and force-area curves. Stiffness and force-area curves have a crucial importance in the haptic exploration. The devices proposed was tested with phycophisical experiments on humans in order to quantify the effective performance in reproducing haptic informations an cues.

In the last chapter (chapter 6) of this part I introduce a custom made 36 axis F/T (Force/Torque) sensor employed in experiments on the characterization of human grasp. Three different calibration method are presented for this sensor. On this custom made sensor can be fixed different shape in order to assembly different sensorized obgect to grasp. Moreover, I introduce an algorithm to detect the contact point of an object interacting with a generic F/T where a know surface is fixed. Calibration results and contact point section results are reported to show the effective performances of the sensorized object proposed.

Chapter 4

Fabric Yielding Display

In this chapter I propose a new haptic device which convey to subjects both cutaneous and kinaesthetic information by exploiting the bi-elasticity of a fabric and, at the same time, give a direct measurement of the contact area involved in the interaction between the fingertip and these devices.

The role of the exploration of both real and virtual textiles and fabrics is becoming an important topics in haptic research ([65], [66], [67], [68], [69]). My starting point is the hypothesis that softness discrimination by touch is given by the rate at which the contact area between manipulated objects and fingertip grows over time, as the finger is increasingly pressed on the object. This relationship, already cited and described in [34], is referred to as Contact Area Spread Rate (CASR). In [34], authors proposed a CASR display able to replicate the spread rate of contact area between probed material and fingertip. The main limitation of the CASR display presented in [34] was the low resolution of the rendered contact area. Further work [70] aimed at integrating the CASR with a commercial Delta Haptic Device [W13] in order to increase performance.

The new haptic display here presented allow subjects to interact with a deformable surface at different levels of softness. In this case,

Figure 4.1: The system FYD: starting from the left side, it is possible to see the electronic box, which contains the motor driver and the DAQ card, the FYD prototype and a computer to control the system.

haptic perception resolution is higher and discrimination capabilities are enhanced.

First I discuss the design, architecture and implementation of the FYD. Then, I focus on the control mechanisms of this display based on contact area estimation. I also describe the graphical user interface, which is friendly and intuitive.

Finally, I evaluate performance of the display through a set of psychophysical tests, and compare softness discrimination capabilities with the CASR display [34].

Further details about this topic can be found also in [A6], [A7] and [A8]

4.1 FYD: Structure Description

The system here proposed, called hereafter FYD (Fabric Yielding Display) is based on a layer of bi-elastic fabric which can be touched by subjects with their forefinger. By changing the elasticity of the fabric,

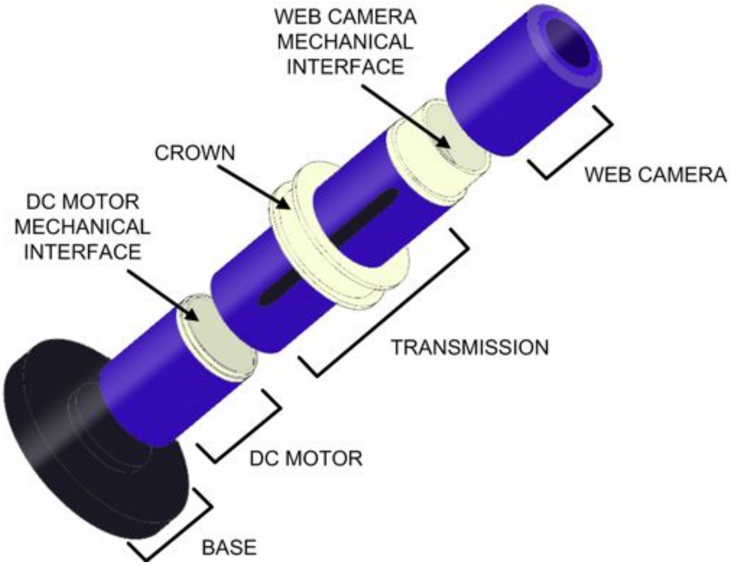

Figure 4.2: External view of the prototype. The potentiometric sensor connected to the crown is not reported for a better visualization.

subjects are able to feel different levels of stiffness. It is comprised of a hollow plastic cylinder containing a DC motor. A thin layer of bi-elastic square shaped fabric (250 × 250 mm) is placed on the top of the hollow cylinder and it is tied to a circular crown which can run outside along the cylinder, with a minimum friction. When the motor pulls down the crown, the fabric is stretched and its apparent stiffness increases. Conversely, when the motor pushes down the crown, the fabric is relaxed and it is felt softer. The FYD also behaves like a contact area display, by suitably processing signals coming from a couple of photo-devices. A view of the display is reported in fig. 4.1. The FYD prototype is 300 mm high and 60 mm wide in diameter and consists of three sections (see fig. 4.2 and fig. 4.3):

1. Motor section (80 mm high). The motor is controlled using a Sabertooth Syren10 [W14] dual motor driver. This driver allows to get a bidirectional rotation of the motor. Using the National

DAQ system PCI6036E [W15], I can acquire the position of the crown with an external potentiometer connected to it, and, consequently, apply the input voltage to the motor in order to reach the desired position, i.e. the desired stretching state of the fabric (see section 4.1.1);

2. Transmission section (160 mm high). The transmission system converts the rotational movement of the motor into the translational movement of the crown. The system consists of a screw-female screw, the latter is attached to the crown by means of three, 120° spaced, metallic supports. They are moved with the crown. The DC motor is connected to the screw with an Oldham joint. The screw-female screw system was adopted in order to have an acceptable trade off between the velocity of the crown and the torque necessary to reach a good state of stretching of the fabric. In addition, the screw-female screw system allows a bidirectional movement of the crown;

3. Web camera section (60 mm high). The camera (whose resolution is 320×240 pixels) is placed inside the hollow cylinder at the center of the mechanical interface, just beneath the fabric. The camera is endowed with high luminosity LEDs and frames the lower surface of the fabric. During the tactual indentation, the fabric is strained and the fabric area which comes into contact with the fingertip changes according to the applied force. The camera allows to acquire the image of the strained fabric and, by means of suitable processing algorithms, the contact area can be estimated (see section 4.1.2).

The prototype as a whole is connected on a base (15 mm high and 90 mm diameter) in order to guarantee the physical stability.

Several materials (including commercial lycra, latex layer, and silicon rubber) were tested to verify their suitability for my purpose. Best performance were provided by Superbiflex HN by Mectex [W16]

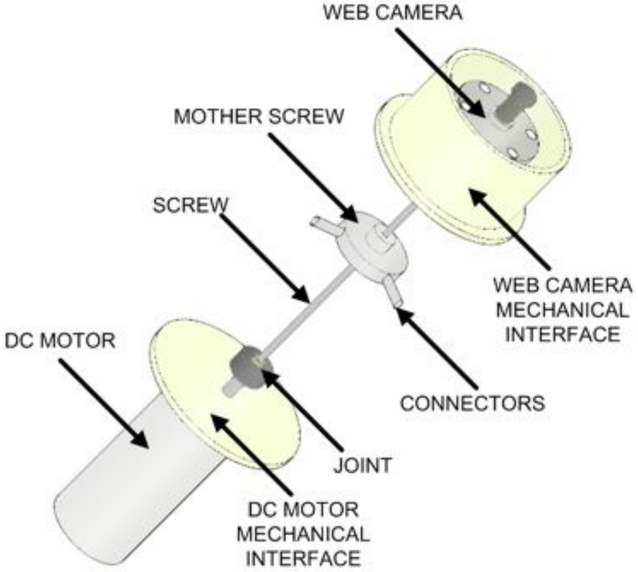

Figure 4.3: Prototype internal view. It is possible to see the transmission system and the DC motor position.

because it exhibits both a very good elastic behaviour with a large range of elasticity and a high resistance to traction.

4.1.1 Control

Control strategy was implemented in order to have a low computational workload and guarantee a real-time functioning.

Control is based on two signals comparison (see fig. 4.4), P_{ref} e P_r that are, respectively, the reference position and the current position of the crown read by the potentiometer.

The comparison produces a third signal (`s`) for the motor driver activation. In pseudo-code the situation is represented as

```
if($P_{ref}$==$P_r$){s=0}
if($P_{ref}$>$P_r$){s=+1}
if($P_{ref}$<$P_r$){s=-1}
```

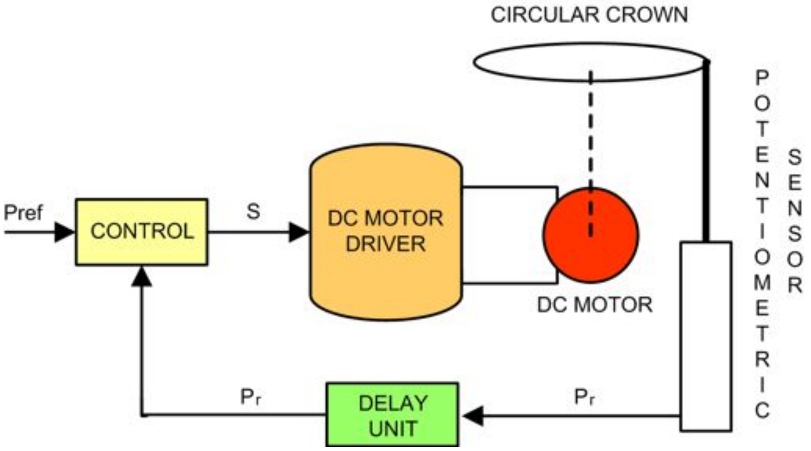

Figure 4.4: Control blocks architecture: P_r is the signal acquired by the potentiometric sensor, S is the signal produced by the comparison of P_{ref} and P_r.

The signal `s` has three logical levels. When $\mathtt{s} = -1$ the motor is driven to clockwise rotate, while when ($\mathtt{s} = +1$) the motor rotates counterclockwise. When $\mathtt{s} = 0$, the DC motor is stopped at the current position. P_{ref} is the position of the circular crown, to which a specific level of stretching of the fabric is associated. It is calculated from the characterization curves (see section 4.1.3). P_r is the signal recorded by the potentiometric sensor and gives the current position of the crown. At each simulation step, the control produces the signal `s` and the DC motor is moved until the actual crown position is equal to P_{ref}. In fig. 4.4 the control block diagram is reported, where the delay unit is put to prevent algebraic loop when the control starts to run.

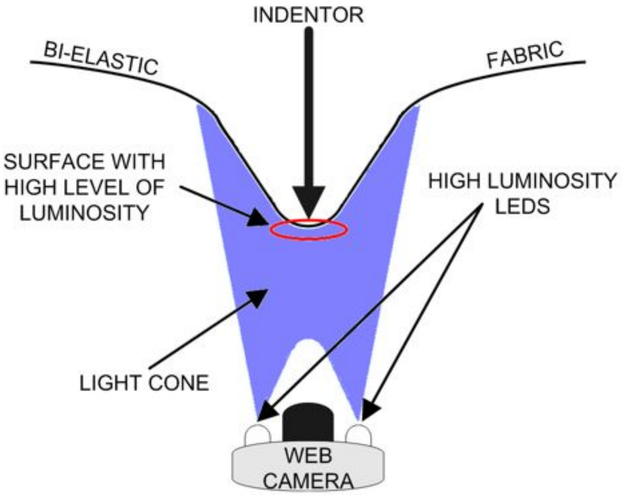

Figure 4.5: Scheme of the area acquisition and the illumination system.

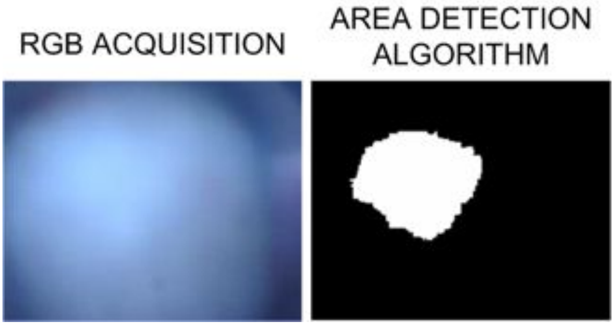

Figure 4.6: The results of the contact area detection algorithm: the RGB acquisition (on the left side) and the result of the final binarization (on the right side).

4.1.2 Area Acquisition

The FYD system allows to visually display the contact area between the fabric and the fingertip. A suitable segmentation algorithm gives an estimation of the contact area which is real-time visualized.

The contact area acquisition algorithm is based on the RGB image binarization. More properly, only one image band (the R band, which is 320×240 matrix of integer numbers) out of three is involved in the area detection algorithm to avoid a computational workload too high for assuring a real-time processing.

During the tactile probing, the indented fabric surface is closer to the camera with respect to the outer region. Consequently, this area will be more lighted up by the LEDs. The difference between background luminosity and contact area luminosity is discriminated by binarization thresholds (see fig. 4.5), which were heuristically calculated. Using a linear interpolation, at each vertical position of the crown a binarization threshold was associated. In this manner, the pixels in the image which belong to the contact area are displayed as white pixels.
The contact area in $[cm^2]$ is estimated as

$$C_{area} = N_p \times \frac{A_c}{S_p}, \tag{4.1}$$

where N_p is the number of white pixels belonging to the contact area; A_c is the frame area in $[cm^2]$ and S_p is the web camera resolution (i.e. 320×240 pixels). The accuracy of the contact area measurement is crucial because the indentation force and the indentation displacement are indirectly estimated using, respectively, Force–Area and Force–Displacement characteristics. The result of the area detection algorithm is reported in fig. 4.6.

4.1.3 Characterization and Interpolation

In this work I disregard the contact mechanism in all its details, both from mechanical and physiological viewpoint [71], but I use a simplified model, as already proposed in [34].

As it is well known, haptic perception is given by the combination of two different modalities, kinaesthetic and cutaneous. When a hap-

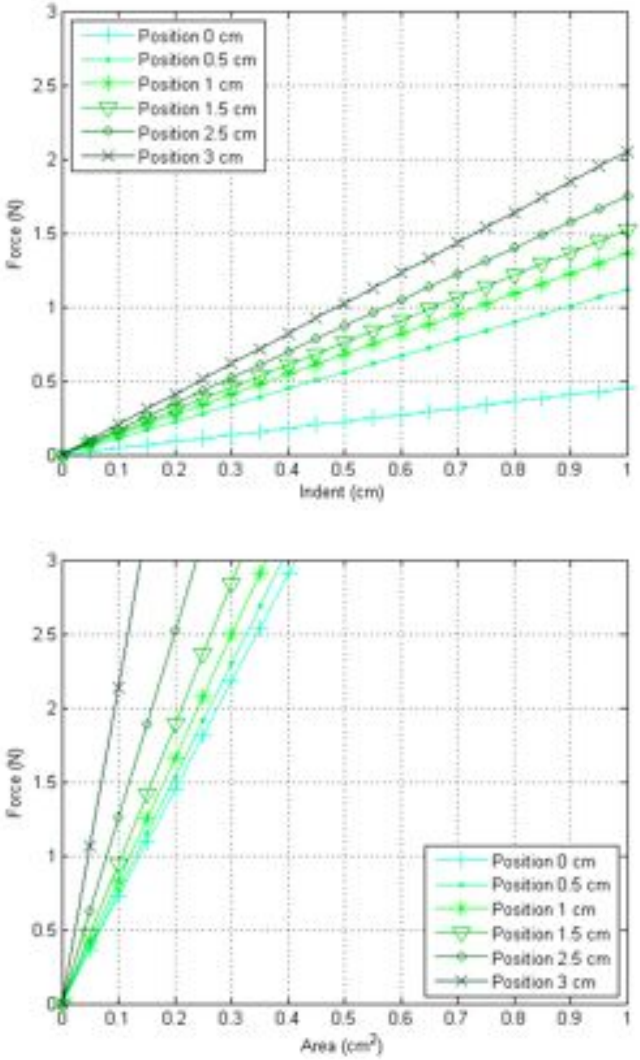

Figure 4.7: Characterizations of Force–Displacement (upper figure) and of Force–Area , obtained using a 5 mm step for the vertical crown displacement.

tic device is designed and realized both these perceptual cues have to be provided. In literature, there are several way to convey these types of information. Here I use a simplified abstraction of these features.

Let the resultant contact force be denoted by F, the contact area by A. Let also δ denote the overall (rigid) relative displacement between the two bodies.

The $F(\delta)$ curve of a fingertip/object pair can be considered as a close correlate of kinaesthetic information elicited by probing for softness.

Analogously, starting from the CASR hypothesis ([34]), I will therefore consider the $F(A)$ curve of a fingertip/object pair as a correlate of cutaneous information elicited by probing for softness.

The device here proposed is controlled in order to simulate softness of materials having specific $F(\delta)$ and $F(A)$ curves.

The current architecture of FYD, at least in this preliminary prototype, does not allow decoupling cutaneous and kinaesthetic information, because they are both intrinsically constrained to the elasticity of the fabric.

In Fig. 4.7 the $F(\delta)$ and $F(A)$ curves of the fabric at different levels of stretching are reported.

These levels were obtained changing the position of the crown, in a range between 0 mm (0 mm was chosen near the top of the cylinder) and 30 mm, with an incremental step of 5 mm.

I used a load-cell to measure the force applied on the fabric during the indentation. Indentation tests were performed by means of a compressional indentor driven by an electromagnetic actuator.

The actuator is a Bruel & Kjear minishaker, capable of applying a maximum displacement of 10 mm in the axial direction. The indentor is a wood model of the human fingertip of 15 mm in diameter and 100 mm in length.

This is a first approximation of the fingertip. Differences between the wood indentor (which is a non-compliant object) and the human fingertip (which is a compliant object) had to be considered. However the deformations of the fingertip interacting with the fabric, which

which is naturalistically modeled under the fingertip, are very small and the approximation with a non-deformable object is acceptable.

The indentor is equipped with a magnetic linear transducer, Vit KD 2300/6C by KAMAN Science Corporation, in order to measure the vertical displacement induced on the fabric, and with a load cell sensor, ELH-TC15/100 by Entran, able to detect forces up to ±50 N. In this way I obtained a real-time measurement of the Force–Displacement ($F(\delta)$) characteristics for every position of the crown.

At the same time, it was possible to acquire the image of the strained fabric, by means of the camera endowed with high luminosity LEDs, placed just beneath the fabric (at a distance of 30 mm). Upon suitable processing algorithms, an estimation of the contact area under the indenting force was given. In this way, I obtained a real-time measurement of Force–Area ($F(A)$) characteristics.

During the characterization phase, only a finite set of positions was acquired. For intermediate values I used linear interpolation.

When I would like to mimic a given material having a specific stiffness coefficient I have to identify which position of the crown provides the fabric elasticity whose Force-Displacement approximates that of the material. $F(A)$ and $F(\delta)$ curves (see fig. 4.7) are linear over all the positions of the crown.

4.1.4 Graphical User Interface

A GUI (Graphical User Interface) was implemented in MATLAB © ([W17]) to allow a correct utilization of the display. The GUI presents a hierarchical structure and consists of four windows: two for the initialization of the prototype and two for the contact area, force and indentation measurement (see fig.4.8).

The “Home” window has the main role of managing all the simulation levels. In fact, from the "Home", each level of the GUI can be reached using an easy drop-down menu. The “Initialization” window permits to insert a stiffness coefficient for the simulation of a particular material. This stiffness coefficient corresponds to an angular

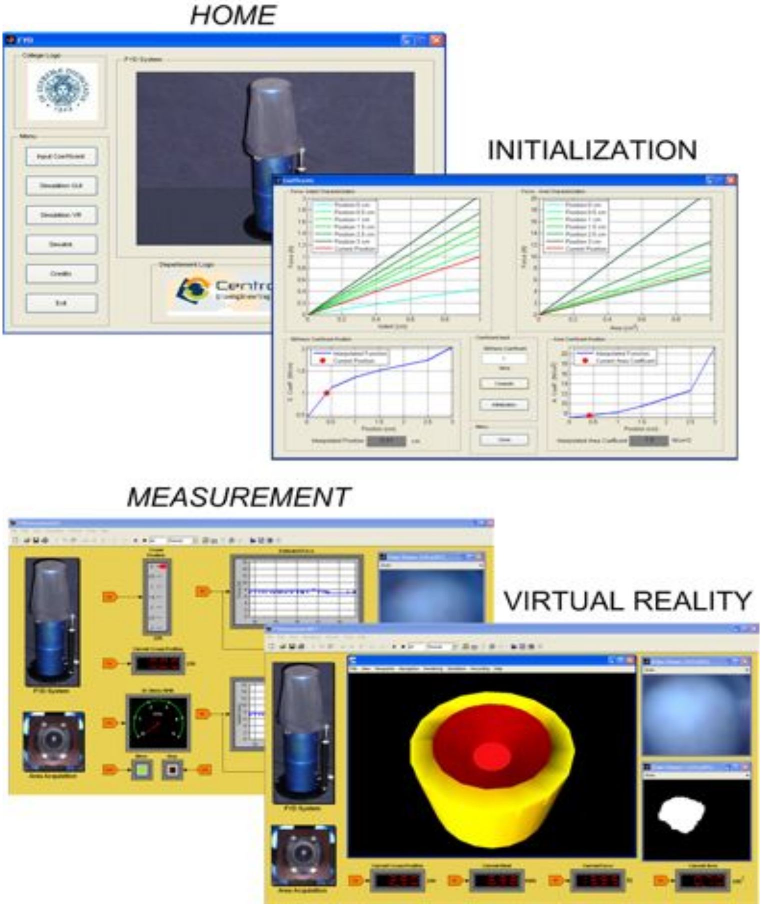

Figure 4.8: GUI implemented: HOME and INITIALIZATION windows for the initialization of the prototype; MEASUREMENT and VIRTUAL REALTY windows to display the measurement of force, area and indentation

coefficient of an unknown $F(\delta)$ characteristic, which can be obtained interpolating the characterization curves. At the same time, the angular coefficient describing the related $F(A)$ characteristic is calculated. Properly, in the "Initialization" window, the stiffness coefficient was compared to the Force–Indentation and Force–Area curves (which are not independent) and the corresponding vertical crown position was determined (P_{ref}, see section 4.1.1). The “Measurement” window offers a complete environment for the real time measurements of the principal contact parameters (e.g. contact area, force, and indentation), with the possibility of visualizing both the result of the area detection algorithm and the RGB acquisition of the indented fabric. The "Measurement" allows also a control of the correct functionality of the display, in terms of motor performance monitoring. In the “Virtual Reality” window a simple virtual reality application was realized to geometrically describe both the contact area and the exerted indentation indirectly estimated from it (see section 4.1.4.1).

4.1.4.1 Virtual Reality Implementation

The Virtual Reality was also implemented in MATLAB ©. To describe the geometry of the indentation, two hypothesis were assumed:

a. Contact area shape: I assumed that the contact area shape was a perfect circle with radius of $\sqrt{C_{area} \setminus \pi}$ (C_{area} was previously calculated using the area detection algorithm);

b. Indentation: I assumed that the axis of the indentation was the vertical axis of FYD.

Starting from assumptions (a) and (b), the indented surface was approximated using a set of troncated right cones nested together. They present the same area of the larger base (which is equal to the upper base of FYD), while the surface of the smaller base correspond to the contact area and it changes according to the value of indentation. At each value of indentation was associated a troncated cone, i.e. each value of indentation describes the height of a troncated cone. In this way, only the internal lateral surface of the troncated cone is useful for a correct visualization in a virtual environment and so visible in the virtual reality, while the rest of the cone is not displayed, even if drawn. To completely describe the lateral surface, the only

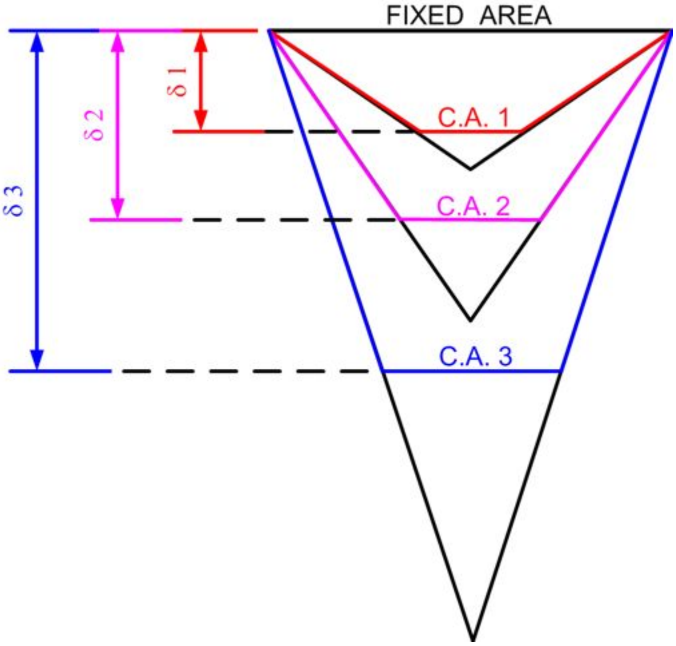

Figure 4.9: The set of troncated cones associated to different levels of indentation . The term “C.A.” refers to the contact area. The term δ refers to the indentation

parameter to determine is the total height of the cone, h. Referring to fig.4.10, using simple geometric valuations, it is possible to write

$$\overline{AB} = R$$

$$\overline{BK} = \overline{OJ} = r^* \tag{4.2}$$

$$\overline{AK} = \overline{AB} - \overline{BK} = R - r^*,$$

with R and r^*, respectively, the radius of the larger base and the radius of the smaller base (known from assumption (a)). Moreover

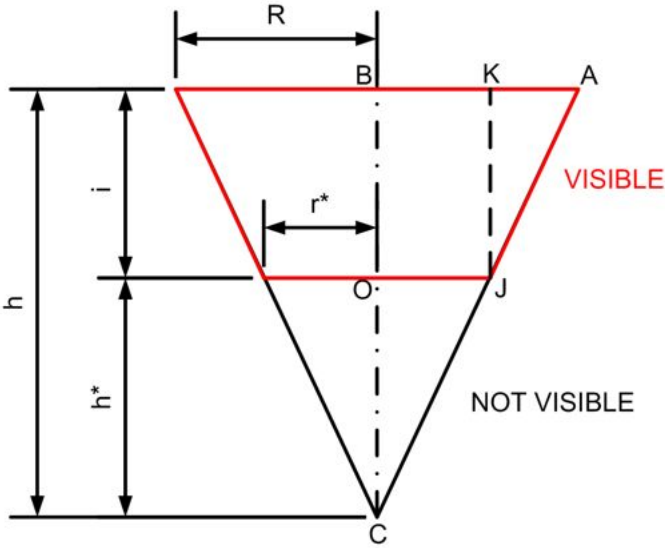

Figure 4.10: Cross section of a cone and some geometric parameters.

$$\begin{gathered}\overline{BO} = \overline{KJ} = i \\ \overline{OC} = h^* = \overline{BC} - \overline{BO} = h - i,\end{gathered} \tag{4.3}$$

with i and h, respectively, the indentation (indirectly estimated) and the cone height (unknown). Exploiting the similarity of $\widehat{KAJ}$ e $\widehat{OCJ}$ triangles, it is possible to write

$$\overline{OC} = \frac{\overline{OJ} \cdot \overline{KJ}}{\overline{KA}} = \frac{r^* i}{R - r^*}. \tag{4.4}$$

Considering that cone height h is given by

$$\overline{BC} = \overline{BO} + \overline{OC}, \tag{4.5}$$

finally, h is calculated as

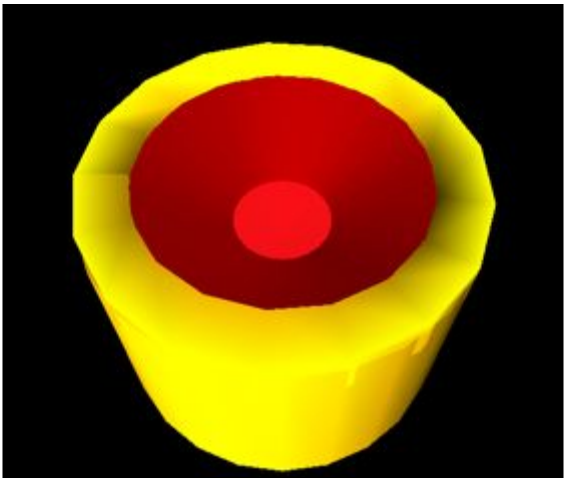

Figure 4.11: Final representation of the geometry of the indentation in the virtual reality.

$$h = i + \frac{r^* i}{R - r^*} = \frac{Ri}{R - r^*}. \tag{4.6}$$

These considerations were the background for the correct drawing of the geometry of the indentation in the virtual environment, reported in fig. 4.11.

4.2 Psychophysical Experiments

The experimental session was designed to evaluate the performance of the FYD, comparatively with a CASR device. The performance of the FYD was assessed both with the integration of the virtual reality rendering and without it, in order to valuate if the system improves when visual stimuli are provided. I have chosen the CASR display realized by the same authors as comparative device because it is based on the same paradigm as the FYD. Specific technical details of this CASR display can be found in [34]. Here I briefly summarize how it

Figure 4.12: The discrete CASR display.

works. The CASR device is a pneumatic device consisting of a set of cylinders of different radius, assembled in telescopic arrangement (see fig.4.12). Because of the discontinuity in the structure due to the cylinders, I will refer to this CASR display as discrete CASR display.

A regulated air pressure is inflated inside acting on the cylinders according to the desired force to be perceived by subjects during indentation. Pressure is applied on all the cylinders. When the subject finger pushes down against the cylinders, it comes into contact with a surface depending on the height of the cylinders themselves and perceives a resultant force correlated to the pressure. The display can realize a desired force-contact area (CASR) relationship [34]. Even for the discrete CASR display, the force-area behaviour is strictly related to the geometry of the device, therefore it cannot be independently controlled from the force-displacement behaviour.

I selected five simulated specimens, i.e. five Force-Displacement and Force-Area characteristics, which can be exactly rendered both with FYD and the discrete CASR display. In the table 4.1 the input parameters of FYD and of the discrete CASR device to reproduce the five simulated specimens are reported.

Results in rendering softness with the discrete CASR display were already rather satisfactory [34]. My aim was to improve these results using FYD.

4.2.1 Subjects

After written consensus, 15 healthy volunteers participated in the study. Their age ranged from 23 to 40. None had a history of nerve injury or finger trauma and their finger pads were free of calluses. 5 volunteers participated only in the experiments with the discrete CASR display; 5 volunteers participated only in the experiments with the FYD display (with and without the virtual reality integration); 5 volunteers participated in all the experiments. In conclusion, each type of experiment was performed by 10 subjects. Their handedness was evaluated by the Edinburgh Handedness Inventory (EHI) [72] and they were allowed to use the dominant hand to perform the task. They always performed the tests comfortably sat, blindfolded (except for the tests performed with the integration of the virtual reality rendering, in which subjects were requested to look at a monitor visualizing the rendered tactile experience in the virtual environment) and with plugged up ears, to prevent the possible use of any other sensory cues and eliminate any diversion from the task. The chosen arm was locked to the table and the subject was able to move the wrist and fingers only.

4.2.2 Rendered Specimens

Artificial softness specimens were used through the experimental session, rendering five different $Force-Displacement$ and $Force-Area$ curves, see fig. 4.7. I will refer to these specimens as $SS1$, $SS2$, $SS3$, $SS4$ and $SS5$, see tab. 4.1. The specimens were chosen in order to be rendered in the same way with the two displays, i.e. these specimens exhibit the same $Force - Displacement$ and $Force - Area$ curves both with the discrete CASR and with FYD.

Stiffness	Coeff. (N/cm)	Pressure (bar)	Position (cm)
SS1	0.67	0.35	0.16
SS2	1.00	0.5	0.41
SS3	1.18	0.6	0.86
SS4	1.28	0.7	1.44
SS5	1.71	0.8	2.33

Table 4.1: Discrete CASR display (third column) and FYD (fourth column) parameters. The term “Position” refers to the vertical position of the crown of the FYD (position 0 was chosen near the top of the cylinder) associated to a given stiffness coefficient. The term “Pressure” refers to the pressure of the air inflated into the internal camera of the discrete CASR display to mimic a given stiffness coefficient. At each value of “Position” of FYD corresponds a value of “Pressure” of discrete CASR device, in order to render the same specimens. The characteristic $Force - Area$ is strictly related to the P-δ curve, i.e. the stiffness coefficient

4.2.3 Experiments: Design and Procedure

Subjects participating in these experiments were presented with rendered specimens and were asked to judge their softness by touch. They were instructed to do so by pressing vertically or tapping the index finger of their dominant hand against the displays. Subjects were recommended not to perform movements of the finger across the surface and not to apply lateral forces. In this way, according to the literature [36], any anisotropic effect or distortion in softness perception due to the radial/tangential discrepancy in touch is eliminated, only focusing on normal indentation of the specimens. Experiments were designed to test the ability of subjects to tactually discriminate softness both through the discrete CASR display and through the FYD, with and without the integration of the virtual reality feedback. The aim is to compare the performance in rendering specimens between these two displays. The experiments included pairwise discrimination and ranking tasks. In all tests, subjects had no time limitations and were allowed to check each specimen or haptic stimulus as many times as they wished going back and forth between them at will. The design of the experiments, in evaluating ranking and pairwise discrimination performance, is similar to the approach reported by Srinivasan and LaMotte [32], even if a direct quantitative comparison of these results with those of Srinivan and LaMotte is not in order. The aim of the experiments was not to obtain a statistically significant validation (e.g ANOVA, [73]) of the performance of FYD compared with the CASR display or define perception thresholds for the displays, like JND (Just Noticeable Difference) or Weber fractions ([74], [75]). On the contrary results of the tests were only presented avoiding any strong consideration above their significance. This methodology in data analysis referred to the work ([76]) which has to appear in Transactions on Haptics.

4.2.3.1 Pairwise discrimination

In each trial, a standard ($SS3$) and a comparison specimen were presented to the subjects in random order. After probing the specimens, subjects were asked to report which of the two was softer. Each task was performed three times for each subject.

4.2.3.2 Ranking

In the ranking experiment subjects were asked to probe and sort in terms of softness the set of 5 specimens $SS1$ to $SS5$, presented in random order. Ranking tasks were repeated three times for each subject.

4.3 Experimental Results and Discussion

4.3.1 Pairwise Discrimination

Results of pairwise discrimination experiments, for both the displays, are reported in fig. 4.13. Answers are classified as $X = 1$ if the subject correctly identifies the softer specimen, or $X = 0$ otherwise. The average number of correct answers m_n is represented by the height of the histogram bars in fig. 4.13. The statistics of this binary experiment are described by its Bernoulli distribution. Confidence intervals for expected values $E(X)$ with statistical significance $(1 - \alpha)$ are also reported in fig. 4.13. The intervals are computed as

$$E(X) \in \left[m_n - z_{\alpha/2}\sqrt{\frac{m_n(1-m_n)}{N}}, m_n + z_{\alpha/2}\sqrt{\frac{m_n(1-m_n)}{N}} \right], \tag{4.7}$$

with $\alpha = 5\%$, sample size $N = 36$, and critical value of the normalized standard distribution $z_{\alpha/2} = 1.96$ (from standard statistical tables). It is worthwhile noting that for both the displays the normalized correct answers are very similar and comparable, for stimuli that are farther away from the reference, in the range of stiffness (i.e., $SS1 - SS3$ and $SS5 - SS3$). For closer pairs ($SS2 - SS3$ and especially $SS4 - SS3$), artificial specimens rendered with the CASR display are discriminated in a poorer way than their counterparts rendered with FYD without the virtual reality feedback. When subjects are provided with visual cues given by the contact area rendering in the virtual environment, performance globally increases, even if not dramatically.

4.3.2 Ranking

Results from ranking experiments are shown in tables 4.2 ,4.3 and 4.4, where subjective softness is reported versus objective compliance in a confusion matrix structure for the five specimens, under the three

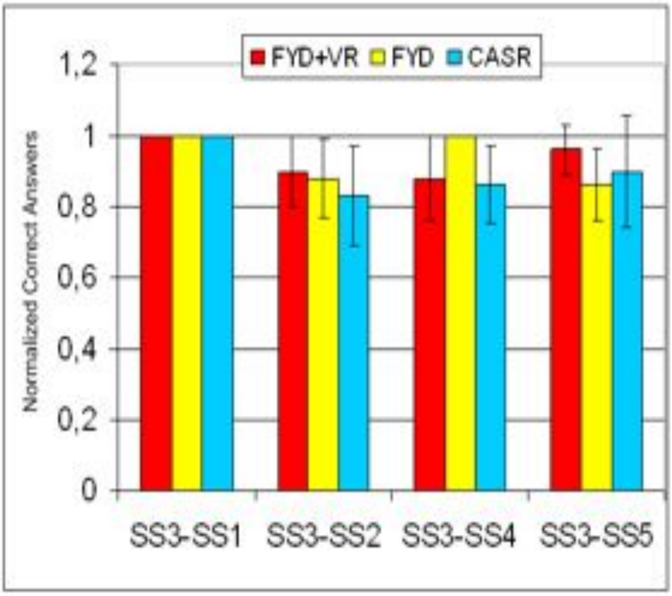

Figure 4.13: Results of pairwise test with CASR and FYD, with and without the virtual reality feedback.

different conditions. Values on the diagonal express the amount of correct answers. The percentage of total accuracy is calculated considering the sum of all correct answers. The results obtained with the discrete CASR display exhibits a percentage of total accuracy of 61%. The results obtained with FYD, without virtual feedback, exhibits a percentage of total accuracy of 82%. When subjects were allowed to exploit the virtual reality rendering, a total accuracy of 84% is observed. In addition, the dispersion of the matrix is reduced and the matrix appears as tridiagonal. It means that errors are limited to pairs that are very close in the stiffness range.

	SS1	**SS2**	**SS3**	**SS4**	**SS5**	$N°$	**Relative A.**
SS1	18	4	1	1	6	30	60%
SS2	0	19	8	3	0	30	63%
SS3	2	1	18	8	1	30	60%
SS4	8	1	1	17	3	30	56%
SS5	2	5	2	1	20	30	66%
							Total A.
$N°$	30	30	30	30	30	150	61%

Table 4.2: Confusion matrix of ranking experiments with the discrete CASR display. The term "Relative A." refers to the accuracy, i.e. the percentage of correct recognition, associated to a specific specimen. The term "Total A" refers to the total percentage of correct recognition, considering all the specimens.

4.3.3 Discussion

Results show that FYD appears to provide more information than the discrete CASR display, in the pairwise discrimination tests as well as in the ranking experiments. This fact fundamentally relies on the absence of edge effects during the interaction between fingertip and fabric surface. Moreover, being the fabric deformable in a controlled way under the fingertip, this new device is able to provide cues for a more reliable and realistic perception. Indeed, FYD appears to increase performance both in tasks such as ranking, which require multiple comparisons and involve haptic memory, and in tasks of pairwise discrimination between specimens which are close in stiffness, i.e. increasing "haptic" resolution.

When FYD was used with the integration of the virtual reality feedback, the best results were observes, especially in ranking experi-

	SS1	**SS2**	**SS3**	**SS4**	**SS5**	*N*°	**Relative A.**
SS1	22	4	0	2	2	30	73%
SS2	4	25	1	0	0	30	83%
SS3	0	1	27	0	2	30	90%
SS4	3	0	0	25	2	30	83%
SS5	1	0	2	3	24	30	80%
							Total A.
N°	30	30	30	30	30	150	82%

Table 4.3: Confusion matrix of ranking experiments with FYD display, without the virtual reality feedback. The term “Relative A.” refers to the accuracy, i.e. the percentage of correct recognition, associated to a specific specimen. The term “Total A." refers to the total percentage of correct recognition, considering all the specimens.

ments when “haptic” memory is integrated with “visual” memory. Visual information is related to the contact area and local deformation of the fabric, providing helpful cues in discriminating softness. This result is very encouraging and further supports the CASR paradigm.

	SS1	**SS2**	**SS3**	**SS4**	**SS5**	$N°$	**Relative A.**
SS1	24	6	0	0	0	30	80%
SS2	6	24	0	0	0	30	80%
SS3	0	0	30	0	0	30	100%
SS4	0	0	0	24	6	30	80%
SS5	0	0	0	6	24	30	80%
							Total A.
$N°$	30	30	30	30	30	150	84%

Table 4.4: Confusion matrix of ranking experiments with FYD and the virtual reality feedback. The term “Relative A.” refers to the accuracy, i.e. the percentage of correct recognition, associated to a specific specimen. The term “Total A." refers to the total percentage of correct recognition, considering all the specimens.

Chapter 5

Fabric Yielding Display 2

In this chapter I present a new version of the FYD, hereinafter referred to as FYD–2 (see also fig. 5.1).

The main advantages of the FYD–2 are the reduced dimensions, which enable integration with other devices and wearability; an actuation system based on two fast motors, which allow for real-time trajectory tracking of force-area curves and endow the system with an additional degree of freedom to vehiculate supplementary haptic cues; a more effective sensorization scheme, with a force sensor that can record the force exchanged during haptic interaction .

Moreover, In this chapter I describe the mechanical design and the mathematical model of the FYD–2. Experiments showing the reliability in real-time tracking of force-area curves demonstrate the effectiveness of the here proposed system (for more details see also [A9] and [A10]).

5.1 Mechanical Description

For FYD–2, I use a layer of isotropic elastic fabric, Superbiflex HN by Mectex S.P.A (Erba, Como, Italy). Subjects touching the fabric can experience different levels of stiffness, which are obtained by suitably

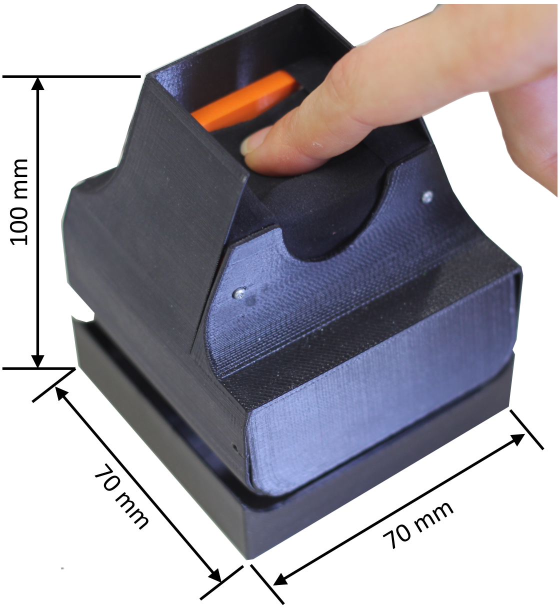

Figure 5.1: A subject's finger interacting with FYD–2. The dimensions of the device are also reported.

changing the stretching state of the fabric itself.

The extremities of a rectangular strip of the elastic fabric are connected to two rollers, each of them independently moved by a pulley placed on a motor shaft. Motors are DC Maxon Motor REmax (256:1, 3 Watt) by Maxon Motor ag, Sachseln, Switzerland. These motors provide a good trade-off between velocity and torque, thus enabling fast changes in the stretching state of the fabric.

The pulley and the roller are connected by means of a wire transmission. The motor positions are controlled with a custom made electronic board (PSoC-based electronic board with RS–485 communication protocol), which reads motor position by using two absolute magnetic encoders (12 bit magnetic encoder by Austria Microsystems - Unterpremstaetten, Austria - AS5045 with a resolution of 0.0875°).

The system exploded draw is reported in fig. 5.2. As it is notice-

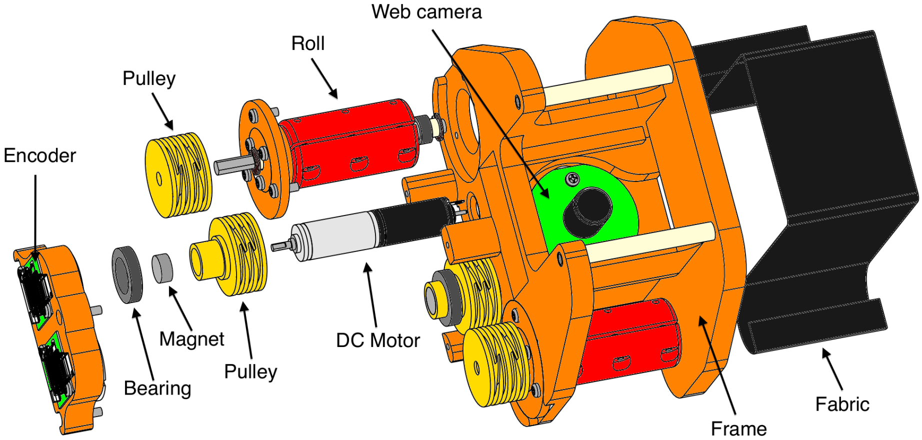

Figure 5.2: Exploded draw – in false colors – of the FYD–2. The device main components are indicated.

able from fig. 5.1, the dimensions of the FYD–2 are less than a third of the one exhibited by the previous version of the device [A8]. These reduced dimensions can enable the integration with other haptic systems (as proposed, e.g., in [76]) and wearability.

To reproduce a given level of softness, when motor 1 rotates in a counter-clockwise direction and motor 2 rotates in a clockwise direction they stretch the fabric thus increasing its apparent stiffness. On the other hand, when motor 1 rotates in a clockwise direction and motor 2 rotates in a counter-clockwise direction they relax the fabric which appears softer (for further details see fig. 5.3).

It is important to notice that the two motors, when rotate in the same direction, can implement an additional “translational” degree of freedom; such degree of freedom can be used to convey additional haptic information, such as, e.g., curvature cues. However this aspect is still under investigation.

FYD–2 also enables to real-time measure the contact area involved in the contact by placing a web camera (Kraun ”Rainbow Compact”

USB Web Camera with a resolution of 1.3 Mpixel) and two high luminosity LEDs (whose luminosity can be regulated with a trimmer) just beneath the fabric (30 mm). The segmentation algorithm used to estimate the contact area is based on binarization thresholds heuristically calculated considering the difference between background luminosity and contact area luminosity, as it is described in [A8]. An hemispherical cover is placed on the device to guarantee uniform and reproducible luminosity conditions during successive haptic interactions.

Finally, the FYD–2 is endowed with a load cell (Micro Load Cell (0-780g) - CZL616C from Phidgets, Calgary, Alberta, Canada) placed on the basis of the device to record the normal force exerted by the subject finger interacting with the fabric.

5.2 Characterization

As it is well known, haptic perception is given by the combination of two different modalities, kinaesthetic and cutaneous. As in [76], using simplified abstractions and physics concepts, I can consider the $F(\delta)$ curve resulting from the finger touching the object as an approximation of kinaesthetic information in softness perception. F $[N]$ indicates the indenting force and δ $[mm]$ the overall rigid displacement between the two bodies. Analogously, based on the CASR paradigm [34], the $F(A)$ curve can be used to describe the cutaneous cues associated with softness discrimination. The stiffness (σ in $[N/mm]$) of the fabric is computed directly deriving the contact force w.r.t. the displacement. The obtained $F(\delta)$ characteristics are quadratic (i.e $F = \lambda\delta^2$, with λ $[N/mm^2]$ be the quadratic coefficient of the parabolic curve) at fixed motor positions: the stiffness of the fabric uni-axially stretched is hence linear, since it depends on the displacement and it can be defined as (see also [77] and [78])

$$\sigma(\delta) = \frac{\partial F}{\partial \delta} = \rho\delta, \tag{5.1}$$

where $\rho = 2\lambda$ $[N/mm^2]$ is defined as the stiffness coefficient. During the characterization of the fabric, the motors were moved at different positions, considering each time the same angular displacement for both. These angular displacements are within the interval $10^\circ \div 80^\circ$, with an incremental step of 10°.

To obtain the aforementioned characteristics, I used a column load frame testing machine (Z005 by Zwick/Roell, Ulm, Germany) to compress the fabric while the indentation was recorded and the contact area was measured by the web camera placed beneath the fabric. The indentor was moved using fixed indentation steps of 1.5 mm each, for an overall displacement of 12 mm in a time interval of 30 s.

I used a wooden hemispherical indentor with a diameter of 14 mm and 100 mm in length, in order to model a finger. This diameter was chosen since it is within the typical range of human finger diameter [79]. Differences between the wooden indentor (which is a non-compliant object) and human fingertip (which is a compliant object) should be considered; however, since the deformation of the fingertip interacting with the fabric is small, the approximation of the indentor with a non-deformable object is still acceptable.

5.3 Device and Contact Area Model

Considering the characterization outcomes, I can model the system with two springs fixed at two pulleys of radius R and inertia $J_1 = J_2 = J$, whose stretching state is related to motor positions (θ_1 and θ_2, respectively) (cf. fig. 5.3). Let be K the elastic constant of the springs which model the fabric elasticity, by applying the Lagrangian formulation I get

$$\begin{cases} J_1\ddot{\theta}_1 + c_1\dot{\theta}_1 - K(R\theta_1 - R\theta_2)^2 = \tau_1 + RF\sin\alpha \\ J_2\ddot{\theta}_2 + c_2\dot{\theta}_2 + K(R\theta_1 - R\theta_2)^2 = \tau_2 + RF\sin\alpha \end{cases}, \tag{5.2}$$

where c_1 and c_2 are the damping coefficients of motor 1 and 2, respectively, τ_1 and τ_2 are the control torques and F is the indentation force

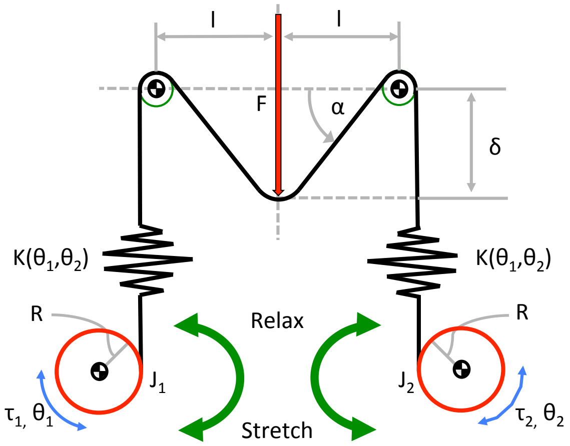

Figure 5.3: Schematic representation of the device. The elastic fabric is modeled in a symmetrical fashion with two non linear springs connected each other by means of an inextensible wire. The model springs are thought to be fixed at two pulleys of radius R and inertia $J_1 = J_2 = J$, and they stretching state changes according to the motor positions (θ_1 and θ_2). When the fingertip interacts with the fabric exerting a vertical force (F), the length of the springs as well as the geometry of the fabric are changed.

exerted by the user.

It is possible to derive also a model-based estimation of the contact area (which I assume to be expressed in $[mm^2]$). This estimate, if properly validated, might allow to have a contact area computation, without the need to measure it by the web camera. In this manner, I might use this outcome to drive the design of FYD–2 with further reduced dimensions – thus enabling device integration with complex systems or in multi-finger haptic interface.

I assume that the interaction between the finger and the device occurs at the center of the fabric and that the indentation direction is orthogonal to the fabric surface; the finger shape can be modelled with a sphere with a given curvature radius while the contact area is approximated with a circle; the finger deformation is not relevant w.r.t. the deformation of the fabric; the elasticity of the fabric can be modeled in a symmetrical fashion, by means of two non linear springs linked each other by an inextensible wire.

After force exertion, the fabric geometry will change. The parameter α defines the angle between the fabric surface at rest and the surface after the indentation. It can be worth computed from the indentation δ, the latter can be obtained from the contact force F measured by the load cell

$$\delta = \sqrt{\frac{F}{\lambda}}, \tag{5.3}$$

where λ is the coefficient of the $F(\delta)$ quadratic curve; therefore α is

$$\alpha = \arctan\left(\frac{\delta}{l}\right) \tag{5.4}$$

where l is the half length of the fabric tactile surface. For further details see figg. 5.4 and 5.3.

The model contact area (A_{mo}) will be

$$A_{mo} \approx \pi(R_f \sin\varphi)^2. \tag{5.5}$$

where $R_f = 7\ mm$ [79]is the curvature radius of the fingertip (i.e the radius of the sphere) and is a free parameter of the model. φ is the angle between the normal passing through O – the center of the sphere modelling the fingertip – and the segment connecting O and A, the latter is the point on the fabric tangent to the sphere modelling the fingertip.

A_{mo} is centered at the point K and it is parallel to the xz plane and orthogonal to the xy plane, passing trough the point A.

Knowing the indentation of the fabric produced by the fingertip (δ) from the equation 5.3, I can define the indentation of the sphere center as

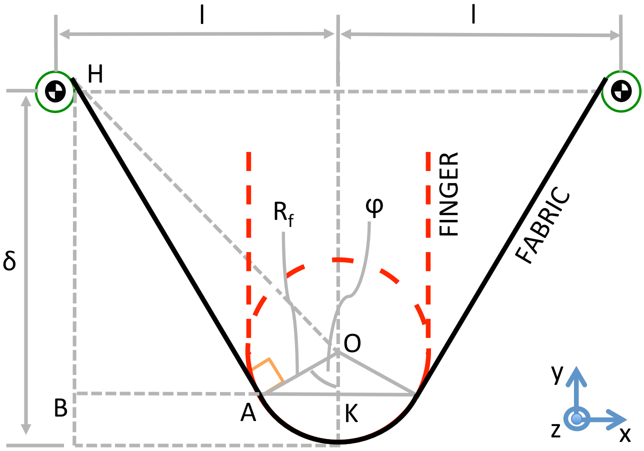

Figure 5.4: Sketch of the fingertip (red dashed line circle) contacting the elastic fabric (black line). φ is the angle between the normal passing through O – the center of the sphere (with radius R_f) modelling the fingertip – and the segment connecting O and A, i.e. the point on the fabric tangent to the sphere. δ is the indentation that the fingertip produces on the fabric, while l is the half length of the fabric tactile surface. The z axis is oriented out from the xy plane.

$$\bar{\delta} = \delta - R_f, \tag{5.6}$$

δ (and $\bar{\delta}$) is time dependent since it is strictly linked to the indentation force. For sake of readability, in the following, time dependency of δ is omitted. Computing segments $\overline{HO}$, $\overline{HA}$ and $\overline{HB}$ as

$$\overline{HO} = \sqrt{l^2 + \bar{\delta}^2}, \tag{5.7}$$

$$\overline{HA} = \sqrt{\overline{HO}^2 - {R_f}^2} = \sqrt{l^2 + \bar{\delta}^2 - {R_f}^2}, \tag{5.8}$$

$$\overline{HB} = \bar{\delta} + R_f \cos\varphi, \tag{5.9}$$

and considering that

$$\sin\varphi = \frac{\overline{HB}}{\overline{HA}}, \tag{5.10}$$

angle φ can be obtained using tangent parametric formulation as

$$\varphi_{1,2} = 2\arctan\left(\frac{-\,2\overline{HA} \pm l}{(2R_f - \bar{\delta})}\right). \tag{5.11}$$

and hence A_{mo} can be calculated.

5.3.1 Model Validation

In order to validate the proposed model, I have compared the contact area measured by the web camera (A_{me}) with the contact area computed by the model (A_{mo}) obtained during the characterization procedure. Root Mean Square Errors (RMSE) between A_{mo} and A_{me}, over all the force-area characterization curves, are considered for the comparison.

Without affecting the goodness-of-fit of the model, I introduce a correcting scaling factor (different for each characterization curve), hereinafter referred to also as C.F. (see the fourth column of table 5.1), to restore the model computation on the real measurements. I have computed RMSE (the second column of table 5.1) values also in this case, referring to it as CMRSE, with the letter C standing for Correction (cf. the fifth column of table 5.1).

In fig. 5.5 I report the comparison results for three motor positions, while in table 5.1 I report the root mean square errors of the comparison for each characterization curve with and without the correction factor. For sake of completeness I also report the percentage RMSE normalized by the maximum value of contact area measured at a a given position of the motor. I refer to it as a Percentage RMSE (RMSEP, the third column of table 5.1). Same thing is used also for CRMSE, thus obtaining the CRMSEP (cf. the sixth column of table 5.1).

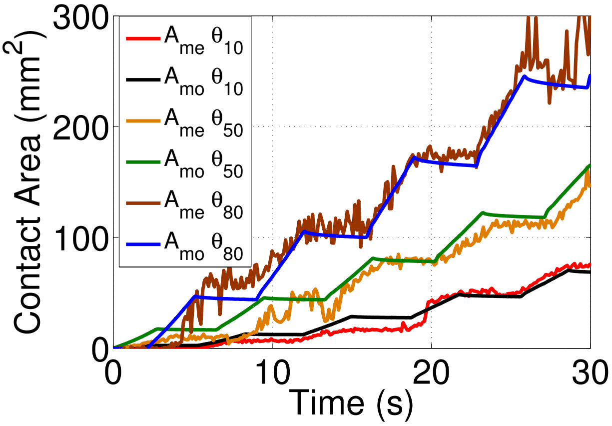

Figure 5.5: Results of model validation at three different motor positions. A_{mo} is the contact area estimated with the model while A_{me} is the measured one.

What is noticeable is that the model is able to estimate the contact area with a good level of accuracy: considering the correction factor the maximum percentage of error is less than 30%, and usually close to or less than 10%.

Since softness perception relies on both haptic channels – kinaesthesia and cutaneous information – it can be thought to be controlled to track $F(\delta)$ or $F(A)$ curves. Of course both characteristics are associated each other in the device (for a decoupling strategy of these characteristics, see e.g. [76]).

When the system behaves like a $F(\delta)$ tracker, i.e. to mimic a given stiffness, the behavior is analogous to the one exhibited by common kinaesthetic systems (which basically act as force displays [80]), although cutaneous cues are clearly vehiculated to subjects by means of fabric deformation. However, the measurement of the contact area in real-time is now available and it provides additional tactile information on the haptic interaction in act.

Since the CASR paradigm, experimentally validated, underlines

Table 5.1: Table of model errors (RMSE, RMSEP, CRMSE, CRMSEP) for different motor positions θ. C.F.s are the correcting factors.

θ (°)	RMSE (mm^2)	RMSEP (%)	C. F.	CRMSE (mm^2)	CRMSEP (%)
10	24.1	37.1	1.5	9.3	9.6
20	10.1	38.5	2	4.5	10.6
30	8.7	32.2	1.5	7.2	17.8
40	62.3	44.2	2.6	44.8	24.4
50	79.9	43.8	3.2	30.7	10.5
60	121.6	55.7	5	53.4	14.7
70	124.5	36.4	6	44.8	8.7
80	105.5	42.2	4.8	32.2	8.8

the importance of dynamically controlling the fingertip contact area growth under the indenting contact force to properly convey ness perception, the $F(A)$ tracking represents a more interesting issue. In [34], the pneumatic-CASR display was proved to be able to properly track given $F(A)$ curves; however its discrete design (a set of hollow cylinder arranged in a telescopic manner) and the lack of an effective feedback on the actual contact area limit the resolution of the stimuli. In the previous version of the device here presented [A8], the contact area was actively measured but no contact-area feedback for dynamic tracking was implemented. Finally, in [35], authors presented a softness display able to control the fingertip contact area, on the basis of the detected contact force and by suitably regulating the fluid volume within the device. Although the tracking performance was satisfac-

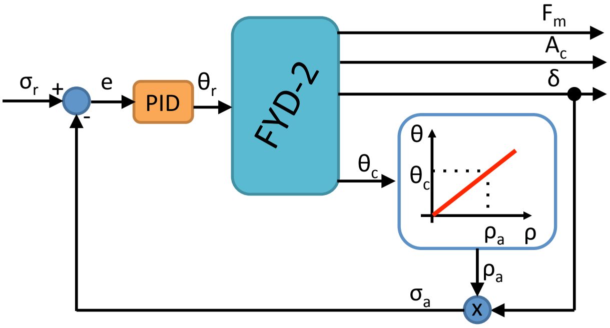

(a) Stiffness Control

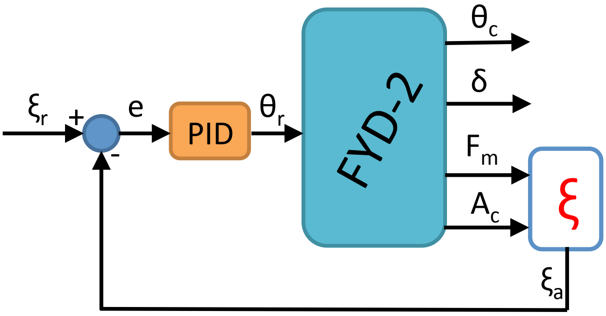

(b) F(A) Tracking Control

Figure 5.6: In the plot 5.6a I report the block diagram of the control for constant stiffness experiments, while in the plot 5.6b block diagram of the control applied for F(A) tracking is graphicated.

tory, the need to construct and store in advance the "numerical models" of the materials to be rendered reduced the mimicking reliability up to a finite set of previously numerically built materials. Here I realize a closed-loop control able to track a theoretically infinite range of specimens, since the control is based on the actual measurement of the contact area provided in real-time by the web camera.

5.3.2 Constant Stiffness Tracking

In this experiment I try to track a constant stiffness $\sigma_r = 1\ N/mm$. Since the fabric stiffness is not constant but it depends on the indentation, I need to suitably control motor positions on the basis of the actual δ (see 5.3).

To control the stiffness (block diagram reported in fig. 5.6a, I need to first know the actual stiffness (σ_a in $[N/mm]$) of the fabric. Hence, I first get the angular coefficient (ρ_a in $[N/mm^2]$) of the actual stiffness curve, which depends on the motor position (θ_c), from the characterization characteristics or interpolating between them

$$\sigma_a = \rho_a \delta, \tag{5.12}$$

Second, a PI control is used to move the motor positions, based on the error between σ_r (reference stiffness) and σ_a (actual stiffness), with heuristically found constants $P = 1$, $I = 0.01$.

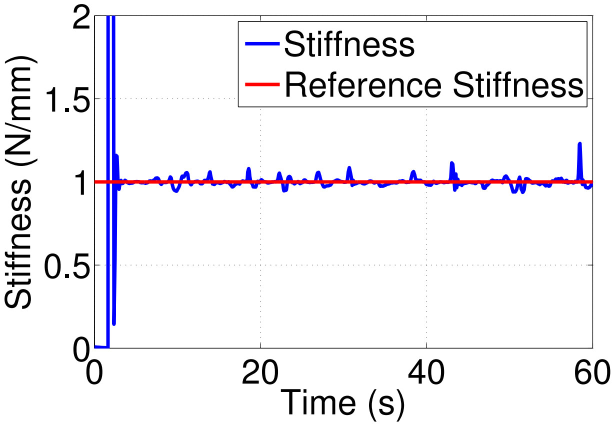

Figure 5.7: Stiffness control (blue line) vs. stiffness reference (red line).

In fig. 5.7 the result of the control is reported. In this case, after

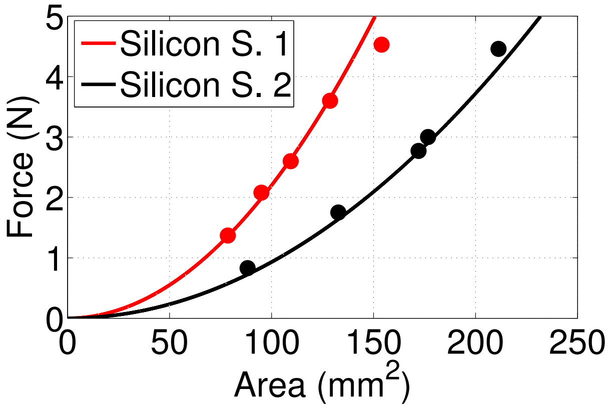

Figure 5.8: Experimental $F(A)$ characteristics of two silicon specimens.

the initial transitory phase due to motor positioning, I get a RMSE of 0.1879 N/mm, less than 20% w.r.t. the reference value.

5.3.3 Trajectory Area Tracking

$F(A)$ characteristics are linear at fixed motor positions; therefore, linear $F(A)$ curves can be simply mimicked by interpolating motor positions over the characterization graphs. However, to reproduce common quadratic $F(A)$ characteristics [34], the position of the motors needs to be controlled and suitably changed, based on the actual contact area. Starting from the $F(A) = \xi_r A_r^2$ (ξ_r in $[N/mm^4]$) curve to be tracked, the actual ξ_a $[N/mm^4]$ coefficient can be obtained each time by suitably dividing the measured indented force by the squared measured area A_m. A PI control is then used to move the motors, based on the error between ξ_r and the actual ξ_a (see fig. 5.6b).

In this case, the PI constants are heuristically set as: $P = 5$ and $I = 0.3$.

To properly validate the system performance in $F(A)$ tracking, two different silicon specimens, specimen 1 and specimen 2, were chosen to be reproduced.

I derived the properties between the contact force and the contact area, by measuring the indented force while the silicon specimen was touched by the fingertip. The specimen was placed on a load-cell and the surface of the material covered by a transparent plastic sheet. The finger pad was colored using ink. The contact area was obtained by measuring the scanned contact area images.

The procedure is analogous to the one reported in [35]. The characteristics are reported in fig. 5.8. The contact force was within the range of 0.5 to 4.5 N. The $F(A)$ tracking experiments were performed by touching the fabric with the finger, using an indenting velocity of the finger tip of 30 mm/s.

The $F(A)$ tracking results are reported in figg. 5.9 and 5.10 for the silicon specimens 1 and 2, respectively. In these cases, the couples (Measured Controlled Area, Measured Force) are indicated as red dots.

For specimen 1, $\sim 75\%$ of the controlled couples is within the $\pm 25\%$ of the reference bounds, while for specimen 2, $\sim 72,4\%$ of the controlled couples is within the $\pm 25\%$ of the reference bounds. The corresponding reference area is tracked with a RMSE of 18.05 mm^2 and a RMSEP of 7.28% (w.r.t. the reference value), for the specimen 1 (cf. fig. 5.9a), and for specimen 2 I get a RMSE of 45.1 mm^2 and a RMSEP of 15.1% (for sake of space I do not report the relative plot).

What is noticeable is that the tracking accuracy is reasonably acceptable; of course, it can be improved, e.g. by using a different programming environment (e.g. C++) instead of MATLAB/SIMULINK to increase control performance. In this manner, I might be able to enhance the accuracy and to mimic curves when faster indentation velocities are used. However, up to my knowledge, for the first time, force-area curves can be reproduced using the system here presented on the basis of the feedback of real-time measured area.

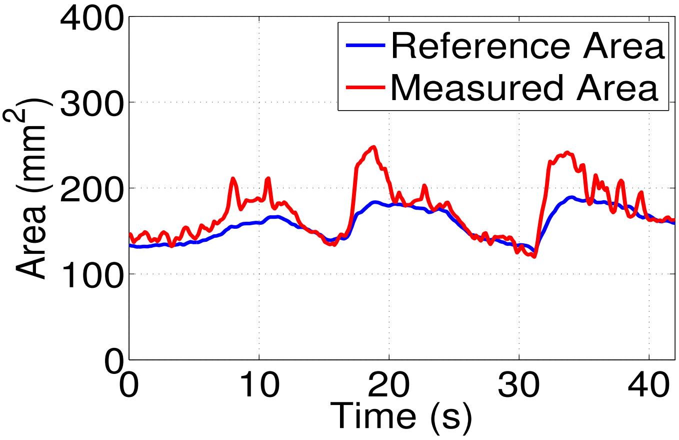

(a) Measured Area control

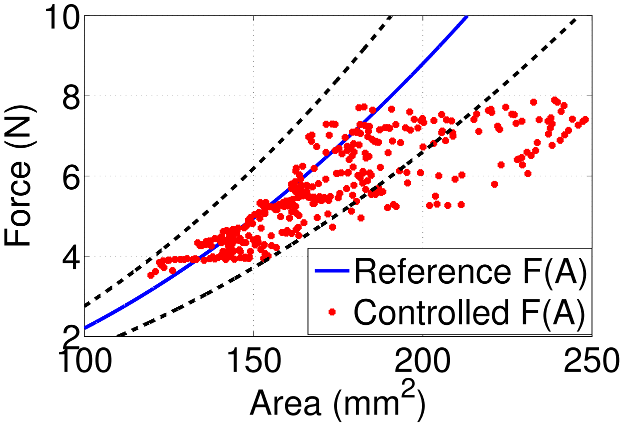

(b) F(A) characteristic

Figure 5.9: In the first plot 5.9a I report the contact area tracking control (red line) vs. contact area reference (blue line). In the second plot 5.9b I show the reference $F(A)$ curve (in blue) while the pairs (measured controlled area, measured force) are represented as red dots. The ±25% interval bounds w.r.t the reference curve are represented as black dashed lines. These plots refer to the silicon specimen 1.

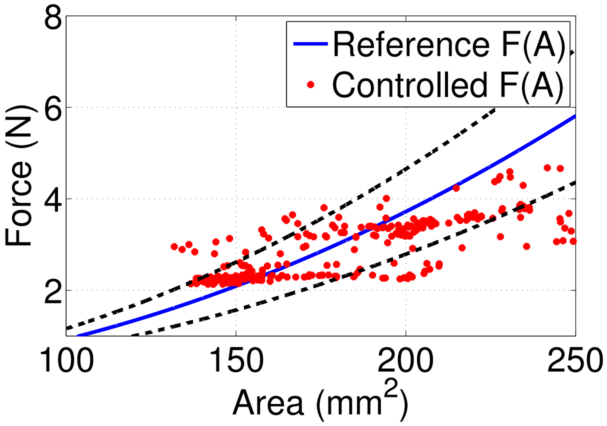

Figure 5.10: In this figure I show the reference $F(A)$ curve (in blue) while the pairs (measured controlled area, measured force) are represented as red dots. The ±25% interval bounds referred w.r.t the reference curve are represented as black dashed line. This plot refers to the silicon specimen 2.

Chapter 6

Sensorized Object and Contact Point Detection

THIS CHAPTER presents three different calibration methods for a 36 axis F/T sensor (see fig. 6.1). This sensor is the core of a sensorized object employed for contact point computations in human grasping tasks. The object can assume different shape by simply changing the patches attached on the sensor (see fig. 6.2).

Moreover I introduce an algorithm to identify the contact point position on a surface patch through the measurements of the corresponding face force and torque.

Finally, I report a comparison between contact point detection applied on a commercial F/T sensor and on sensorized object (for more details see also [A11]).

6.1 Calibration Methods

In the calibration procedures here presented I used an ATI Delta force/torque sensor for measuring wrenches applied on the custom made sensor and two types of calibration flanges (with known dimension) to fix the device to the ATI sensor (for more detail see also fig.

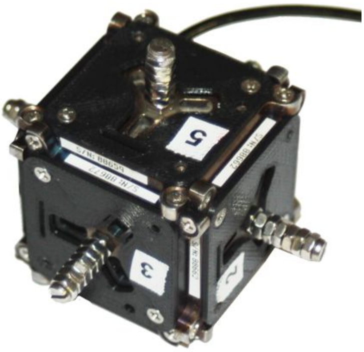

Figure 6.1: The custom made 36 axis F/T sensor.

Figure 6.2: The patches applied on the sensorized object allow to compose different shape: a sphere, a cube or an ellipsoid.

6.3). Calibration was performed without attaching any surface patch to the active surfaces. The first flange (see fig. 6.4) is fixed on the 36 axis F/T sensor frame thus, not allowing to measure strain gauge deformations of the corresponding face. The second flange (see fig. 6.13) is fixed on one face of the 36 axis F/T sensor and allows measurement of the strain gauges of all active faces. The generic active faces deformations are measured by 6 strain gauges.

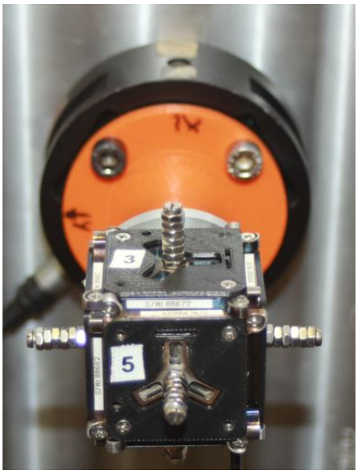

Figure 6.3: The calibration setup. The custom made 36 F/T sensor is fixed on a flange. Then the flange is screwed in the ATI Delta F/T sensor (black cylinder in figure).

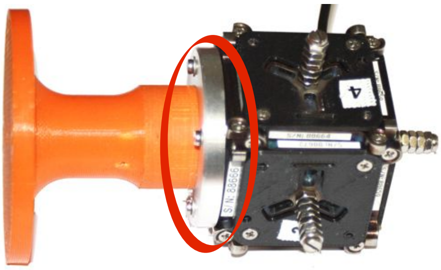

Figure 6.4: The first type of flange employed in face by face calibration e in quasi total calibration methods.

6.1.1 Face by Face Calibration

If the 6 strain gauges of each active face are completely decoupled from those of the others, i.e a wrench applied on a face does not produce any relevant deformation on the strain gauges of the other faces, a face to face calibration procedure can be applied.

This consists of applying a known wrench W_i (in this case measured by ATI Delta force/torque sensor) on a face and correlating it with the strain gauges measurements, as

$$W_i = C_i S_i, \tag{6.1}$$

where $W_i \in \mathbb{R}^{6\times 1}$ is the wrench vector applied on the i-th face, $C_i \in \mathbb{R}^{6\times 6}$ is the calibration matrix of the i-th face and $S_i \in \mathbb{R}^{6\times 1}$ is the strain gauge measurements of the i-th face.

Now, it is possible to compute the calibration matrix as

$$C_i = W_i S_i^{\dagger} \tag{6.2}$$

where $S_i^{\dagger}$ is the pseudo-inverse of matrix S_i.

Since the sensor has 6 independent active faces, the calibration method has to be repeated six times (i.e with $i = 1, 2, ..., 6$) and each face will have its calibration matrix.

Moreover, to obtain a more precise calibration matrix it is possible to apply and record more than one wrench.

With this assumption equation 6.2 can be rewritten as

$$\bar{C_i} = \bar{W_{i,k}} \bar{S_{i,k}}^{\dagger}, \tag{6.3}$$

where $\bar{W}_{i,k} \in \mathbb{R}^{6\times k}$ and $\bar{S}_{i,k} \in \mathbb{R}^{6\times k}$ are the recorded wrench and the recorded measurement of the staring gauges matrix, respectively. k the number of the trials.

6.1.1.1 Face by Face Calibration Results

Results of the calibration methods are reported in fig. 6.5–6.8. As it possible to notice this kind of calibration does not produce acceptable results.

Probably, this fact is due to the coupling phenomena of the faces. In fact, even if the load wrench is applied on only one face, the string gauges of the other faces are stressed, producing fictitious wrenches.

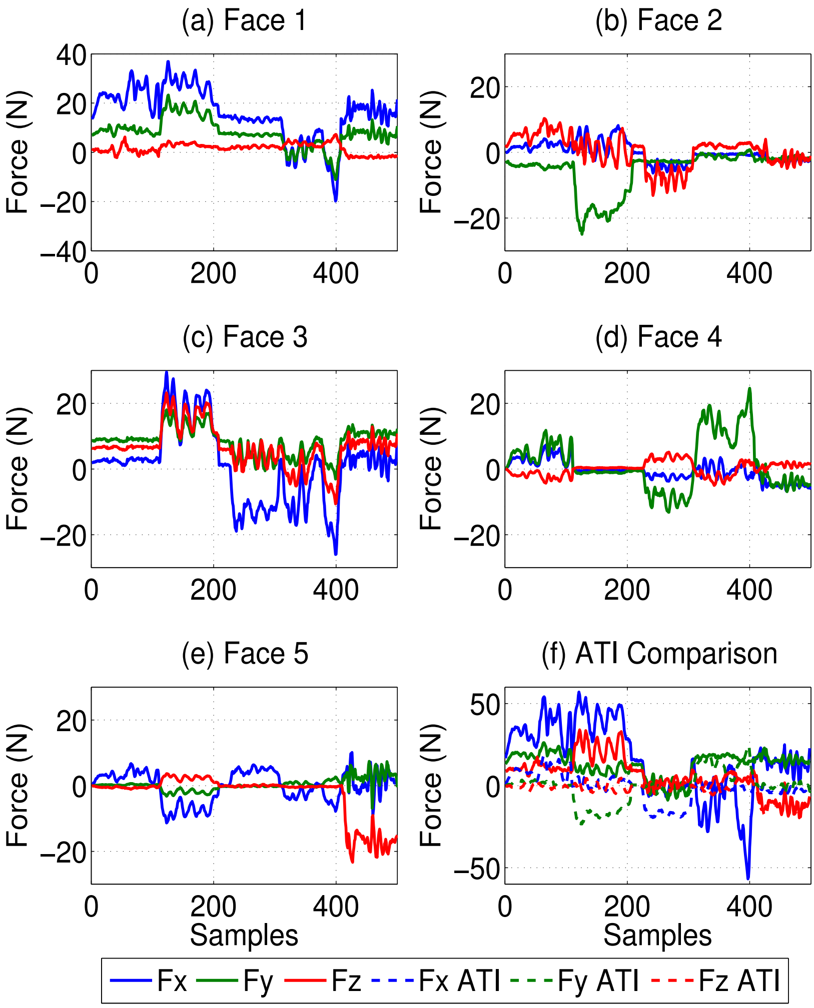

Figure 6.5: In this experiment only one face at a time was touched, from face 1 by face 5 (fig. a - e), with face to face calibration. Forces read by the object are shown with solid line. In fig. f I report the comparison with ATI force/torque sensor (dashed line).

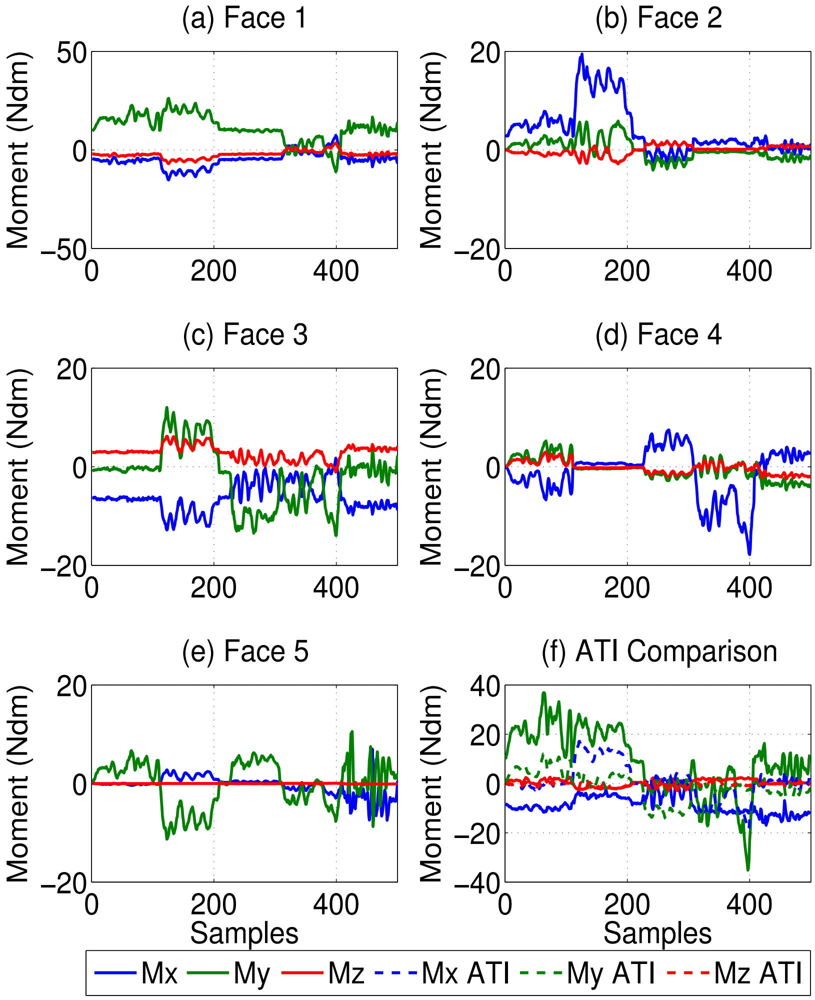

Figure 6.6: In this experiment only one face at a time was touched, from face 1 to face 5 (fig. a - e), with face by face calibration. Moments read by the object are shown with solid line. In fig. f I report the comparison with ATI force/torque sensor (dashed line).

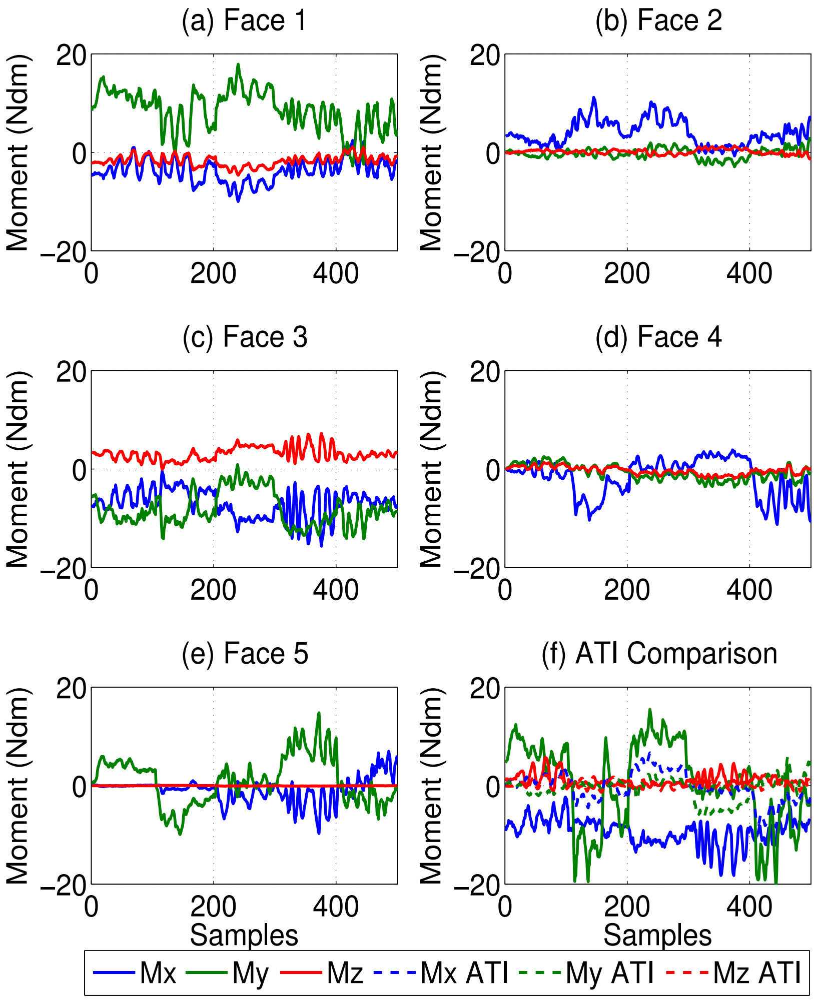

Figure 6.7: In this experiment two face at a time were touched in sequence (faces 1-3, faces 2-4, faces 5-2, faces 5-3 and faces 5-4) with face by face calibration. Forces read by the object are shown with solid line. In fig. f I report the comparison with ATI force torque sensor (dashed line).

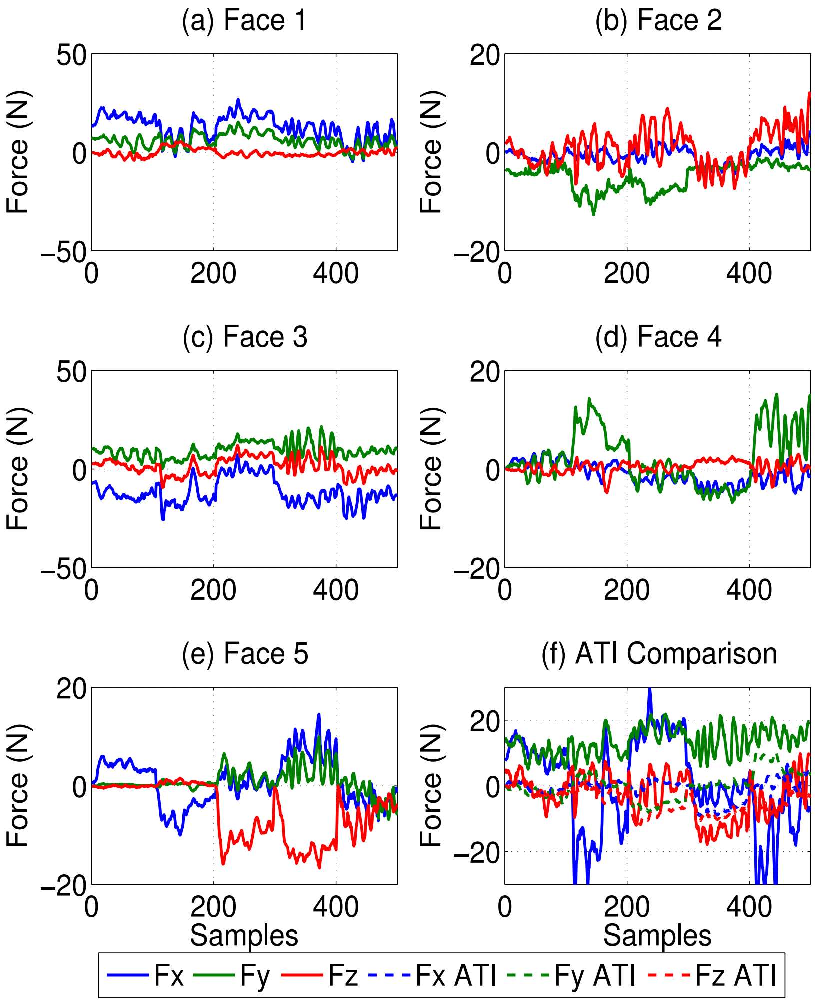

Figure 6.8: In this experiment two face at a time were touched in sequence (faces 1-3, faces 2-4, faces 5-2, faces 5-3 and faces 5-4) with face by face calibration. Moments read by the object are shown with solid line. In fig. f I report the comparison with ATI force torque sensor (dashed line).

6.1.2 Quasi Global Calibration

In this calibration method I apply a wrench on each face at a time in sequence, starting from active face 1 to active face 5.

For this calibration method flange 1 (see fig. 6.4) is used. This flange does not allow to apply a wrench on the active face where the flange is fixed.

Supposing to fix the flange on face 6 and considering to collect load wrenches ($W_i \in \mathbb{R}^{6\times1}$ with $i = 1, ..., 5$) applied on each face, a matrix

$$\bar{W} = \left[\begin{array}{c|c|c|c|c} W_1 & 0 & 0 & 0 & 0 \\ 0 & W_2 & 0 & 0 & 0 \\ 0 & 0 & W_3 & 0 & 0 \\ 0 & 0 & 0 & W_4 & 0 \\ 0 & 0 & 0 & 0 & W_5 \end{array}\right], \tag{6.4}$$

where $0 \in \mathbb{R}^{6\times1}$ is a vector of zero elements, is obtained.

Consequently, I collect the strain gauge measurements in a matrix

$$\bar{S} = \begin{bmatrix} S_1^1 & S_1^2 & S_1^3 & S_1^4 & S_1^5 \\ S_2^1 & S_2^2 & S_2^3 & S_2^4 & S_2^5 \\ S_3^1 & S_3^2 & S_3^3 & S_3^4 & S_3^5 \\ S_4^1 & S_4^2 & S_4^3 & S_4^4 & S_4^5 \\ S_5^1 & S_5^2 & S_5^3 & S_5^4 & S_5^5 \\ S_6^1 & S_6^2 & S_6^3 & S_6^4 & S_6^5 \end{bmatrix}, \tag{6.5}$$

where $S_i^j \in \mathbb{R}^{6\times1}$ is the strain gauges measurement of the $i - th$ face when it is applied a wrench on the $j - th$ face. Matrices 6.4 and 6.5 are correlated by

$$\bar{W} = \bar{C}\bar{S} \tag{6.6}$$

were $\bar{C} \in \mathbb{R}^{30\times 36}$ is the calibration matrix.

From 6.6, it is possible to compute the calibration matrix $\bar{C}$ as

$$\bar{C} = \bar{W}\bar{S}^{\dagger}, \tag{6.7}$$

where $\bar{S}^{\dagger}$ is the pseudo inverse of $\bar{S}$.

Moreover, to obtain a more precise calibration matrix it is possible to apply and record more than one wrench.

With this assumption equation 6.6 can be rewritten as

$$\bar{C}_i = \bar{W}_{i,k}\bar{S}^{\dagger}_{i,k}, \tag{6.8}$$

where $\bar{W}_{i,k} \in \mathbb{R}^{36\times k}$ and $\bar{S}_{i,k} \in \mathbb{R}^{36\times k}$ are the recorded wrench and the recorded measurement of the staring gauges matrix, respectively. k the number of the trials.

6.1.2.1 Quasi Global Calibration Results

Results of the calibration methods are reported in fig. 6.9–6.12. This calibration presents better results than face by face.

In fact, in this case the calibration takes into account the entire deformation of the custom made F/T sensor and even if a load wrench applied on a face produces some deformations of the strain gauges of the other faces, this method "learn" where the wrench is applied.

Principally, the "learning" is linked to the construction of the matrices $\bar{W}$ (6.4) and $\bar{S}$ (6.5) where I collect the wrenches applied and the strain gauges deformations during the calibration phase, respectively.

The only technical problem of this calibration method is the non accessibility of the face where the flange is fixed.

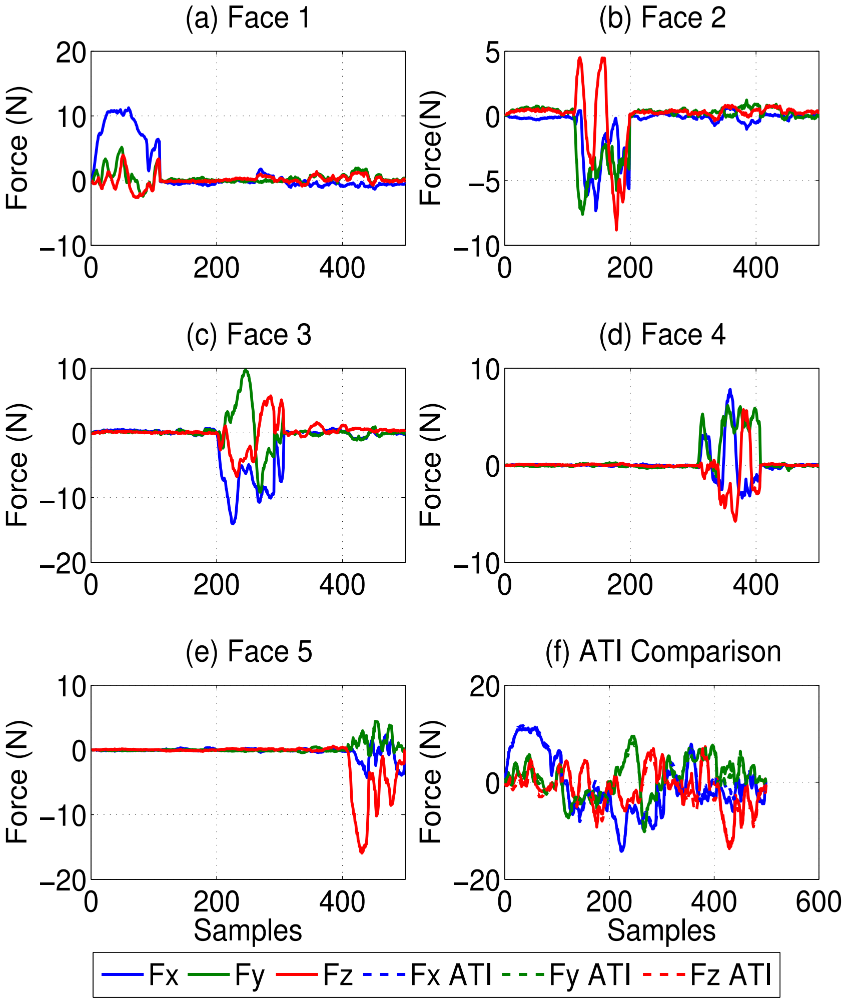

Figure 6.9: In this experiment only one face at a time was touched, from face 1 to face 5 (fig. a - e), with quasi global calibration. Forces read by the object are shown with solid line. In fig. f I report the comparison with ATI force/torque sensor (dashed line).

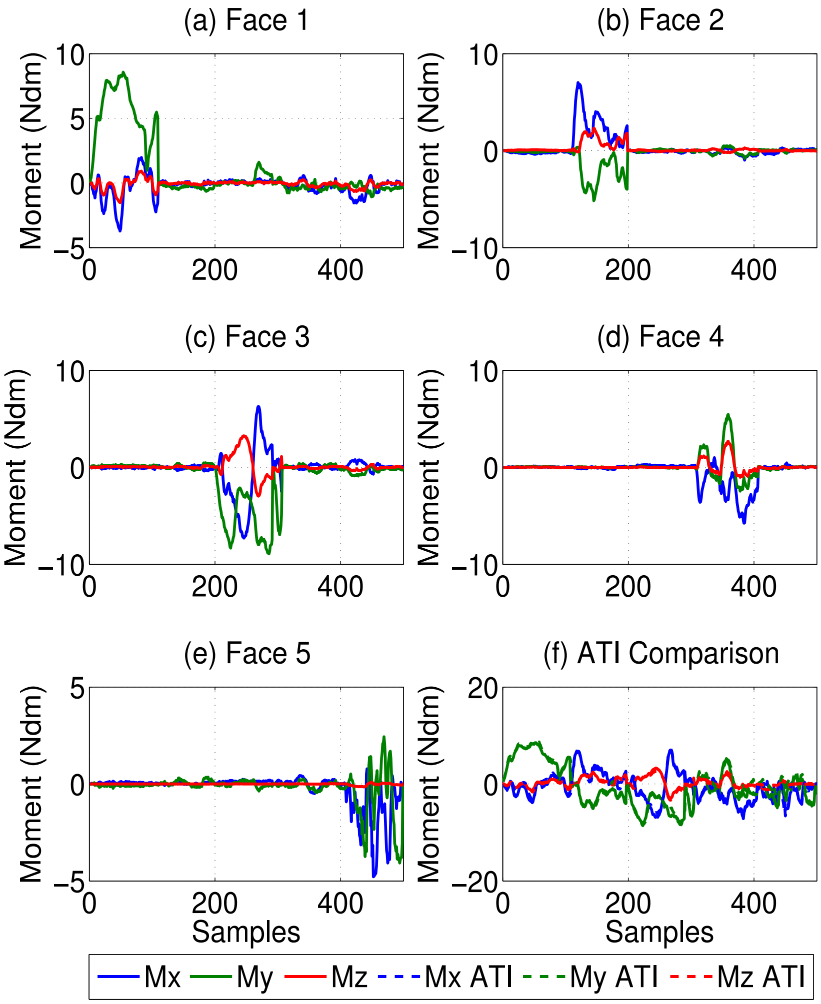

Figure 6.10: In this experiment only one face at a time was touched, from face 1 to face 5 (fig. a - e), with quasi global calibration. Moments read by the object are shown with solid line. In fig. f I report the comparison with ATI force/torque sensor (dashed line).

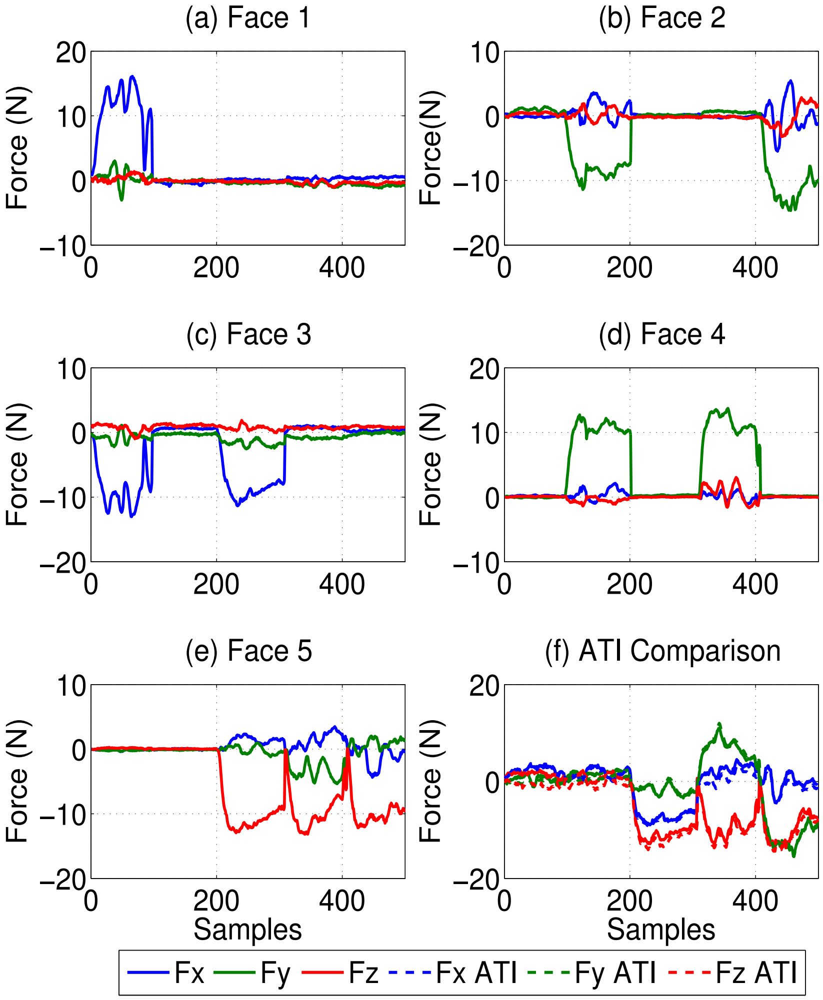

Figure 6.11: In this experiment two face at a time were touched in sequence (faces 1-3, faces 2-4, faces 5-2, faces 5-3 and faces 5-4) with quasi global calibration. Forces read by the object are shown with solid line. In fig. f I report the comparison with ATI force torque sensor (dashed line).

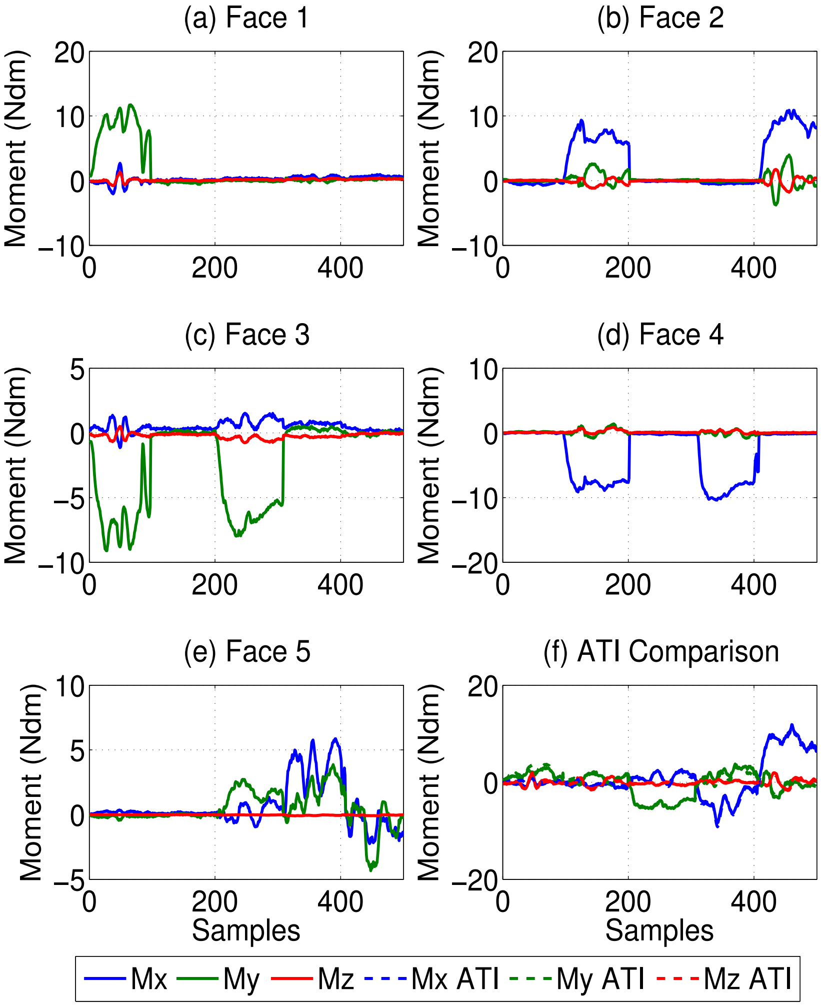

Figure 6.12: In this experiment two face at a time were touched in sequence (faces 1-3, faces 2-4, faces 5-2, faces 5-3 and faces 5-4) with quasi global calibration. Moments read by the object are shown with solid line. In fig. f I report the comparison with ATI force torque sensor (dashed line).

6.1.3 Global Calibration

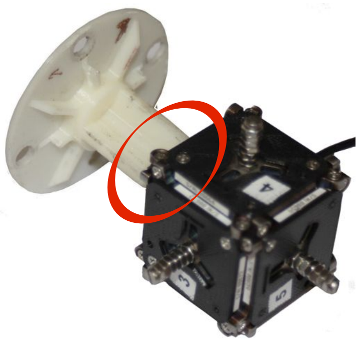

Figure 6.13: The Second type of flange employed in total calibration method.

In this calibration method I apply a wrench on each face at a time in sequence, starting from active face 1 to active face 6.

For this calibration method flange 2 (see fig. 6.13) is used. This flange allows to apply a wrench also on its active face. Supposing to fix the flange on face 6 and considering to collect load wrenches ($W_i \in \mathbb{R}^{6\times1}$ with $i = 1, ..., 6$) applied on each face, a matrix

$$\hat{W} = \left[\begin{array}{c|c|c|c|c|c} W_1 & 0 & 0 & 0 & 0 & 0 \\ 0 & W_2 & 0 & 0 & 0 & 0 \\ 0 & 0 & W_3 & 0 & 0 & 0 \\ 0 & 0 & 0 & W_4 & 0 & 0 \\ 0 & 0 & 0 & 0 & W_5 & 0 \\ W_1^6 & W_2^6 & W_3^6 & W_4^6 & W_5^6 & W_6 \end{array}\right], \tag{6.9}$$

where $0 \in \mathbb{R}^{6\times1}$ is a vector of zero elements, is obtained.

Consequently, I collect the strain gauge measurements in a matrix

$$\bar{S} = \begin{bmatrix} S_1^1 & S_1^2 & S_1^3 & S_1^4 & S_1^5 & S_1^6 \\ S_2^1 & S_2^2 & S_2^3 & S_2^4 & S_2^5 & S_2^6 \\ S_3^1 & S_3^2 & S_3^3 & S_3^4 & S_3^5 & S_3^6 \\ S_4^1 & S_4^2 & S_4^3 & S_4^4 & S_4^5 & S_4^6 \\ S_5^1 & S_5^2 & S_5^3 & S_5^4 & S_5^5 & S_5^6 \\ S_6^1 & S_6^2 & S_6^3 & S_6^4 & S_6^5 & S_6^6 \end{bmatrix} \tag{6.10}$$

where $S_i^j \in \mathbb{R}^{6\times 1}$, is the strain gauges measurement of the $i-th$ face with applied the $j-th$ wrench. Matrices 6.9 and 6.10 are correlated by

$$\hat{W} = \hat{C}\hat{S} \tag{6.11}$$

where $\hat{C} \in \mathbb{R}^{36\times 36}$ is the calibration matrix.

From 6.11, it is possible to compute the calibration matrix $\hat{C}$ as

$$\hat{C} = \hat{W}\hat{S}^{\dagger}, \tag{6.12}$$

where $\hat{C}^{\dagger}$ is the pseudo inverse of $\hat{C}$.

Moreover, to obtain a more precise calibration matrix it is possible to apply and record more than one wrench.

With this assumption equation 6.11 can be rewritten as

$$\hat{C}_i = \hat{W}_{i,k}\hat{S}_{i,k}^{\dagger}, \tag{6.13}$$

where $\bar{W}_{i,k} \in \mathbb{R}^{6\times k}$ and $\bar{S}_{i,k} \in \mathbb{R}^{6\times k}$ are the recorded wrench and the recorded measurement of the staring gauges matrix, respectively. k the number of the trials.

6.1.3.1 Global Calibration Results

Results of the calibration methods are reported in fig. 6.14–6.17. This calibration presents better results than the other calibration methods.

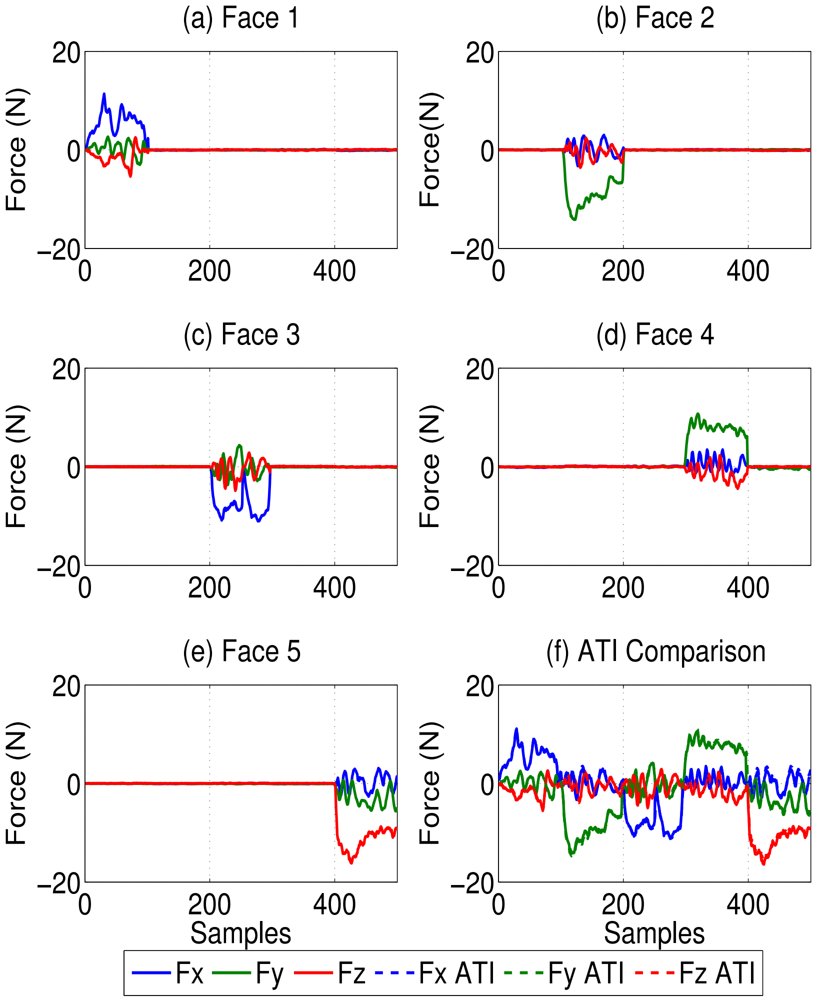

Figure 6.14: In this experiment only one face at a time was touched, from face 1 to face 5 (fig. a - e), with global calibration. Forces read by the object are shown with solid line. In fig. f I report the comparison with ATI force/torque sensor (dashed line).

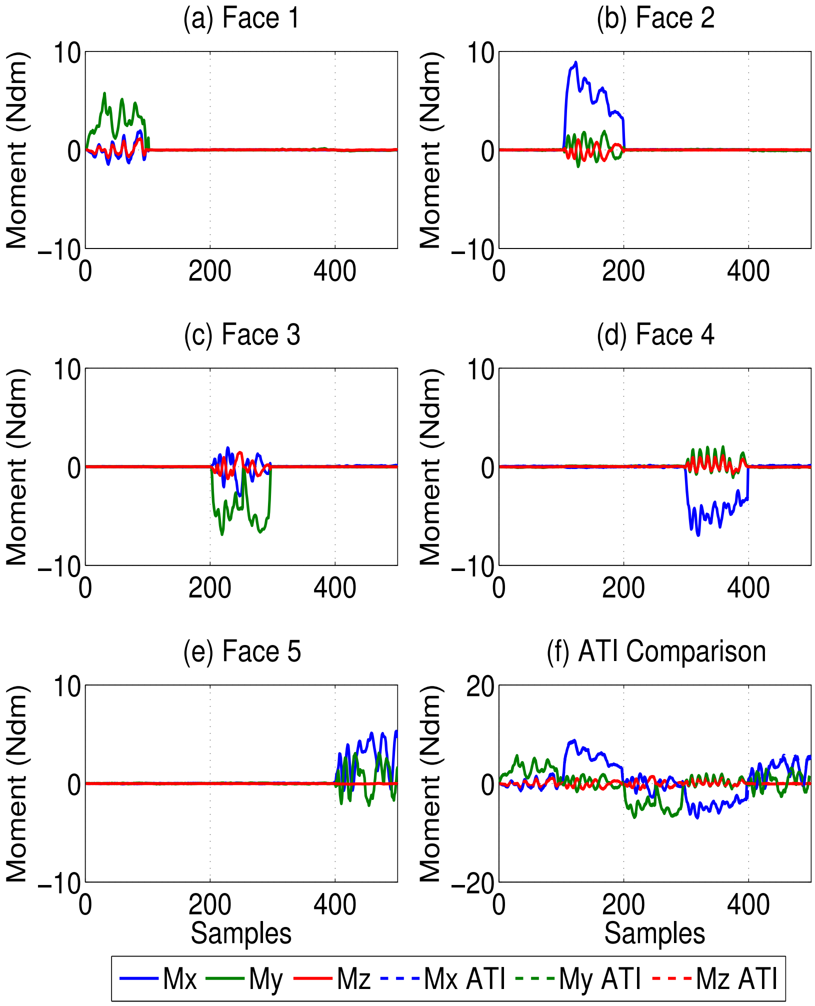

Figure 6.15: In this experiment only one face at a time was touched, from face 1 to face 5 (fig. a - e), with global calibration. Moments read by the object are shown with solid line. In fig. f I report the comparison with ATI force/torque sensor (dashed line).

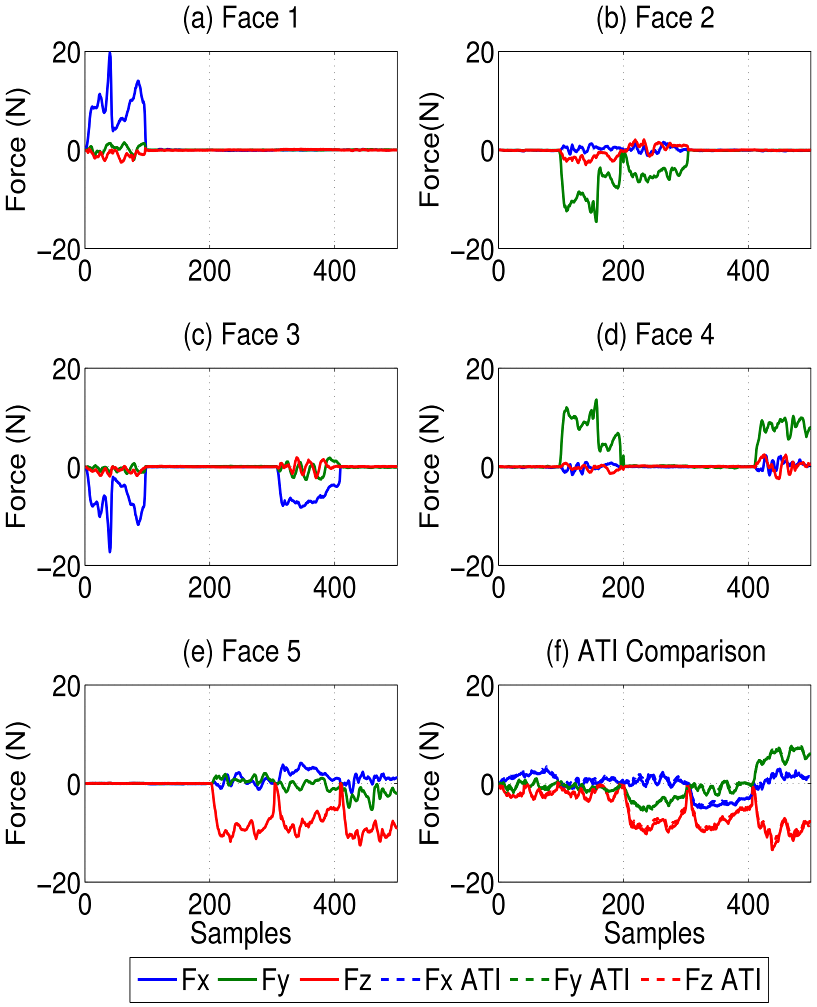

Figure 6.16: In this experiment two face at a time were touched in sequence (faces 1-3, faces 2-4, faces 5-2, faces 5-3 and faces 5-4) with global calibration. Forces read by the object are shown with solid line. In fig. f I report the comparison with ATI force torque sensor (dashed line).

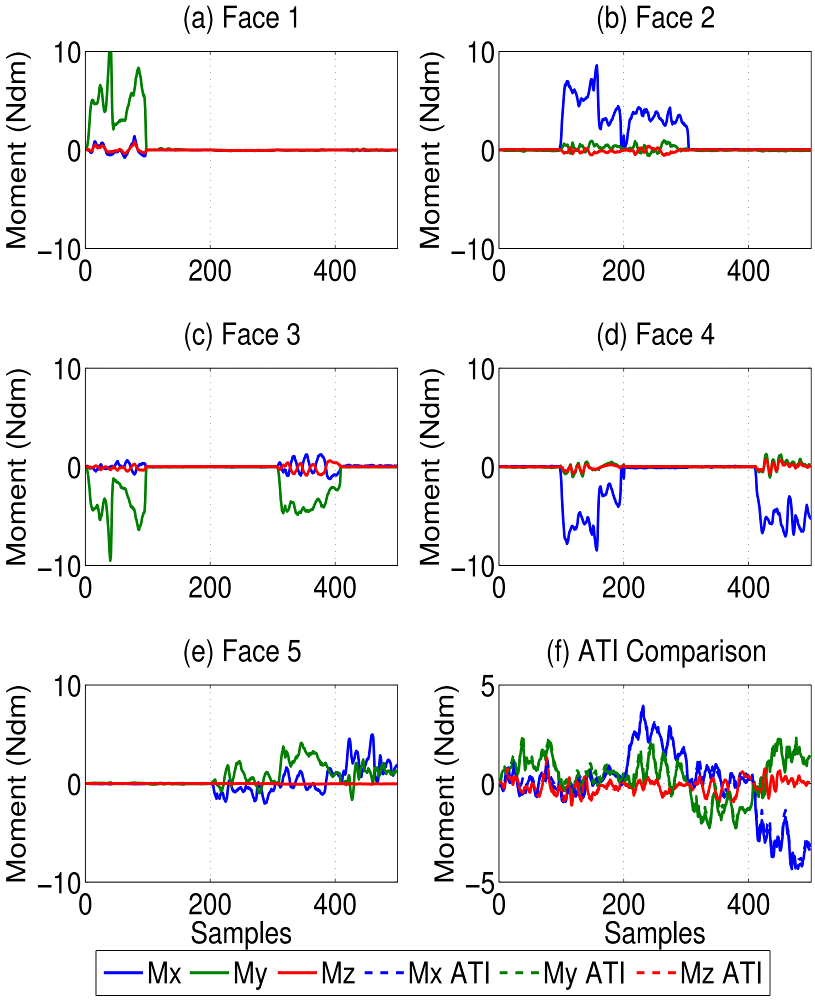

Figure 6.17: In this experiment two face at a time were touched in sequence (faces 1-3, faces 2-4, faces 5-2, faces 5-3 and faces 5-4) with global calibration. Moments read by the object are shown with solid line. In fig. f I report the comparison with ATI force torque sensor (dashed line).

Now, all the faces are accessible and with the global calibration method it is possible to recognize and measure with a good accuracy the wrenches applied.

6.2 Contact Point Detection Algorithm

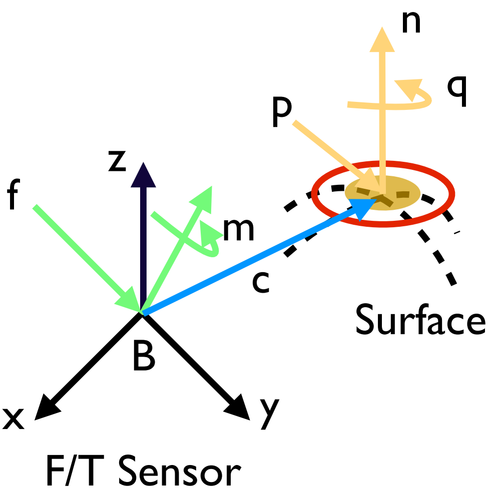

Figure 6.18: Schematic of the application of the contact point algorithm with its main physical characteristics.

Given the measurements f and m (from torque-force sensor), together with a surface equation $S() = 0$, I want to determine the location of contact centroid c, and the related contact force p and moment q.

Starting from the force-torque equation of equilibrium

$$\begin{cases} f = p \\ m = q + p \times c \end{cases}, \tag{6.14}$$

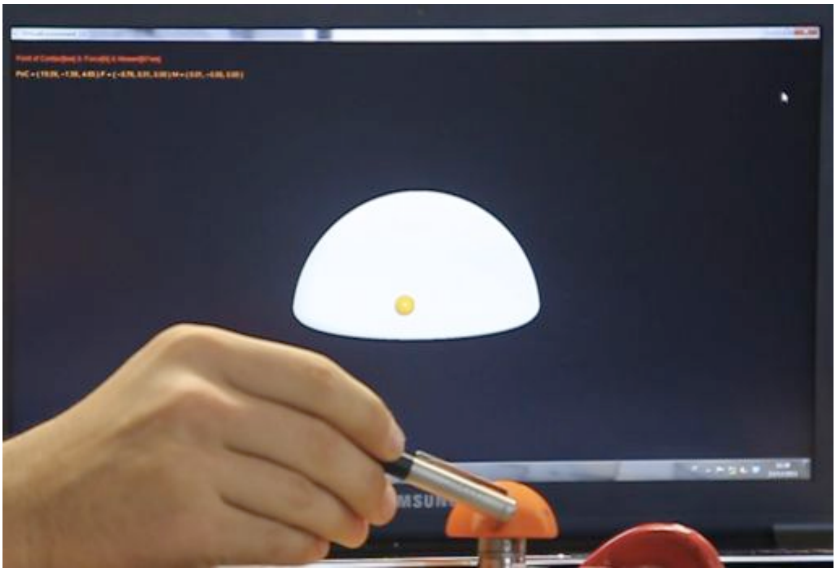

Figure 6.19: Sanpshot of the toolbox implemented for the contact pony detection. On the close up it is possible to notice the F/T sensor with an hemispherical surface. In background it is possible to notice the algorithm computation (yellow point).

and from the equation of the normal to the surface in the contact point

$$q = K\frac{\nabla S(c)}{||\nabla S(c)||} = Kn, \tag{6.15}$$

given together with an ellipsoidal surface

$$r^T A^T A r - R^2 = 0, \tag{6.16}$$

where r is $\mathbb{R}^3$ vector of the Cartesian coordinates, A is the matrix which defines the shape of the ellipsoid (i.e a plane, a sphere, a cylinder or a generic ellipsoid) and R the offset to the ellipsoid center, the

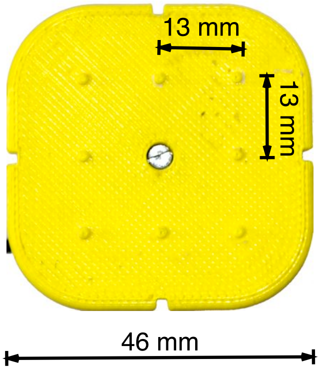

Figure 6.20: Patch employed for the contact point detection.

algorithm compute the contact point c of an object touching the know surface.

Expanding the 6.15 I get a non linear systems of 10 equation in 10 unknowns. Moreover, considering as the know surface an ellipsoidal surface (i.e 6.16) the system has a closed form solution. The complete algorithm is reported in [81].

For this algorithm a toolbox was implemented, both for Matlab and C++ environment (see fig. 6.19 for a snapshot). The toolbox is available at the address [W18].

6.3 Contact Point Comparison

To assess the accuracy of the contact point reconstructions, a comparison between the algorithm presented in [81] and implemented in [W18] applied on the custom made sensor and a commercial one was performed.

The algorithm was employed with a surface patch for the cubical shape (i.e I use one face of the 36 axis F/T sensor). Then the same surface patch was fixed on the ATI Nano 17 commercial F/T sensor.

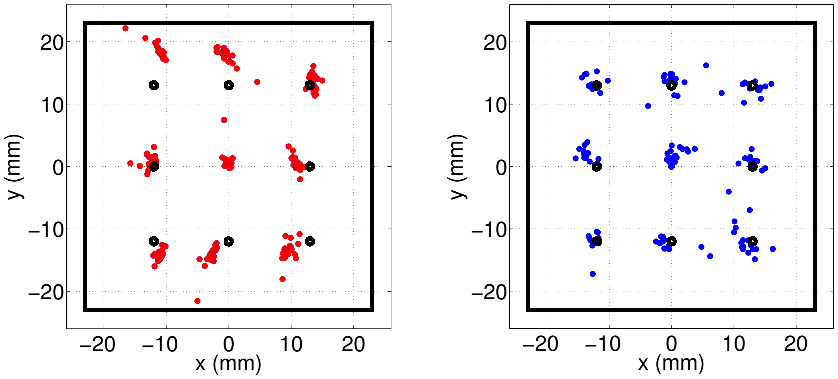

(a) ATI Nano Contact Points (b) Sensorized Object Contact Points

Figure 6.21: Contact points algorithm tested with ATI Nano 17. Reference points (black) were touched with fingertip (one at a time). Red points are the algorithm results on the ATI Nano F/T sensor. Blue point are the algorithm results on the face 5 of the custom made F/T sensor.

The contact surface was a square of 46 × 46 mm with 8 points. These points lie on the edges of a 26 × 26 mm square (see 6.20).

The experimental task was performed touching the points (one at a time) with fingertip and then touching the center of the surface patch.

The accuracy of the custom made 36 axis F/T sensor after the calibration was in the order of 3 mm, which is enough for its employment. In fig. 6.21 I report the results.

Bibliography

Author's

[A1] A. Serio, M. G. Catalano, G. Grioli, M. Gabiccini, and A. Bicchi, “The hand embodied,” in *Automatica.it 2011*, Pisa, Italy, September, 7 - 9 2011.

[A2] M. G. Catalano, G. Grioli, A. Serio, E. Farnioli, C. Piazza, and A. Bicchi, “Adaptive synergies for a humanoid robot hand,” in *IEEE-RAS International Conference on Humanoid Robots*, Osaka, Japan, 2012, best Paper Award.

[A3] M. G. Catalano, G. Grioli, A. Serio, C. Piazza, E. Farnioli, and A. Bicchi, “Adaptive synergies for the design and control of the pisa–iit softhand,” *International Journal of Robotics Research*, Submitted.

[A4] G. Grioli, M. G. Catalano, M. Garabini, F. Bonomo, A. Serio, P. Salaris, F. A. W. Belo, M. Mancini, A. Bicchi, and A. Passaglia, “Variable stiffness actuators: muscles for the next generation of robots,” in *Automatica.it 2011*, Pisa, Italy, September, 7 - 9 2011.

[A5] A. Serio, G. Grioli, I. Sardellitti, N. G. Tsagarakis, and A. Bicchi, "A decoupled impedance observer for a variable stiffness robot," in *2011 IEEE International Conference on Robotics and Automation*, Shangai, China, May 9 - 13 2011, pp. 5548 – 5553.

[A6] M. Bianchi, A. Serio, E. P. Scilingo, and A. Bicchi, "Rendering softness: a new fabric yielding display," in *Workshop for young researchers on human - friendly robotics - Symposium*, Sestri levante (Ge), Italy, December 3 2009.

[A7] M. Bianchi, E. P. Scilingo, A. Serio, and A. Bicchi, "A new softness display based on bi-elastic fabric." IEEE Computer Society, 2009, pp. 382–383.

[A8] M. Bianchi, A. Serio, E. P. Scilingo, and A. Bicchi, "A new fabric-based softness display," in *Proc. IEEE Haptics Symposium*, 2010, pp. 105 –112.

[A9] A. Serio, M. Bianchi, and A. Bicchi, "A device for mimicking the contact force/contact area relationship of different materials with applications to softness rendering," *International Conference of Intelligent Robots and Systems - IROS 2013*, Submitted.

[A10] ——, "A 'haptic synergy–based" approach to convey softness information: a fabric–based tactile display," *Workshop in IEEE International Conference on Robotics and Automation, ICRA*, 2013.

[A11] A. Serio, M. Gabiccini, I. Sarakoglou, and A. Bicchi, "Calibration and test of a multi-touch tactile object," in *International Conference of Intelligent Robots and Systems - IROS 2012*, Algrave, Portugal, 2012.

Web

[W12] [Online]. Available: www.viactors.eu

[W13] [Online]. Available: www.forcedimension.com

[W14] [Online]. Available: www.dimensionengineering.com

[W15] [Online]. Available: www.ni.com

[W16] [Online]. Available: www.mectex.com

[W17] [Online]. Available: www.mathworks.com

[W18] [Online]. Available: www.thehandembodied.eu/tools

Miscellaneous

[19] J. Zheng, S. De La Rosa, and A. Dollar, "An investigation of grasp type and frequency in daily household and machine shop tasks," in *Robotics and Automation (ICRA), 2011 IEEE International Conference on.* IEEE, 2011, pp. 4169–4175.

[20] M. Santello, M. Flanders, and J. F. Soechting, "Postural hand synergies for tool use," *The Journal of Neuroscience*, vol. 18, no. 23, pp. 10 105–10 115, 1998.

[21] A. Bicchi, M. Gabiccini, and M. Santello, "Modelling natural and artificial hands with synergies," *Philosophical Transactions of the Royal Society B: Biological Sciences*, vol. 366, no. 1581, pp. 3153–3161, 2011.

[22] A. G. Feldman and M. F. Levin, "The equilibrium-point hypothesis–past, present and future," in *Progress in Motor Control*. Springer, 2009, pp. 699–726.

[23] N. Hogan, "Impedance control: An approach to manipulation," in *American Control Conference, 1984*. IEEE, 1984, pp. 304–313.

[24] M. Kawato, "Internal models for motor control and trajectory planning," *Current opinion in neurobiology*, vol. 9, no. 6, pp. 718–727, 1999.

[25] E. Burdet, R. Osu, D. Franklin, T. Yoshioka, T. Milner, and M. Kawato, "A method for measuring endpoint stiffness during multi-joint arm movements," *Journal of biomechanics*, vol. 33, no. 12, pp. 1705–1709, 2000.

[26] R. v. Ham, T. Sugar, B. Vanderborght, K. Hollander, and D. Lefeber, "Compliant actuator designs," *Robotics & Automation Magazine, IEEE*, vol. 16, no. 3, pp. 81–94, 2009.

[27] I. BIPM, I. IFCC, I. IUPAC, and O. ISO, "International vocabulary of metrology—basic and general concepts and associated terms (vim), 3rd edn. jcgm 200: 2008," 2008.

[28] A. De Luca, B. Siciliano, and L. Zollo, "PD control with on-line gravity compensation for robots with elastic joints: Theory and experiments," *Automatica*, vol. 41, no. 10, pp. 1809–1819, 2005.

[29] G. Palli, C. Melchiorri, and A. De Luca, "On the feedback linearization of robots with variable joint stiffness," in *Proc. IEEE Int. Conf. on Robotics and Automation*, 2008, pp. 1753–1759.

[30] J. M. Loomis and S. J. Lederman, *Tactual perception. Hand-book of Perception and Human Performance, II, p. 1-41.* Malden MA, USA: Wiley-Interscience, 1986.

[31] R. S. Johansson and G. Westling, “Roles of glabrous skin receptors and sensorimotor memory in automatic control of precision grip when lifting rougher or more slippery objects,” *Experimental Brain Research*, vol. 56(3), pp. 550–564, October 1984.

[32] M. A. Srinivasan and R. H. LaMotte, “Tactile discrimination of softness,” *Journal of Neurophysiology*, vol. 73, no. 1, pp. 88–101, June 1995.

[33] V. Levesque, J. Pasquero, V. Hayward, and M. Legault, “Display of virtual braille dots by lateral skin deformation: Feasibility study,” *ACM Trans. on Applied Perception*, vol. 2, no. 2, pp. 132–149, April 2005.

[34] A. Bicchi, D. E. De Rossi, and E. P. Scilingo, “The role of the contact area spread rate in haptic discrimination of softness,” *IEEE trans. on Robotics and Automation*, vol. 16, no. 5, pp. 496–504, October 2000.

[35] K. Fujita and H. Ohmori, “A new softness display interface by dynamic fingertip contact area control,” in *World Multiconf. on Systemics, Cybernetics and Informatics*, Orlando, Florida (USA), July 2001, pp. 78–82.

[36] S. L. Lederman and R. L. Klatzky, “Relative availability of surface and object properties during early haptic processing,” *Journal of Experimental Psychology: Human Perception and Performance*, vol. 23, no. 6, pp. 1680–1707, December 1997.

[37] M. A. Srinivasan and R. H. LaMotte, “Tactile discrimination of softness,” *Journal of Neurophysiology*, vol. 73, no. 1, pp. 88–101, June 1995.

[38] V. H. V. Levesque, J. Pasquero and M. L. R.D., “Display of virtual braille dots by lateral skin deformation: Feasibility study,” *ACM Trans. on Applied Perception*, vol. 2(2), pp. 132–149, April 2005.

[39] C. Lovchik and M. A. Diftler, “The robonaut hand: a dexterous robot hand for space,” in *Robotics and Automation, 1999. Proceedings. 1999 IEEE International Conference on*, vol. 2. IEEE, 1999, pp. 907–912.

[40] K. J. De Laurentis and C. Mavroidis, “Mechanical design of a shape memory alloy actuated prosthetic hand,” *Technology and Health Care*, vol. 10, no. 2, pp. 91–106, 2002.

[41] G. Grioli, M. Catalano, E. Silvestro, S. Tono, and A. Bicchi, “Adaptive synergies: an approach to the design of under-actuated robotic hands.” in *Intelligent Robots and Systems, 2012. IROS 2012. IEEE/RSJ International Conference on.* IEEE, 2012.

[42] C. Brown and H. Asada, “Inter-finger coordination and postural synergies in robot hands via mechanical implementation of principal components analysis,” in *Intelligent Robots and Systems, 2007. IROS 2007. IEEE/RSJ International Conference on.* IEEE, 2007, pp. 2877–2882.

[43] M. Ciocarlie, C. Goldfeder, and P. Allen, “Dexterous grasping via eigengrasps: A low-dimensional approach to a high-complexity problem,” in *Proceedings of the Robotics: Science & Systems 2007 Workshop-Sensing and Adapting to the Real World, Electronically published.* Citeseer, 2007.

[44] T. Wimboeck, C. Ott, and G. Hirzinger, “Passivity-based object-level impedance control for a multifingered hand,” in *Intelligent Robots and Systems, 2006 IEEE/RSJ International Conference on.* Ieee, 2006, pp. 4621–4627.

[45] R. Murray, Z. Li, and S. Sastry, *A mathematical introduction to robotic manipulation.* CRC, 1994.

[46] M. Gabiccini, E. Farnioli, and A. Bicchi, “Grasp and manipulation analysis for synergistic underactuated hands under general

loading conditions," in *Robotics and Automation (ICRA), 2012 IEEE International Conference on.* IEEE, 2012, pp. 2836–2842.

[47] T. Easton, "On the normal use of reflexes: The hypothesis that reflexes form the basic language of the motor program permits simple, flexible specifications of voluntary movements and allows fruitful speculation," *American Scientist*, vol. 60, no. 5, pp. 591–599, 1972.

[48] D. Prattichizzo, M. Malvezzi, and A. Bicchi, "On motion and force controllability of grasping hands with postural synergies," *Proceedings of Robotics: Science and Systems, Zaragoza, Spain*, 2010.

[49] J. Rosmarin and H. Asada, "Synergistic design of a humanoid hand with hybrid dc motor-sma array actuators embedded in the palm," in *Robotics and Automation, 2008. ICRA 2008. IEEE International Conference on.* IEEE, 2008, pp. 773–778.

[50] M. Grebenstein, A. Albu-Schaffer, T. Bahls, M. Chalon, O. Eiberger, W. Friedl, R. Gruber, S. Haddadin, U. Hagn, R. Haslinger *et al.*, "The dlr hand arm system," in *Robotics and Automation (ICRA), 2011 IEEE International Conference on.* IEEE, 2011, pp. 3175–3182.

[51] R. Tomovic and G. Boni, "An adaptive artificial hand," *Automatic Control, IRE Transactions on*, vol. 7, no. 3, pp. 3–10, 1962.

[52] C. Gosselin, F. Pelletier, and T. Laliberte, "An anthropomorphic underactuated robotic hand with 15 dofs and a single actuator," in *Robotics and Automation, 2008. ICRA 2008. IEEE International Conference on.* IEEE, 2008, pp. 749–754.

[53] A. Dollar and R. Howe, "The highly adaptive sdm hand: Design and performance evaluation," *The International Journal of Robotics Research*, vol. 29, no. 5, p. 585, 2010.

[54] T. Laliberte, L. Birglen, and C. Gosselin, "Underactuation in robotic grasping hands," *Machine Intelligence & Robotic Control*, vol. 4, no. 3, pp. 1–11, 2002.

[55] B. Hillberry and A. Hall Jr, "Rolling contact joint," Jan. 13 1976, uS Patent 3,932,045.

[56] G. Pratt and M. Williamson, "Series elastic actuators," in *Proceedings of the IEEE/RSJ International Conference on Intelligent Robots and Systems (IROS-95)*, vol. 1. IEEE, 1995, pp. 399–406.

[57] G. Grioli and A. Bicchi, "A non-invasive, real-time method for measuring variable stiffness," *Robotics Science and Systems. Robotics Science and Systems. Zaragoza, Spain*, 2010.

[58] A. Bicchi, G. Tonietti, M. Bavaro, and M. Piccigallo, "Variable stiffness actuators for fast and safe motion control," *Robotics Research*, pp. 527–536, 2005.

[59] R. Van Ham, B. Vanderborght, M. Van Damme, B. Verrelst, and D. Lefeber, "MACCEPA, the mechanically adjustable compliance and controllable equilibrium position actuator: Design and implementation in a biped robot," *Robotics and Autonomous Systems*, vol. 55, no. 10, pp. 761–768, 2007.

[60] R. Van Ham, T. Sugar, B. Vanderborght, B., K. Hollander, and D. Lefeber, "Review of actuators with passive adjustable compliance/controllable stiffness for robotic applications," *IEEE Robotics & Automation Magazine*, vol. 1070, no. 9932/09, p. 81, 2009.

[61] M. Laffranchi, N. Tsagarakis, and D. Caldwell, "A Variable Physical Damping Actuator (VPDA) for Compliant Robotic Joints."

[62] K. Hashimoto, T. Kureha, Y. Nishimura, K. Okumura, and S. Muraoka, "Measurement of mechanical impedance using quartz resonator force sensor during the process of grasping," in *SICE 2004 Annual Conference*, vol. 1, 2004, pp. 722–726 vol. 1.

[63] L. Ljung and E. Ljung, *System identification: theory for the user.* Prentice-Hall Englewood Cliffs, NJ, 1987.

[64] B. V. Amir Jafari, Nikos G. Tsagarakis and D. G. Caldwell, "A novel actuator with adjustable stiffness (awas)," in *IROS*, Taipei (accepted), 2010.

[65] N. Magnenat-Thalmann, P. Volino, U. Bonanni, I. R. Summers, M. Bergamasco, F. Salsedo, and F. E. Wolter, "From physics-based simulation to the touching of textiles: The haptex project," *The International Journal of Virtual Reality*, vol. 6, no. 3, pp. 35–44, September 2007.

[66] M. Bergamasco, F. Salsedo, M. Fontana, F. Tarri, C. A. Avizzano, A. Frisoli, E. Ruffaldi, and S. Marcheschi, "High performance haptic device for force rendering in textile exploration," *The Visual Computer, Springer Berlin/Heidelberg*, vol. 23, no. 4, pp. 247–256, April 2007.

[67] P. Volino, P. Davy, U. Bonanni, C. Luible, N. Magnenat-Thalmann, M. Mkinen, and H. Meinander, "From measured physical parameters to the haptic feeling of fabric," *The Visual Computer, Springer Berlin/Heidelberg*, vol. 23, no. 2, pp. 133–142, February 2007.

[68] C. Luible, M. Varheenmaam, N. Magnenat-Thalmann, and H. Meinander, "Subjective fabric evaluation," in *Int. Conference on Cyberworlds, HAPTEX'07 Workshop, IEEE Computer Society*, Hannover, Germany, October 2007, pp. 285–291.

[69] M. Varheenmaam and H. Meinander, “Mechanical properties as a base for haptic sensing of virtual fabrics,” in *Proc. Autex 2007 Conference*, Tampere, Finland, June 2007.

[70] E. P. Scilingo, N. Sgambelluri, G. Tonietti, and A. Bicchi, “Integrating two haptic devices for performance enhancement,” in *World Haptics Conference*, Tsukuba, Japan, March 2007, pp. 139–144.

[71] K. O. Johnson, “The roles and functions of cutaneous mechanoreceptors,” *Curr. Opin. Neurobiol.*, vol. 11, no. 4, pp. 455–461, August 2001.

[72] R. C. Oldfield, “The assessment and analysis of handedness: The edinburgh inventory,” *Neuropsychologia*, vol. 9, no. 1, pp. 97–113, March 1971.

[73] R. M. Friedman, K. D. Hetster, B. G. Green, and R. H. LaMotte, “Magnitude estimation of softness,” *Exp Brain Res.*, vol. 191, no. 2, pp. 133–142, November 2008.

[74] W. M. Bergmann Tiest and A. M. L. Kappers, “Cues for haptic perception of compliance,” *IEEE Transactions on Haptics*, vol. 2, no. 4, pp. 189–199, October-December 2009.

[75] F. K. B. Freyberger and B. Farber, “Compliance discrimination of deformable objects by squeezing with one and two fingers,” in *EuroHaptics 2006*, Paris, France, July 2006, pp. 271–276.

[76] E. P. Scilingo, M. Bianchi, G. Grioli, and A. Bicchi, “Rendering softness: Integration of kinaesthetic and cutaneous information in a haptic device,” *Transaction on Haptics, to appear.*

[77] G. Grioli and A. Bicchi, “A real-time parametric stiffness observer for vsa devices,” in *2011 IEEE International Conference on Robotics and Automation*, Shanghai, China, May 2011.

[78] A. Serio, G. Grioli, I. Sardellitti, N. Tsagarakis, and A. Bicchi, “A decoupled impedance observer for a variable stiffness robot,” in *IEEE International Conference on Robotics and Automation*, Shanghai, China, May 2011.

[79] “3-d finite-element models of human and monkey fingertips to investigate the mechanics of tactile sense,” *ASME, J. of Biomech. Eng.*, vol. 125, pp. 682–691, 2003.

[80] B. Hannaford and A. M. Okamura, *Springer Handbook on Robotics.* Heidelberg, Germany: Springer, 2008, ch. Haptics, pp. 719–739.

[81] A. Bicchi, J. K. Salisbury, and D. L. Brock, “Contact sensing from force measurements,” *The International Journal of Robotics Research*, vol. 12, no. 3, pp. 249–262, 1993.